Crystallization dynamics in glass-forming systems

by

Timothy Edward Cullinan

A dissertation submitted to the graduate faculty

in partial fulfillment of the requirements for the degree of

DOCTOR OF PHILOSOPHY

Major: Materials Science and Engineering

Program of Study Committee:

Ralph E Napolitano, Major Professor
Scott Beckman
Matt Kramer
Richard LeSar
Soeren Prell

Iowa State University

Ames, Iowa

2015

TABLE OF CONTENTS

LIST OF TABLES

LIST OF FIGURES

ACKNOWLEDGEMENTS

There are countless people who have helped me during my journey through graduate school. First, I would like to thank my major professor, Dr. Ralph Napolitano, for his guidance and support. I would also like to thank Dr. Matt Kramer for his helpful insight, thoughtful conversations, and for leading the structures and dynamics group to which I belonged. A special thanks goes to my committee members, Dr. Scott Beckman, Dr. Ludovico Cademartiri, Dr. Richard LeSar, and Dr. Soeren Prell, in light of their guidance and support as well.

I could not have completed this degree without the numerous people who saved me from day-to-day problems, taught me to use equipment, delivered my packages, and who generally took an interest in my success. Thanks to Kevin Dennis for answering my numerous questions regarding DSC. Thanks to Matt Besser for helping me melt-spin metallic glasses and lending me countless tools. Thanks to Emrah Simsek for helping me with countless tasks, troubleshooting motion control devices, and - most importantly - for discovering Egg Harbor. Thanks to Luis Fabietti for helping me discover the real issues behind my countless problems.

I am also very grateful for the support that I received from my groupmates: James Acton, Yang Huo, Paul Matlage, Megan Meyer, Zach Royer, Irmak Sargin. Other graduate students who were instrumental in my success include Connor Daily, Ryan Gebhardt, and Danny Vennerberg.

This work was supported by the US Department of Energy, Office of Basic Energy Science, Division of Material Sciences and Engineering. The research was performed at Ames Laboratory, Ames Laboratory is operated for the US Department of Energy by Iowa State University under Contract No. DE-AC02-07CH11358.

ABSTRACT

Crystallization under far-from-equilibrium conditions is investigated for two different scenarios: crystallization of the metallic glass alloy $Cu_{50}Zr_{50}$ and solidification of a transparent organic compound, *o*-terphenyl. For $Cu_{50}Zr_{50}$, crystallization kinetics are quantified through a new procedure that directly fits thermal analysis data to the commonly utilized JMAK model. The phase evolution during crystallization is quantified through *in-situ* measurements (HEXRD, DSC) and *ex-situ* microstructural analysis (TEM, HRTEM). The influence of chemical partitioning, diffusion, and crystallographic orientation on this sequence are examined. For *o*-terphenyl, the relationship between crystal growth velocity and interface undercooling is systematically studied via directional solidification.

CHAPTER 1. INTRODUCTION

The rigid nature of solids make them difficult to manipulate mechanically, especially under ambient conditions. Heating a solid reduces the mechanical burden associated with deformation, as the forging of hot iron by a blacksmith demonstrates. Extending the notion of deforming a material while it is hot, we arrive at solidification which utilizes thermal energy to maintain a liquid that can be deformed using far less mechanical work. Indeed, highly intricate shapes can be produced by filling a mold with a liquid and allowing it to freeze.

The properties of a material are intimately linked to its structural hierarchy that often spans a vast range of length scales and includes defects. Since this hierarchy [1] is often established during solidification, engineering the properties of a material that is solidified requires an understanding of (i) the kinetics and mechanisms associated with the structural evolution and (ii) the process parameters [2] to which these are linked.

The present work is concerned with crystallization under far-from-equilibrium conditions. The extent to which a system is driven away from equilibrium can profoundly influence its transformation pathways and resulting state. In terms of solidification, a liquid that survives below its melting temperature falls further out of equilibrium with increased undercooling. Concamitant with an increased undercooling is a change in the relative thermodynamic stabilities and nucleation and growth kinetics of competing crystalline phases. Indeed, the potential for novel phases and microstructures presented under such conditions is of great fundamental and practical interest. One way to access high undercoolings is through rapid solidification, where a high cooling rate limits the chance of nucleation and growth of a crystal due to the reduced

[1] Examples include: atomic structure (i.e. crystalline phase(s) or amorphous), grain size / alignment / count, chemical gradients, dislocation density, etc.

[2] Such as cooling rate, composition, pressure, applied fields (electromagnetic, gravitational, etc.), geometric constraints, etc.

time that a liquid spends at temperatures where nucleation and growth rates are significant. During this time in undercooled states, a material may have the opportunity to access kinetic pathways that are difficult or impossible to achieve via conventional processing methods.

Cooling through deeply undercooled states may allow the formation of metastable phases, novel microstructures, and perhaps an amorphous solid. These non-equilibrium freezing products may even serve as a precursor for subsequent phase transformations. FINEMET, for example, was the first magnetically soft material to derive enhanced properties from partial devitrification of a glassy precursor (Fe-Si-B with small amounts of Cu and Nb). During carefully designed annealing steps, shown schematically in Fig. 1.1, Cu rich crystallites (fcc) precipitate from the glass and serve as heterogeneous nucleation sites for the ferromagnetic Fe-Si phase (bcc)[3], which grows and ultimately comprises a significant volume fraction of the material, although the nominal crystallite size is quite small (approx. 10 nm). The growth of Fe-Si crystallites slows and eventually halts as B and Nb are rejected to the surrounding glass, shifting it to a more stable composition [24, 25]. The resulting ultrafine grains, dispersed in an amorphous matrix, would be difficult to produce via traditional solidification techniques because they are generally unable to provide the high nucleation and low growth rates required to produce such an ultrafine crystalline structure.

The annealed nanocomposite structure shown in Fig. 1.1 allows magnetic coupling between the ultrafine ferromagnetic crystallites, which reduces the effective magnetic anisotropy and provides very soft magnetic behavior.[4] In fact, magnetically soft amorphous and nanocrystalline alloys have enabled several practical advances, such as a dramatic reduction in the size of electrical transformers couled with an increase in their efficiency. Even small improvements to a single hysteresis cycle can provide enormous savings in the long term, considering the number of devices worldwide that require transformed electrical power, some of which operate continuously.

As the example above illustrates, understanding the dynamics of phase competition in terms

[3]TEM and nano beam diffraction revealed Kurjumov-Sachs-based and Nishiyama-Wasserman-based relations, in addition to a third orientation relation, between the fcc (Cu) and bcc (Fe-Si) phases, all of which involve parallel close-packed planes that reduce the energy barrier associated with nucleation. [24]

[4]High saturation magnetization, high permeability, low coercivity, and low hysteresis loss

of thermodynamic stabilities and growth mechanisms is a crucial prerequisite for controlling the structure and properties of a material that is traversing a kinetic landscape that is far-from-equilibrium. Although numerous reports on the crystallization kinetics of metallic glass exist, the majority are anecdotal and lack sufficient rigor to reveal subtle details that may arise during devitrification. The crystallization kinetics of melt-spun $Cu_{50}Zr_{50}$, for example, have been studied extensively, yet the reported devitrification mechanisms and resulting phases vary considerably. This is mostly a result of how the transformation was commonly investigated, namely, *ex-situ* X-ray diffraction (XRD) of specimens that endured continuous heating to a temperature associated with the completion of an exothermic reaction, as measured by thermal analysis. Such an approach provides, at best [5] ,the phase fraction(s) associated with a particular instant in time late in the transformation and risks overlooking complex phenomena, such as transient metastable phase sequences and cooperative reactions that often characterize highly driven transformations.

One of the challenges associated with investigating such transformations is that the XRD patterns for the relevant phases are largely overlapping and difficult to deconvolute. Also, conventional XRD is less capable of detecting nano-sized crystallites compared to high-energy X-ray diffraction (HEXRD), especially when the crystalline phase fraction is small. In a recent investigation using a heating rate of 10 K/min for the devitrification of melt-spun $Cu_{50}Zr_{50}$, Kalay et al. [6] reported a sequence involving the initial formation of the $Cu_{10}Zr_7$, $CuZr_2$, and CuZr phases followed by a gradual decomposition of the metastable CuZr into $Cu_{10}Zr_7$, and $CuZr_2$. The initial three-phase devitrification occurred too rapidly for the transformation kinetics of the individual phase(s) to be resolved. However, by applying a quantitative modeling approach to analyze *in-situ* HEXRD patterns, it was determined that the initial devitrification resulted in relative phase fractions of 0.399, 0.223, and 0.378 (by weight) for $Cu_{10}Zr_7$, $CuZr_2$, and CuZr, respectively. Moreover, this method enabled full quantification of the phase-resolved kinetics of the slower post-crystallization decomposition reaction that began partway through the first, sharp, exotherm and ended shortly after the broad second exotherm, resulting in a fully CuZr structure. Even for the relatively low heating rate of 10 K/min, the initial devitrification

[5] Only after substantial and careful modeling / analysis of X-ray patterns.

was too rapid to allow the initial phase evolution to be resolved, particularly the order in which the phase(s) precipitated from the amorphous ribbon. As noted in Table A and the phase(s) associated with the initial transformation vary considerably among previous reports on the constant heating rate devitrification of $Cu_{50}Zr_{50}$.

A more recent study by Cullinan et al. [64] [6] utilized carefully selected isothermal annealing treatments that resulted in a slower transformation, allowing the initial crystallization sequence to be resolved through *in-situ* HEXRD measurements and electron microscopy of specimens that were quenched at different times throughout the annealing (see Fig. A.2b). The high quality and resolution of the data revealed that the initial devitrification occurs in three stages: (i) $Cu_{10}Zr_7$ crystallites nucleate from the amorphous precursor and grow[7] depleting the surrounding glass of Cu; (ii) when the Cu:Zr ratio of the surrounding glass reaches 1:2,[8] $CuZr_2$ nucleates on the interfaces between the glass and $Cu_{10}Zr_7$ crystallites and grows until the Zr-rich region of the glass is consumed; (iii) the CuZr phase nucleates epitaxially on the glass/$CuZr_2$ interfaces and grows until the specimen is fully crystalline. As indicated in Fig. 1.3, the crystalline phase fractions at the end of the isothermal transformation are consistent with those measured at the beginning of the constant-heating rate transformation. The approach taken by these related studies [6, 64] [9] provides a view of the crystallization process backed by direct experimental data with never-before achieved fidelity.

Similar to the mechanism reported for FINEMET, solute rejection limits the growth of $Cu_{10}Zr_7$ and promotes the growth of $CuZr_2$ in the surrounding Zr rich glass. As $CuZr_2$ grows to the edge of the Zr rich glassy layer, the growth of CuZr becomes favorable because (i) an epitaxial relationship between these crystal structures (see Fig. 1.3) catalyzes the nucleation of CuZr and (ii) subsequent growth of CuZr requires a minimal diffusion burden, since the surrounding glass is the same composition. Thus, atoms merely need to arrive at an appropriate and available lattice site on the interface and no subsequent solute partitioning is required. As these examples illustrate, the phase evolution during crystallization under far-from-equilibrium

[6] Included in Appendix A

[7] At the same time, small plate-like crystals are observed to nucleate from the glass. Their structure is not confirmed, but is consistent with $CuZr_2$.

[8] This seems to occur when the $Cu_{10}Zr_7$ crystallites are approximately 100 nm in size.

[9] Kalay et. al. (2011) and Cullinan et. al. (2015). The latter study is included in Appendix A.

conditions may involve convoluted mechanisms that form metastable phases and structures. Indeed, B2 structures are useful for they tend to participate in martensitic and shape memory transformations, but the phases involved in these reactions tend to be unstable near ambient conditions [26, 27, 28, 29]. This begs the question: can we control the formation of metastable phases to engineer novel microstructures with practical properties, and can we preserve them for use under conditions of interest?

Metastable phase formation is not specific to metallic systems, however, and is commonly observed for organic compounds that are polymorphic.[10] Recent estimates suggest that 30 to 50 percent of pharmaceutically relevant compounds are polymorphic [30]. Amorphous and metastable crystalline phases are desirable forms for drugs because they tend to provide enhanced solubility and therefore enhanced bioavailability per dose. These desirable phases are fragile, however, in the sense that they will transform to a more stable phase if presented such an opportunity during processing or storage.[11] Until recently, phase stability and polymorphic transformations were frequently neglected in the pharmaceutical industry. Perhaps the most serious incident that highlighted the need for such awareness was the recent shortage of Norvir (ritonavir), an antiretroviral drug commonly used in combination with other drugs to control symptoms associated with HIV infection and AIDS. The drug was originally marketed in 1996 in two versions: oral liquid and oral semi-solid capsules. Only one crystal form of Norvir was identified throughout the development of 240 lots of semi-solid capsules, and presented no stability problems until 1998, when several capsule lots failed solubility tests. X-ray diffraction and microscopy revealed that the capsules contained a new and distinct polymorph that was much less soluble than the original. The sudden and rampant appearance of this contaminant polymorph, known as Form II, rendered the original form unattainable and no longer guaranteed the stability of the oral solution without signifiant refrigeration. The production of this lifesaving drug was therefore interrupted, severely threatening its supply until an alternative oral tablet that did not require refrigeration was approved by the FDA in 2000.

[10] When a compound exhibits multiple crystalline phases with distinct properties in the solid state, it is said to be polymorphic. The phenomenon is similar to allotropy, where a pure element exhibits multiple crystalline forms. Diamond and graphite are two allotropes of carbon, for example.

[11] An unintended change of temperature, pressure, pH, or other factor could invoke an undesirable phase change.

The formation of drugs and vaccines that do not require refrigeration or intravenous delivery is a critical necessity, if these and other life saving formulations are to be shared in places that lack electrical infrastructures and sharps disposal programs. It is estimated that 21 million hepatitis B, 2 million hepatitis C, and 250,000 HIV infections occur each year due to reused needles and syringes. The majority (about 70%) of new HIV infections each year occur in sub-Saharan regions of Africa, which is home to about 10% of the world's population [WHO]. According to 2009 estimates, 200-500 people in Africa are infected with HIV every day because of unsafe blood transfusions [inj] Since there is currently no cure for HIV or AIDS, prevention through education and safe practices are the primary mechanisms for limiting the spread of this pandemic [31].

Although some organic compounds such as sucrose, benzoic acid, and naphthalene are believed to exhibit only one crystal form under near-ambient conditions, numerous others exhibit multiple crystalline forms. ROY (5-methyl-2[(2-nitrophenyl)amino]-3-thiophenecarbonitrile)[12], for example, exhibits ten known polymorphs, seven of which are solved structures - which is the current record according to the Cambridge Structural Database. Perhaps the most intriguing aspect of this polymorphic system is that all ten polymorphs can be formed and maintained under near-ambient conditions. In fact, four of the seven crystalline forms can precipitate spontaneously and simultaneously from the same liquid near room temperature [1]. Several of the polymorphs are even capable of catalyzing the growth of a different and faster growing polymorph [32].

In addition to offering a rich suite of metastable forms that are readily accessible, ROY is also one of only eleven materials, all of which are glass-forming organic compounds (listed in Table 1.2), that exhibit an anomalous crystal growth mode at high undercoolings.[13] Unlike the crystallization of other deeply undercooled materials, this growth mode is associated with an abrupt increase in the isothermal growth velocity of crystals just above the glass transition temperature, T_g. Since the growth mode is also observed for temperatures that are well within

[12]The abbreviation is derived from its Red, Orange and Yellow polymorphs. The compound is an intermediate for the production of Olanzapine, an atypical antipsychotic drug for the treatment of schizophrenia and bipolar disorder.

[13]Four ROY polymorphs that can be studied near Tg exhibit GC growth: YT04, Y, R, and OP

the glassy regime, it is referred to as glass-crystal or GC growth. As Fig. 1.5 illustrates for *o*-terphenyl, the fibrous and compact spherulite morphologies are associated with growth velocities that are orders of magnitude faster than faceted growth at similar temperatures. The key features of this anomalous growth mode, which occurs under far-from-equilibrium conditions, are:

1. It has only been observed for eleven organic glass forming compounds, ten of which contain a phenyl ring.

2. It is associated with an abrupt increase in growth velocity, accompanied by a change from faceted to fibrous growth around $T_{Ff} = 1.15T_g$, the transition temperature. An increase in the bulk diffusivity of the constituent species does not occur in this temperature regime.

3. A subsequent morphology change from individual fibers to compact spherulites occurs at a higher undercooling, T_{fc}. No discontinuity of the linear growth rates of the fibrous and compact morphologies at T_{fc} has been reported. The volume growth rates exhibit a discontinuity, however, since the individual fibers do not fill space as quickly.

4. The isothermal growth velocities are independent of time.

5. If a spherulite growing via the compact GC mode is heated above T_{fc} its growth stops, yet fine fibers are noted to protrude from the halted interface. The compact GC growth resumes upon cooling below T_{fc}, but only at certain locations along the crystal/liquid interface.

6. Based on results for the polymorphic material ROY, GC growth is not correlated with the thermodynamic stability of the crystalline phase (e.g. R has stability intermediate between ON and YN, both of which do not exhibit GC growth). GC growth is not correlated with molecular conformation (e.g. YT04, Y, and YN have similar C-N bond twist angles, which are significantly different than the other polymorphs, yet YN does not exhibit GC growth). Polymorphs with higher density and more isotropic packing tended to exhibit GC growth.

1.1 Thesis Organization

The remainder of the thesis includes two distinct studies of crystallization under far from equilibrium conditions. Chapters 2, 3, and the Appendix A are related to the devitrification of a metallic glass $Cu_{50}Zr_{50}$, while chapters 4, 5, 6, and 7 pertain to the solidification of a transparent organic glass former, *o*-terphenyl. Chapters 2 and 4 provide independent reviews of literature that is relevant to each material.

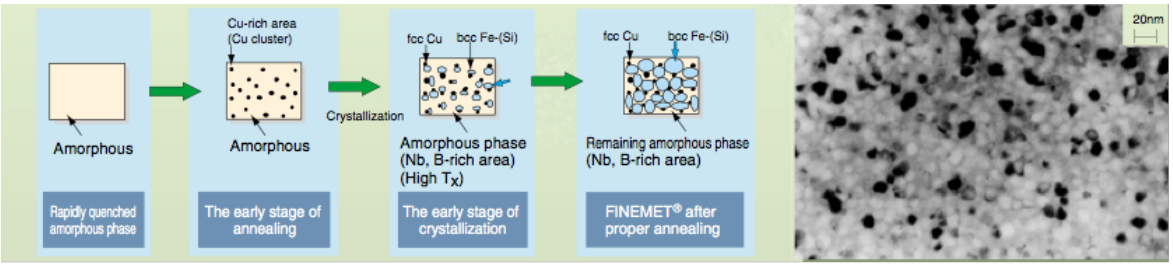

Figure 1.1 A schematic of the devitrification mechanism that produces the ultrafine microstructure of FINEMET. [2]

Table 1.1 A summary of the seven ROY polymorphs whose structures are solved. GC growth was observed for the shaded polymorphs (Y, YT04, R, and OP). [1].

Crystal Structures and Selected Properties of ROY Polymorphs[a]

form	Y	YT04	R	OP	ON	YN	ORP
crystal system	monoclinic	monoclinic	triclinic	monoclinic	monoclinic	triclinic	orthorhombic
space group [No.]	$P2_1/n$ [14]	$P2_1/n$ [14]	$P\bar{1}$ [2]	$P2_1/n$ [14]	$P2_1/c$ [14]	$P\bar{1}$ [2]	*Pbca* [61]
description	yellow prism	yellow prism	red prism	orange plate	orange needle	yellow needle	orange-red plate
a, Å	8.5001	8.2324	7.4918	7.9760	3.9453	4.5918	13.177
b, Å	16.413	11.8173	7.7902	13.319	18.685	11.249	8.0209
c, Å	8.5371	12.3121	11.9110	11.676	16.3948	12.315	22.801
α, deg	90	90	75.494	90	90	71.194	90
β, deg	91.767	102.505	77.806	104.683	93.830	89.852	90
γ, deg	90	90	63.617	90	90	88.174	90
Z	4	4	2	4	4	2	8
D_{calc}, g cm^{-3}	1.447	1.473	1.438	1.435	1.428	1.431	1.429
θ (deg)	104.7	112.8	21.7	46.1	52.6	104.1	39.4
ν_{CN}, cm^{-1}	2231	2224	2212	2226	2224	2222	2217
mp, °C	109.8	106.9	106.2	112.7	114.8	99	97
ΔH_m, kJ/mol	27.2	26.6	26.0	25.5	25.1	24.2	24.2
$H - H_Y$, kJ/mol[b]	0	0.9	1.4	1.9	2.6	3.0	4.1

[a] Empirical formula $C_{12}H_9N_3O_2S$. MW = 259.29. The structures were determined at 20−23 °C. [b] From fitting melting and eutectic melting data.[4,6,7]

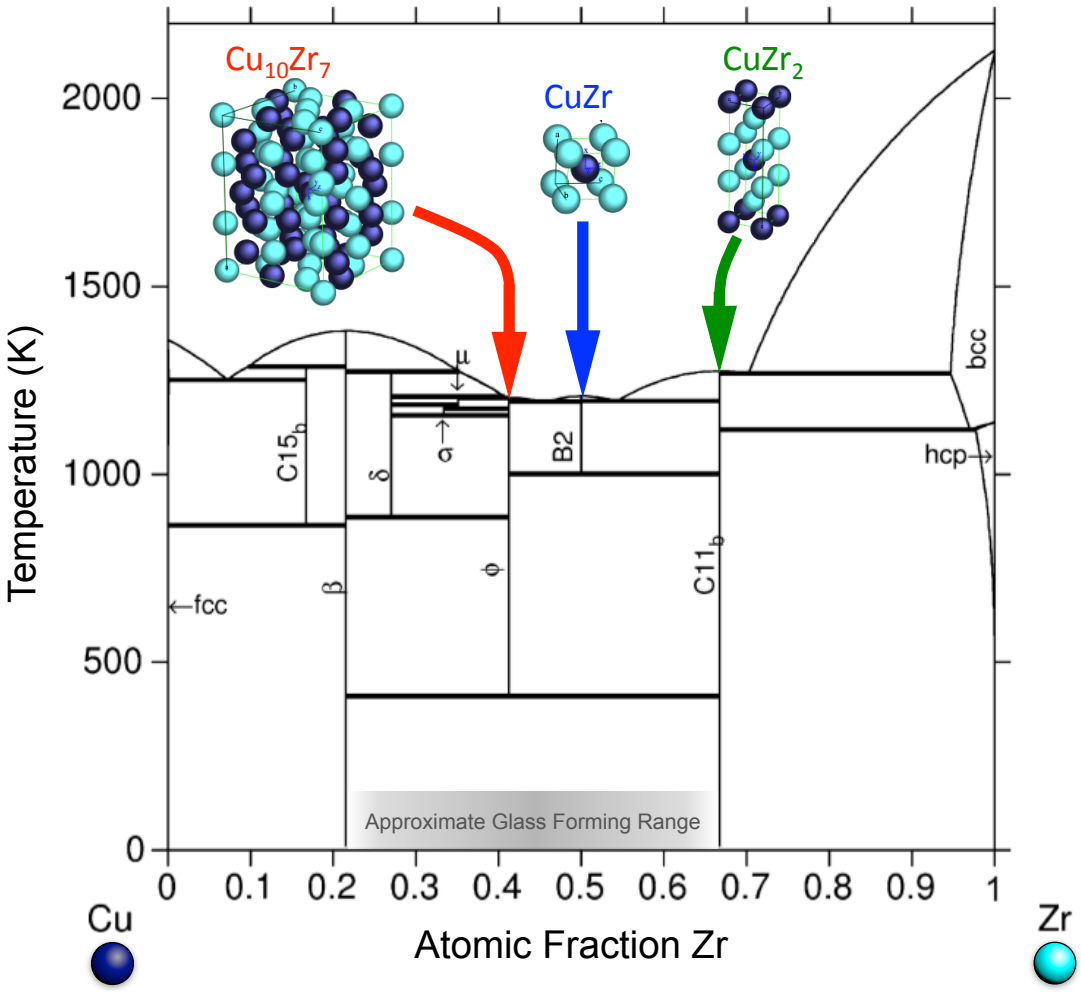

Figure 1.2 The devitrification of Cu-Zr binary metallic glasses has been studied extensively, partly because this system features strong glass formation tendency [3] and a wide composition range within which glassy alloys can be achieved by quenching from the melt [4, 5]. In addition, several intermetallic compounds that reside within or near this glass-forming range may play a role in the devitrification behavior, potentially appearing as stable, metastable, or transient phases.

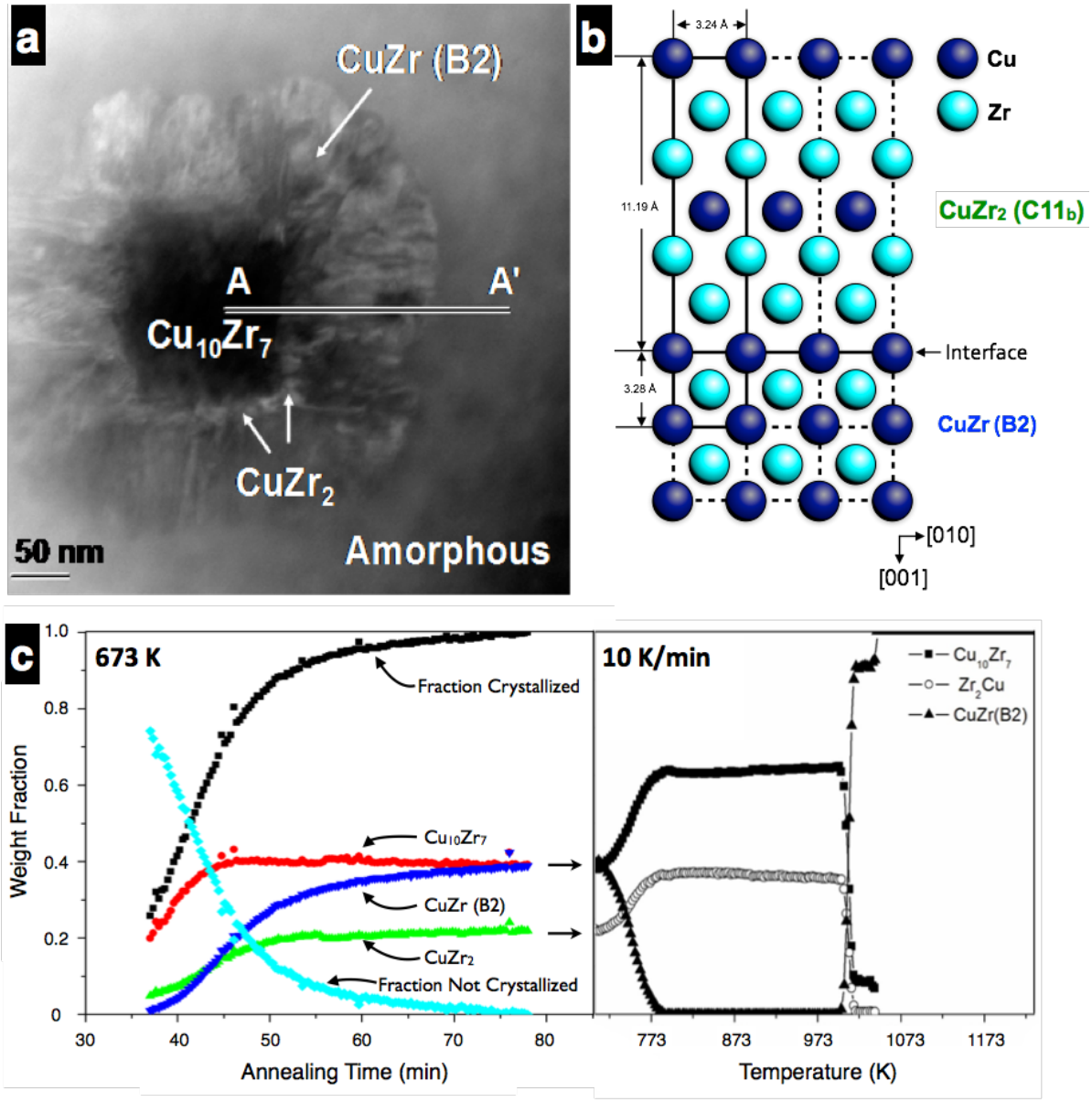

Figure 1.3 (a) A STEM image of melt-spun $Cu_{50}Zr_{50}$ isothermally annealed at 671 K (398°C) for 44 min. (b) A schematic showing the coherent interface between the $CuZr_2$ ($C11_b$) and CuZr (B2) phases. Through slight atomic rearrangements, the lattice parameter of $CuZr_2$ (3.24 $\AA$) enlarges to that of CuZr (3.28 $\AA$) (c) Time-resolved phase fractions computed from *in-situ* HEXRD patterns of isothermally annealed (673 K, 400°C) melt-spun $Cu_{50}Zr_{50}$, which agree well with the temperature-resolved phase fractions computed from *in-situ* HEXRD patterns collected during 10 K/min heating of melt-spun $Cu_{50}Zr_{50}$ [6].

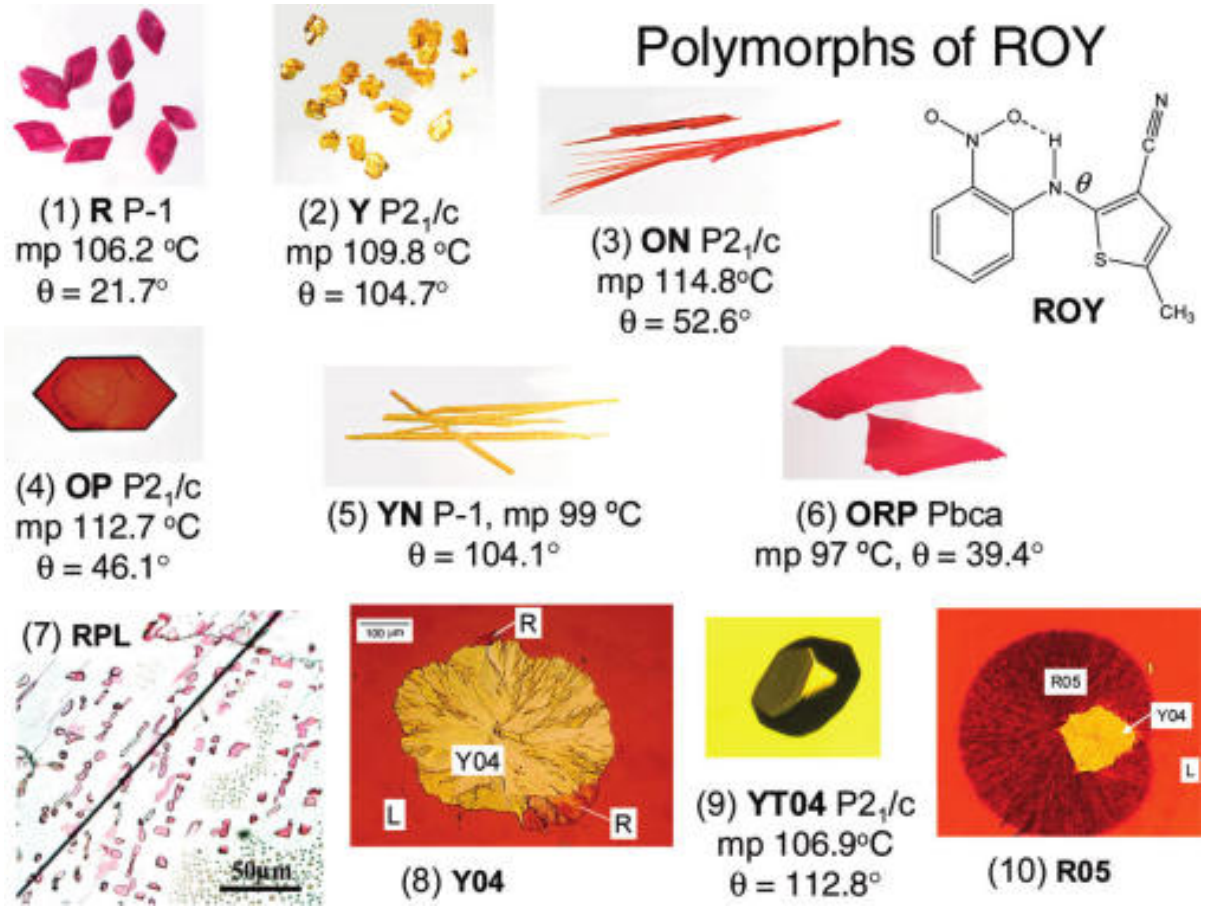

Figure 1.4 The ten know crystalline polymorphs exhibited by ROY (5-methyl-2[(2-nitrophenyl)amino]-3-thiophenecarbonitrile). Each form is associated with a unique color and morphology [1].

Table 1.2 A summary of the 11 materials that are known to exhibit the anomalous glass-crystal growth mode.

Compound	Molecule	Crystal Structure(s)	T_f [K] (°C)	ΔH_f kJ/mol	ΔS_f / R kJ/(mol K)	T_g [K] (°C)
benzophenone	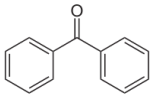	α - orthorombic **β - monoclinic**	α - 325 (52) **β - 301 (28)**	α - 18 **β - ?**	6.662	207 (-66)
salol	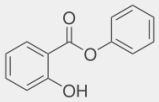	I. orthorombic III. monoclinic	I. 314 (41) III. 302 (2)	I. 18.6 III. 16.5	I. 7.13 II. 7.41	218 (-55)
o-terphenyl OTP	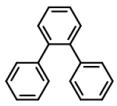	orthorombic	329 (56)	17.2	6.28	244 (-29)
triphenylethylene	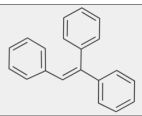		341 (68)	20.35	7.18	248 (-25)
toluene	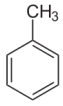	α - orthorombic (monolith) β - orthorombic (~ cubic)	α - 178 (-95) β - 153 (-120)	α - 6.64 (?)	α - 4.49	117 (-156)
diphenylphthalate	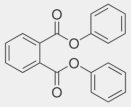		348 (75)			252 (-21)
dimethylphthalate	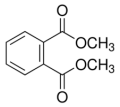		275 (2)			192 (-81)
cumene	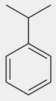		177 (-96)	7.32	4.97	127 (-146)
nifedipine Procardia	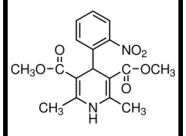	α - monoclinic **β - triclinic** γ - ?	α - 444 (171) **β - 436 (163)** γ - 408 (135)	α - 104 J/g **β - 70 J/g** γ - ?	α - 9.76 **β - 6.68** γ - ?	315 (42)
ROY Olanzapine Impurity A	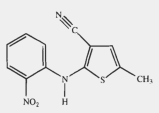	Y - monoclinic YT04 - monoclinic R - triclinic OP - monoclinic	383 (109.8) 380 (106.9) 379 (106.2) 385 (112.7)	27.2 26.6 26.0 25.5	8.54 8.42 8.25 7.97	259 (-14)
testosterone propionate	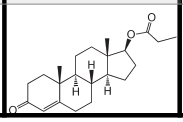	α - orthorombic **β -**	α - 393 (120)	α - 21	α - 6.43	272 (-1)

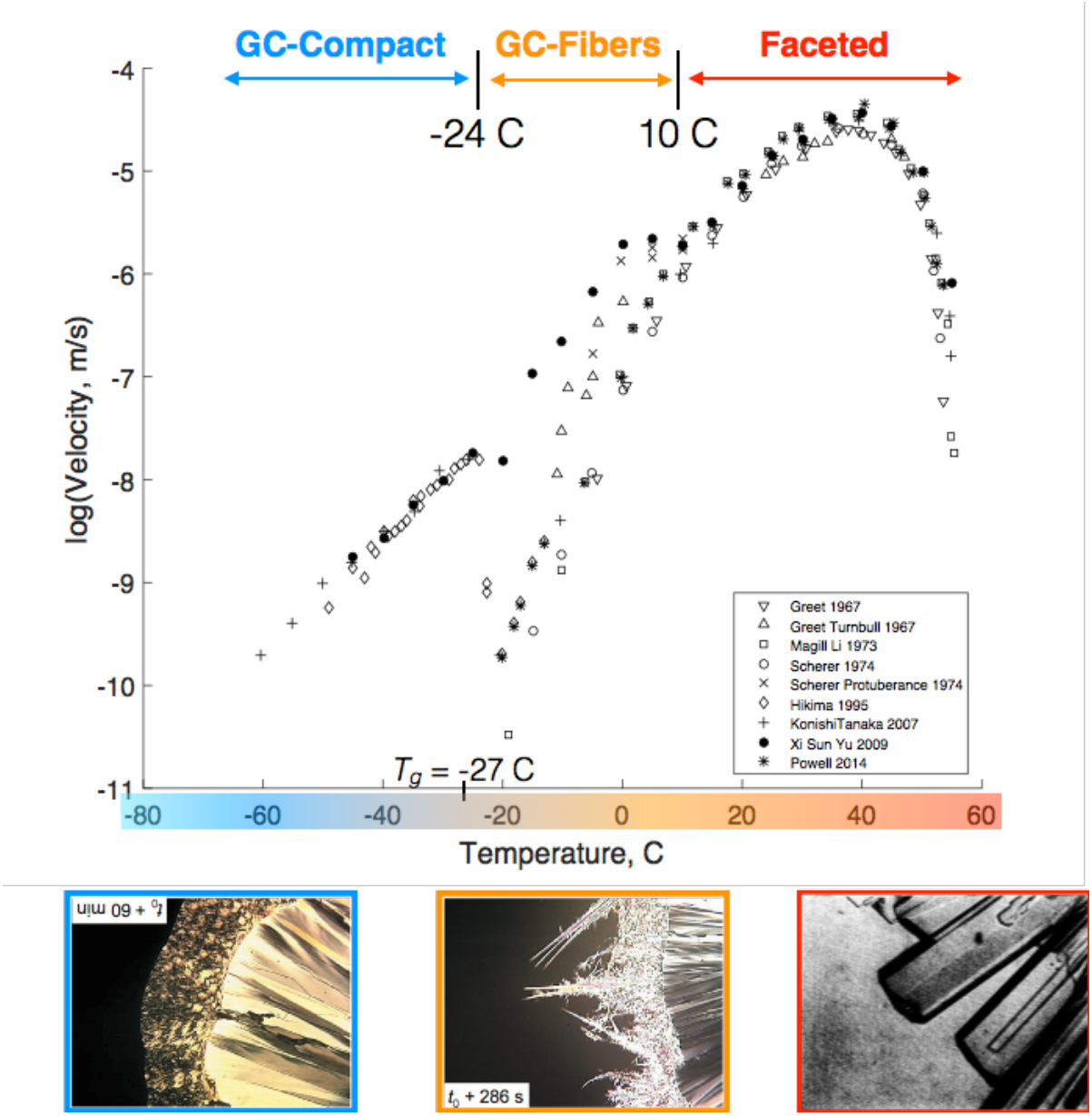

Figure 1.5 A summary of the glass-crystal growth studies for *o*-terphenyl under isothermal conditions [7, 8, 9, 10, 11, 12, 13, 14]. For low undercoolings, down to about 10°C, crystallization proceeds in a faceted manner [8]. The velocity of the smooth faceted front reaches a maximum of 45.7 micron per second around (40°C), and then decreases with further undercooling, due to the decreased molecular mobility (increasing viscosity) of the liquid. Around 10 °C, the glass-crystal growth manifests as individual fiber and whisker crystals protruding from the slower growing faceted front. As the undercooling is increased further, the glass-crystal growth is said to be fully activated and a compact form of growth ensues, which is also much faster than the advancement of the previously established faceted front. [13]

CHAPTER 2. DEVITRIFICATION OF $Cu_{50}Zr_{50}$ - REVIEW OF LITERATURE

The rapid solidification of metallic alloys may give rise to a hierarchy of non-equilibrium effects, ranging from small departures from local chemical equilibrium to large scale trapping of solutes and crystal defects, the growth of metastable crystalline phases, and even the formation of glassy or amorphous solids. Moreover, these non-equilibrium freezing products can be further transformed during subsequent heat treatments to yield novel structures with remarkable properties. Indeed, various far-from-equilibrium transformation pathways can provide access to phases and structures that may be difficult or impossible to achieve through more conventional avenues.

In particular, amorphous metals provide transformation pathways that remain largely unexplored, and there is great interest in exploiting the novel structures and enhanced properties that may be derived from the full or partial crystallization of an amorphous metal [33, 34]. Prediction and control of the phases and structures that are evolved along such far-from-equilibrium pathways, however, requires an understanding of the mechanisms and kinetics that govern the transformation dynamics.

The devitrification of Cu-Zr binary metallic glasses has been studied extensively, partly because this system features strong glass formation tendency [3] and a wide composition range within which glassy alloys can be achieved by quenching from the melt [4, 5], as shown in Fig A.1. In addition, several intermetallic compounds that reside within or near this glass-forming range may play a role in the devitrification behavior, potentially appearing as stable, metastable, or transient phases. While several studies of the kinetics and phase evolution during constant heating rate (CHR) and isothermal (ISO) devitrification of melt-quenched and mechanically alloyed $Cu_{50}Zr_{50}$ have been reported [1] the majority of these studies failed to

[1] See, for example, [35, 36, 37, 38, 39, 40, 41, 42, 43, 44, 45, 46, 47, 48, 49, 50, 51, 52, 53, 54, 55, 56, 57, 58,

describe the devitrification thoroughly and accurately because the underlying analyses often relied on poor quality [2] and/or insufficient data.[3] In some cases, reports of a transformation reaction or mechanism were made without any diffraction or microscopy evidence. Studies that included a kinetic analysis of the devitrification were unclear and incomplete, frequently failing to include all of the fitted parameters associated with a given kinetic model and usually omitting a description of how the parameters were computed. Thus, a complete description of the prevailing mechanisms and related kinetics that reconciles the various observations of phase evolution with system thermodynamics was not established within the literature.

2.1 Review of Constant-Heating Rate Devitrification Studies.

Table A summarizes the constant-heating rate devitrification studies of $Cu_{50}Zr_{50}$, some of which are highlighted in the following paragraphs. Freed et al. [35] used XRD, differential scanning calorimetry (DSC), and transmission electron microscopy (TEM) to study the crystallization of splat-quenched $Cu_{50}Zr_{50}$.[4] For a heating rate of 10 K/min, they reported a two-step devitrification sequence, associating the first exotherm (at 724 K) with partial crystallization resulting in nuclei of a metastable crystalline phase that was not identified. The second, and smaller, exotherm (at 731 K) was reported to correspond with complete crystallization resulting in the formation of the CuZr phase.

Using DSC, Buschow reported that melt-spun $Cu_{50}Zr_{50}$ exhibits two exothermic events when heated (at an unspecified rate). XRD revealed that the first event corresponded to crystallization of the sample, primarily into an orthorhombic CuZr phase, while the second event was proposed to be associated with recrystallization [38]. Dini and Dunlap also used XRD to study the phases formed after heating melt-spun ribbons via differential thermal analysis (DTA). For a sample heated at 20 K/min, they reported a fully crystalline structure comprised of $Cu_{10}Zr_7$ and $CuZr_2$ [41] .

59, 60, 61, 6, 62, 63]

[2]Such as relying on conventional X-ray diffraction (XRD) versus high-energy X-ray diffraction (HEXRD) measurements.

[3]Such as relying on one or just a few diffraction measurements of post-annealed samples versus *in-situ* measurements.

[4]Italics are used here to indicate that the notation is a shorthand description of composition and not a chemical formula.

Using XRD to investigate phase transitions in melt-spun ribbons on heating (40 K/min), Altounian reported that devitrification occurs in a single-step reaction involving the simultaneous formation of $Cu_{10}Zr_7$ and $CuZr_2$, with $Cu_{10}Zr_7$ as the major phase and $CuZr_2$ as the minor phase [39]. Using a much lower heating rate (0.835 K/min), Kneller et al. later reported that the nucleation of the CuZr phase, which is metastable at low temperature, precedes the formation of the $Cu_{10}Zr_7$ and $CuZr_2$ phases [43].

Lu et al. used DSC and Field Ion Microscopy (FIM) to study constant-heating rate (25 K/min) devitrification of $Cu_{50}Zr_{50}$ melt-spun ribbons, reporting a two-step process in which $Cu_{10}Zr_7$ precipitates first from the amorphous alloy at 723 K, followed by the $CuZr_2$ phase at 773 K [46]. Louzguine-Luzgin et al. measured two exothermic events through DSC (40 K/min), one sharp and one broad, for the devitrification of melt-spun ribbons. Through XRD measurements, they attributed the initial crystallization event to the formation of a metastable monoclinic CuZr phase, which transformed to $Cu_{10}Zr_7$ at higher temperatures. They also utilized differential isothermal calorimetry (DIC) to anneal samples at 693, 698, and 710 K. These thermal analysis measurements were subsequently used to model the devitrification kinetcs according to the Johnson-Mehl-Avrami-Kolmogorov (JMAK) equation, Eqn. A.1, resulting in Avrami exponent values, n, between 2.2 and 2.4. [54] Values of the JMAK parameter k were not reported.

Wang et al. investigated the devitrification of melt-spun ribbons through XRD measurements of samples that were heated via DSC (20 K/min) just up to the initiation of crystallization and samples heated just beyond the completion of crystallization and, in both cases, subsequently cooled to ambient temperature. The authors reported a fully crystalline structure comprised of the orthorhombic $Cu_{10}Zr_7$ phase, attributing it as a major competing crystalline phase due to its structural similarity to glassy $Cu_{50}Zr_{50}$ [57]. Using HEXRD, Pauly et al. reported that heating $Cu_{50}Zr_{50}$ melt-spun ribbons through 973 K resulted in a single-step formation of the equilibrium crystalline phases, $Cu_{10}Zr_7$ and $CuZr_2$ [58].

Fernandez et al. utilized DSC, XRD, and TEM to study the devitrification kinetics of $Cu_{50}Zr_{50}$ powder prepared by gas atomization [59]. Although XRD indicated that the as-atomized powder was amorphous, HRTEM revealed the presence of $Cu_{10}Zr_7$ nanocrystals. 10 K/min heating of as-atomized powders indicated a single exothermic peak associated with the further formation of $Cu_{10}Zr_7$, according to XRD and TEM diffraction patterns of post-DSC samples. Louzguine-Luzgin et al. studied the devitrification of melt-spun $Cu_{50}Zr_{50}$ through DSC (40 K/min) and XRD and reported that the first exothermic crystallization event corresponds to the formation of a metastable monoclinic CuZr phase. They also utilized DIC at temperatures 20 to 50 K below the onset of crystallization, analyzed their findings using the JMAK expression (Eqn. A.1), and reported an n value of approximately 2.5 [60, 61]. As before, k values were not reported. Mattern et al. studied the devitrification of melt-spun ribbons via small and wide angle X-Ray scattering and reported that the equilibrium phases, $Cu_{10}Zr_7$ and $CuZr_2$, formed at about 723 K while heating from 573 K to 773 K in 10 K steps [62].

Recently, Cui et al. reported on the phase evolution of melt-spun $Cu_{50}Zr_{50}$. They utilized XRD measurements to determine the phases present at various stages of the devitrification process, using resistivity measurements as a guide. They investigated samples that were i) quenched into water after the "primary" precipitation, ii) quenched into water from 1100 K to determine the "transformed" (intermediate) crystal phases, and iii) slow cooled from 1100 K to determine the final crystalline phases. They reported $Cu_{10}Zr_7$ and $CuZr_2$ as the primary phases, CuZr (B2) as the transformed phase, and $Cu_{10}Zr_7$ and $CuZr_2$ as the final phases [63].

Although the results of the initial crystallization and subsequent phase evolution vary considerably, a few trends are noted among the reports. The first transformation upon heating amorphous $Cu_{50}Zr_{50}$ was most frequently reported as an exothermic event, beginning around 720 K, that was associated with complete crystallization [5] involving the formation of $Cu_{10}Zr_7$ and $CuZr_2$. Of the five [41, 47, 50, 58, 62] studies that shared this result in common, two [58, 62] reported a second exothermic event around 773 K and 783 K, respectively, during

[5] By this we mean the sample no longer features an amorphous fraction. This does not necessarily imply that the resulting crystalline phase(s) are the final products of a given phase evolution.

thermal analysis. Only one [58] of those studies reported on the phase evolution corresponding with the second exotherm, associating it with the growth (increased fraction) of $CuZr_2$. This result is consistent with the phases that are most commonly reported as being present after the second exotherm, namely, $Cu_{10}Zr_7$ and $CuZr_2$.

One of the challenges associated with investigating such transformations is that the X-ray diffraction (XRD) patterns for the relevant phases are largely overlapping and difficult to deconvolute. Also, conventional XRD is less capable of detecting nano-sized crystallites compared to high-energy X-ray diffraction (HEXRD), especially when crystalline phase fraction is small. In a recent investigation using a heating rate of 10 K/min for the devitrification of melt-spun $Cu_{50}Zr_{50}$, Kalay et al. [6] reported a sequence involving the initial formation of the $Cu_{10}Zr_7$, $CuZr_2$, and CuZr phases [6] followed by a gradual decomposition of the metastable CuZr into $Cu_{10}Zr_7$, and $CuZr_2$. Differing from the observations of Freed et al. [35] for this heating rate, Kalay et al. found that the initial three-phase devitrification occurred too rapidly for the transformation kinetics of the individual phase(s) to be resolved. However, by applying a quantitative modeling approach to analyze *in-situ* HEXRD patterns, it was determined that the initial devitrification resulted in relative phase fractions of 0.399, 0.223, and 0.378 (by weight) for $Cu_{10}Zr_7$, $CuZr_2$, and CuZr, respectively. Moreover, this method enabled full quantification of the phase-resolved kinetics associated with the slower post-crystallization decomposition reaction that began partway through the first, sharp, exotherm and ended shortly after the broad second exotherm that produces a fully CuZr structure.

2.2 Review of isothermal devitrification studies.

Table A summarizes the isothermal devitrification studies of $Cu_{50}Zr_{50}$, some of which are highlighted in the following paragraphs. Using DSC, Polk et. al. [36] measured the thermal response of melt-spun $Cu_{50}Zr_{50}$ during isothermal annealing treatments conducted at 5 K intervals from 690 to 715 K, although they only reported the DSC trace for 700 K. Unfortunately, no phase evolution or kinetic analysis was reported.

[6] Unless otherwise indicated, the $Cu_{10}Zr_7$, $CuZr_2$, and CuZr phases are assumed to exhibit the $oC68$, $tI6$, and $cP2$ (B2) structures, respectively.

Using differential isothermal calorimetry (DIC), Louzguine-Luzgin et al. [54] annealed melt-spun ribbons of $Cu_{50}Zr_{50}$ at 693, 698, and 710 K. XRD of ribbon that was annealed for 20 min at 698 K (annealed slightly longer than was required for the exotherm to return to the baseline signal) indicated that a monoclinic form of CuZr precipitated from the glass during the isothermal annealing. They stated that this phase was metastable and transformed to $Cu_{10}Zr_7$ and $CuZr_2$ at higher temperatures. The DIC traces were also integrated and fit to a modified[5] form of the Johnson-Mehl-Avrami-Kolmogorov (JMAK) model, Eqn. A.1, resulting in Avrami exponent, n, values between 2.2 and 2.4. Later studies, by mostly the same authors, reaffirmed the formation of a metastable monoclinic CuZr phase during isothermal annealing and reported n values of approximately 2.5, although the temperature(s) investigated were not specified [60, 61].

In addition to the CHR experiments summarized in Table A, a study by Pauly et. al. [58] also utilized isothermal annealing to investigate the devitrification kinetics of melt-spun $Cu_{50}Zr_{50}$. The authors fit a modified [7] form of the JMAK model to isothermal annealing data acquired at 701, 703, 705, 707, and 709 K and calculated activation energies of crystallization using the fitted parameters k and n. Unfortunately, only the average value of 3.6 for n was reported.

Even for the relatively low heating rate of 10 K/min, the initial devitrification was too rapid to allow Kalay et. al. [6] to resolve the early stages of phase evolution, particularly the order in which the phase(s) precipitated from the amorphous ribbon. The study presented in Appendix A [64] [8] features a more comprehensive investigation of the initial devitrification response of a melt-spun $Cu_{50}Zr_{50}$ glass by utilizing specific isothermal annealing temperatures for which the transformation is relatively slow. This permitted a more detailed measurement and analysis of the phase evolution kinetics and associated mechanisms via *in-situ* HEXRD measurements and electron microscopy of specimens that were quenched at various times during the annealing.

[7] The authors introduced a term, τ, associated with an incubation time: $f_C(t) = 1 - \exp\left[-\left(k[t-\tau]\right)^n\right]$

[8] Recently published in Metallurgical and Materials Transactions A

CHAPTER 3. DEVITRIFICATION OF $Cu_{50}Zr_{50}$ - ISOTHERMAL KINETICS

As indicated in Table A, relatively few isothermal devitrification studies exist for melt-quenched $Cu_{50}Zr_{50}$ and they tend to lack sufficient microstructural evidence to definitively characterize the structural evolution that occurs during the annealing process. Although these studies also tended to provide quantitative analysis of the crystallization kinetics, their reports generally lacked the detail necessary for making meaningful comparisons with other studies. In some cases kinetic model parameters were fit to thermal analysis data [1] but the values were not reported, and in most cases no comments regarding the fitting procedure were provided. Moreover, these studies often stated conclusions regarding crystallization mechanisms and morphologies based on the value(s) of fitted model parameters without proper justification, such as confirmation through microstructural analysis. The need for multi-method characterization for describing such complex phase transformations was demonstrated by two recently published manuscripts [6] [64] that together provide the most rigorous and complete description of the structural and phase evolution during the devitrification of $Cu_{50}Zr_{50}$ to date. The most recent of these manuscripts [64] [2] also introduced a new method for quantifying crystallization kinetics from thermal analysis data. The remainder of this chapter is focused on describing this procedure in detail. The magnitude and overall shape of thermal analysis measurements depends on a variety of factors, some of which are related to the specimen itself (such as its geometry, mass, and thermal history) while others are related to the specific instrument and heating steps that are used. Nonetheless, isothermal reactions measured by differential calorimetry (DSC, DIC, DTA, etc.) frequently exhibit bell-shaped signals superimposed on a relatively constant baseline signal associated with maintaining the temperature of interest.

[1] DSC - Differential Scanning Calorimetry, DIC - Differential Isothermal Calorimetry
[2] Included in Appendix A

Although numerous mathematical expressions are able to adequately model such nominally bell-shaped thermal analysis signals and include parameters that could directly quantify the time dependence of a particular transformation, the tendency in the literature is to quantify the kinetics based on the fraction of material that has transformed as a function of time according to the the Johnson-Mehl-Avrami-Kolmogorov (JMAK) equation:

$$f(t) = 1 - \exp\left[-(kt)^n\right], \tag{3.1}$$

where f is the volume fraction of material that has transformed, t is the elapsed time at the constant annealing temperature, and the model parameters, k and n, are taken as fitting constants. A common method for determining k and n from constant temperature data involves computing a normalized cumulative integral over the thermal analysis event (peak) that corresponds to the isothermal transformation of interest. A plot of the normalized cumulative integral of a bell shaped curve versus time is sigmoidal, equaling zero at the lower integration bound and equaling one at the upper integration bound. Such a curve can be fit to the JMAK expression, $f(t) = 1 - \exp\left[-(kt)^n\right]$, to determine the reaction rate constant, k, and Avrami exponent, n. This type of analysis assumes that the normalized cumulative integral corresponds with the time-dependent volume fraction of the system that has transformed. An alternative analysis involves plotting $\ln(-\ln(1-f))$ versus $\ln(t)$ and computing k and n from the slope and intercept of the log-linearized expression for $f(t)$: $\ln(-\ln(1-f)) = n\ln(k) + n\ln(t)$.

Although constant temperature thermal analysis measurements often seem to be ideally shaped for such analysis, they tend to exhibit features and artifacts that must be addressed in order to ensure that a fit is accurate. Perhaps the biggest challenge involves accounting for a non-constant baseline signal [3], even when an instrument background signal is subtracted. This is especially problematic when the transformation of interest occurs so rapidly that the measured signal associated with the instrument ramping to the isothermal holding temperature

[3] According to the JMAK expression, a valid cumulative distribution function, f should equal zero at $t = 0$, and approach one as t approaches infinity. Thus, df/dt is bell-shaped, equals zero at $t = 0$, and asymptotically approaches one as t approaches infinity. A DSC trace is not likely to share the second and third properties exactly in common with df/dt, even if we account for the trace approaching a non-zero constant (C). However, the signal surrounding a thermal event is often fairly constant during isothermal annealing, and such a trace can be approximated fairly well by a scaled and shifted form of df/dt.

overlaps the signal for the transformation of interest. This is usually not an issue for slower transformations where sufficient time is available for the instrument to establish a relatively constant baseline signal prior to, and after, the transformation of interest. In either case however, proper analysis requires careful truncation, since the fitting results for the methods described above are sensitive to the choice of integration bounds, as demonstrated in Figs. 3.2 3.4c-f. This is especially true for the log-linearization method, where the logarithmic plot is linear over a smaller range as the amount of truncation increases, as shown in Fig. 3.4e for the fitting of an actual isothermal data set. The nonlinear artifacts that arise in the logarithmic plot introduce the need to further limit the amount of data that is considered when constructing a line from which n and k are computed.

To avoid the complexities associated with data truncation, we have computed the JMAK parameters k and n from the raw isothermal DSC signals (with the exception of the 673.4 K data set, as we describe below). We begin by considering the time derivative of the JMAK expression, df/dt, which is essentially a probability density function for the cumulative distribution function $f(t)$. In order to approximate an isothermal DSC signal, $\dot{Q}$, we scale and shift $\frac{df}{dt}$ by the factors S and C, respectively. Thus,

$$\dot{Q} \approx S\left[\frac{df}{dt}\right] + C = S\left[(kn)(kt)^{(n-1)}\exp[-(kt)^n]\right] + C \tag{3.2}$$

Fitting [4] this expression to an isothermal DSC signal with a relatively constant baseline results in n and k values that i) are less sensitive to the extent of data truncation and ii) describe the DSC trace with high accuracy, as demonstrated in Fig. 3.4b and Fig. 3.5 for four different truncation scenarios. This method was applied to each of the raw [5] isothermal data sets shown in Fig. 3.3, resulting in fitted parameters that are plotted in Fig. 3.6 and listed in Table A.1. For each fitting, the corresponding data set was truncated such that only the points surrounding the isothermal peak down to one percent of the peak height were considered.

While we certainly cannot presume that the same set of nucleation and growth processes

[4] Via non-linear regression.

[5] With the exception of the 673.4 K data set, the thermal analysis data was not altered prior to data fitting. The 673.4 K data set warranted a background subtraction to remove a slight curvature that was imparted on the baseline by the instrument. This correction consisted of subtracting a signal that was measured under the same conditions as the 673.4 K ISO experiment, except in the absence of a specimen.

controls the devitrification response over the range of temperatures examined here, the general appearance of the transformation curves in Fig. A.2b does not indicate any dramatic changes in the operative mechanisms. However, we have no reason to expect that a single mechanism or even a single phase dominates the behavior, or even that any steady nucleation or growth rates prevail. Acknowledging these issues fully, we still elect, for convenience, to summarize the overall kinetics using the common exponential form of the JMAK formulation. We emphasize that this choice is intended only to provide an empirical description of our measurements. Moreover, we make no presumption that the value of any of the empirical fitting parameters implies a correlation to any crystallization mechanism. Rather, it is our assertion that such a correlation is not prudent here, given the complexity of the far-from-equilibrium transformation which consists of multiple nucleation mechanisms that are simultaneously active, as indicated by Figs. A.6-A.7.

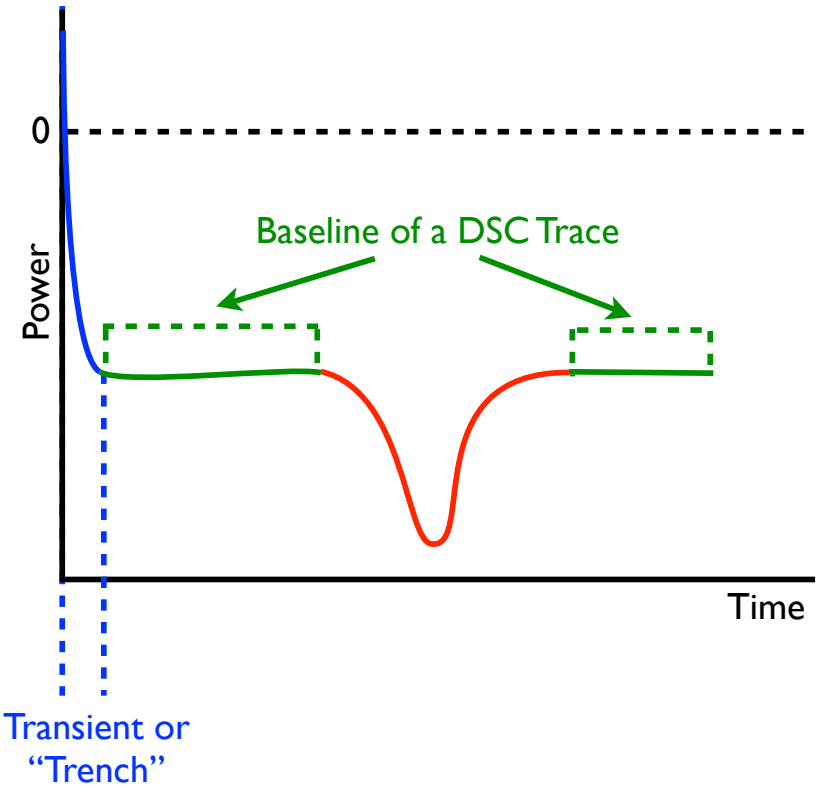

Figure 3.1 A schematic DSC signal for an isothermal transformation. The initial portion of the trace, shown in blue, is associated with bringing the instrument furnaces to the programmed annealing temperature. Care should be taken to ensure that a steady (flat) baseline signal, shown in green, is established before and after to the signal of interest. In this case, an exothermic event is depicted as a bell-shaped signal and downward deflections represent exothermic transformations.

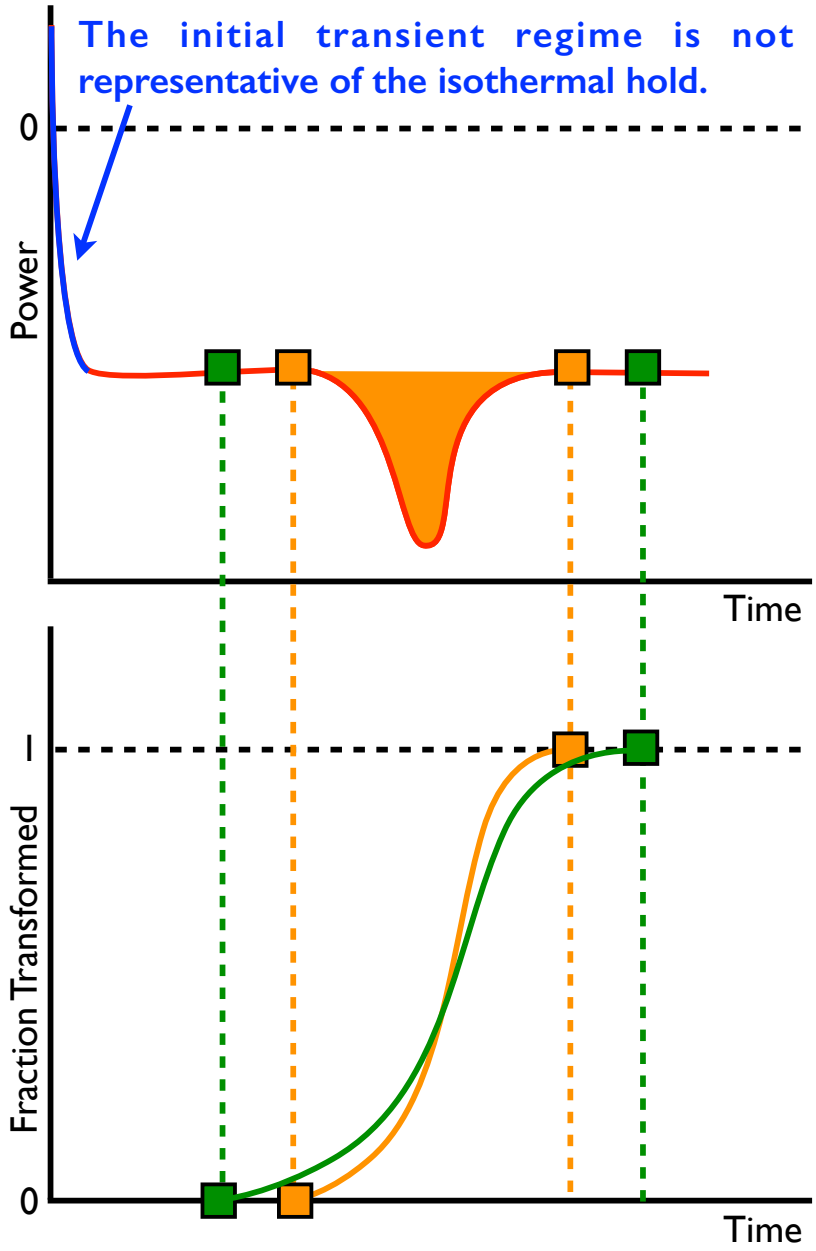

Figure 3.2 A schematic DSC signal for an isothermal transformation. The initial portion of the trace, shown in blue, is associated with bringing the instrument furnaces to the programmed annealing temperature. The choice of integration bounds influences the resulting fraction versus time curve which, in turn, influences the fitted JMAK parameters k and n.

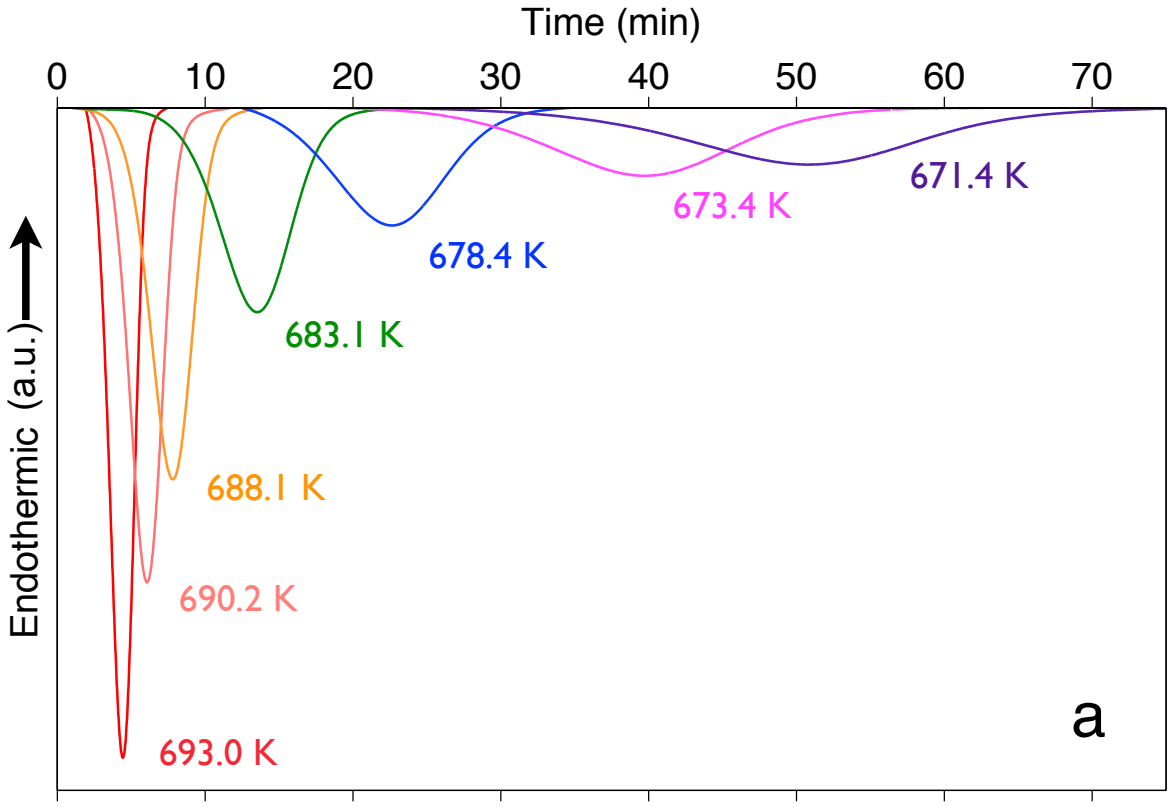

Figure 3.3 Isothermal DSC traces for the indicated temperatures, shifted to a common baseline in this figure.

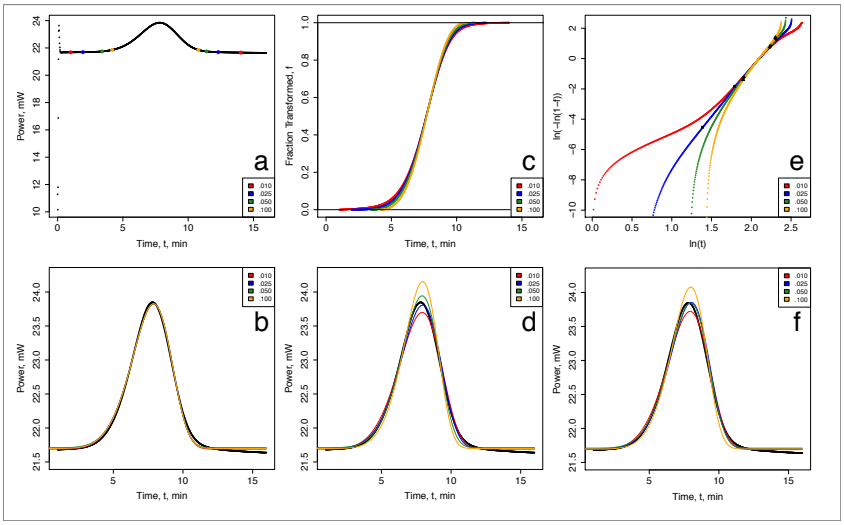

Figure 3.4 (a) Raw isothermal (688.1 K) devitrification data measured by DSC. Note the initial transient signal that persists after the program changes from a ramping (100 K/min) to isothermal mode. For mathematical convenience, we present the data here such that exothermic events result in positive deflections from the baseline signal. The indicated points denote the lower and upper bounds for the data truncation scenarios we consider for this demonstration. The fitted values that we report in Table A.1 are based on truncating the raw data to include only the points greater than one percent of the peak height on both sides of the peak (listed as .010 in this figure). (b) Approximated DSC traces constructed from the expression for $\dot{Q}$ using the JMAK parameters obtained by fitting portions of the raw DSC data directly. This was carried out for the various truncation scenarios and superimposed on the raw data (solid black curve). The plot has been rescaled to omit the data corresponding to the initial transient. Note that fits obtained in this manner are relatively insensitive to the range of truncation conditions investigated here. (c) The normalized cumulative integrals calculated from the raw data in (a) for the various truncation scenarios. Note that the plot and ultimately the fitted parameters, k and n, are sensitive to the values selected for upper and lower integration bounds. (d) Approximated DSC traces based on the k and n values obtained from fitting the curves in (c) to the expression for $f(t)$. They are plotted here using the same S and C values obtained for the direct fitting results of (a), since S and C values are not computed when fitting the fraction curves to $f(t)$. (e) Logarithm plot of the curves presented in (c). Note the increased nonlinearity as the extent of data truncation increases. (f) Approximated DSC traces based on the n and k values computed from the slope and intercept of the lines corresponding with the points indicated in (e). These points were arbitrarily selected such that they visually represented the largest linear portion of each plot. Again, S and C values for (f) were the same as those from the direct fitting procedure.

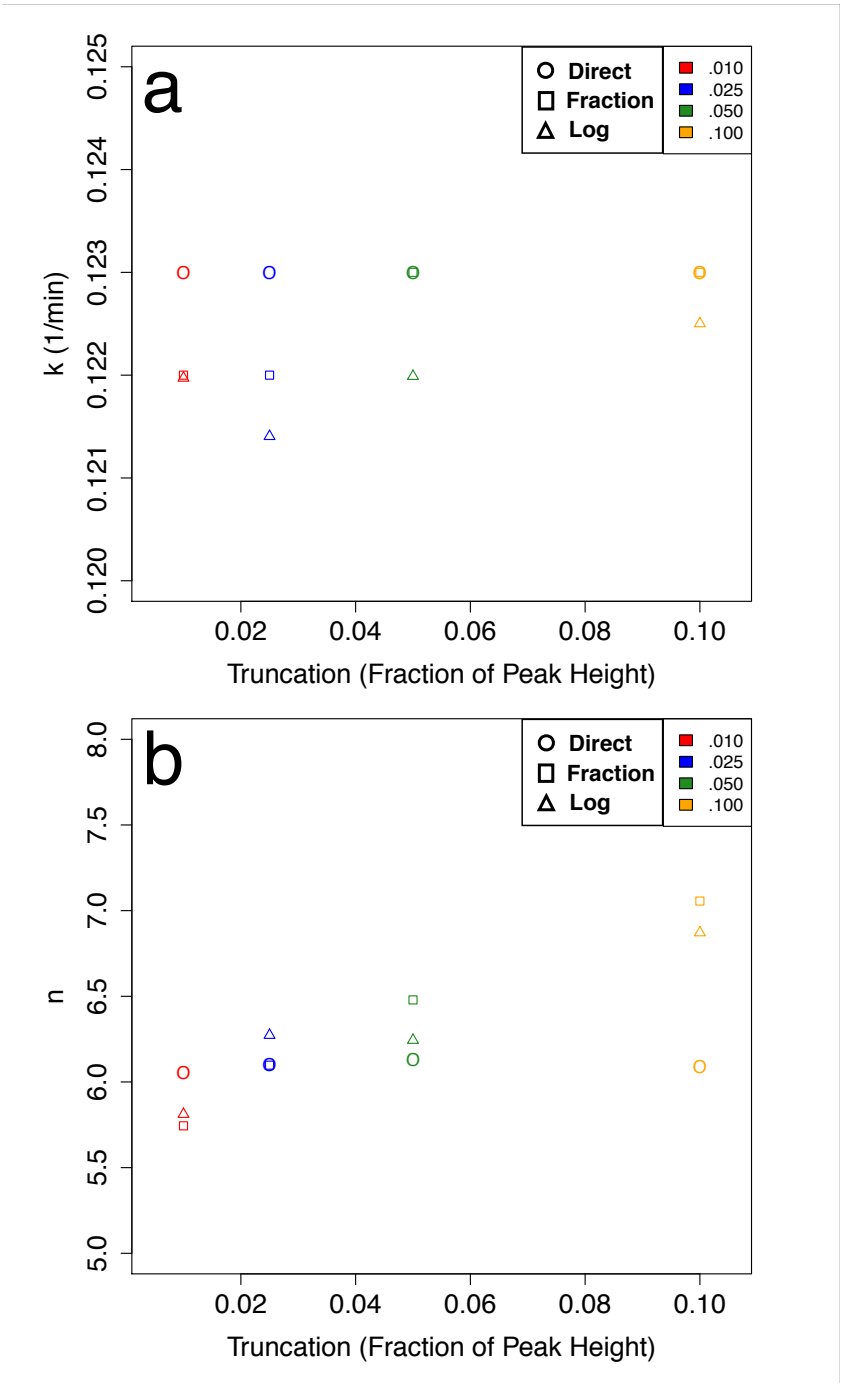

Figure 3.5 k (a) and n (b) values plotted versus the truncation value (fraction of peak height) for the various fitting types demonstrated in Fig. A.13. Direct (□) refers to fitting the raw, but truncated, DSC data to the expression for $\dot{Q}$ (see Fig. A.13a-b). Fraction (◯) refers to fitting the normalized cumulative integral (fraction curve) to the expression for $f(t)$ (see Fig. A.13c-d). Log (△) refers to computing n and k from the slope and intercept of normalized cumulative integral values presented on log scales (see Fig. A.13e-f).

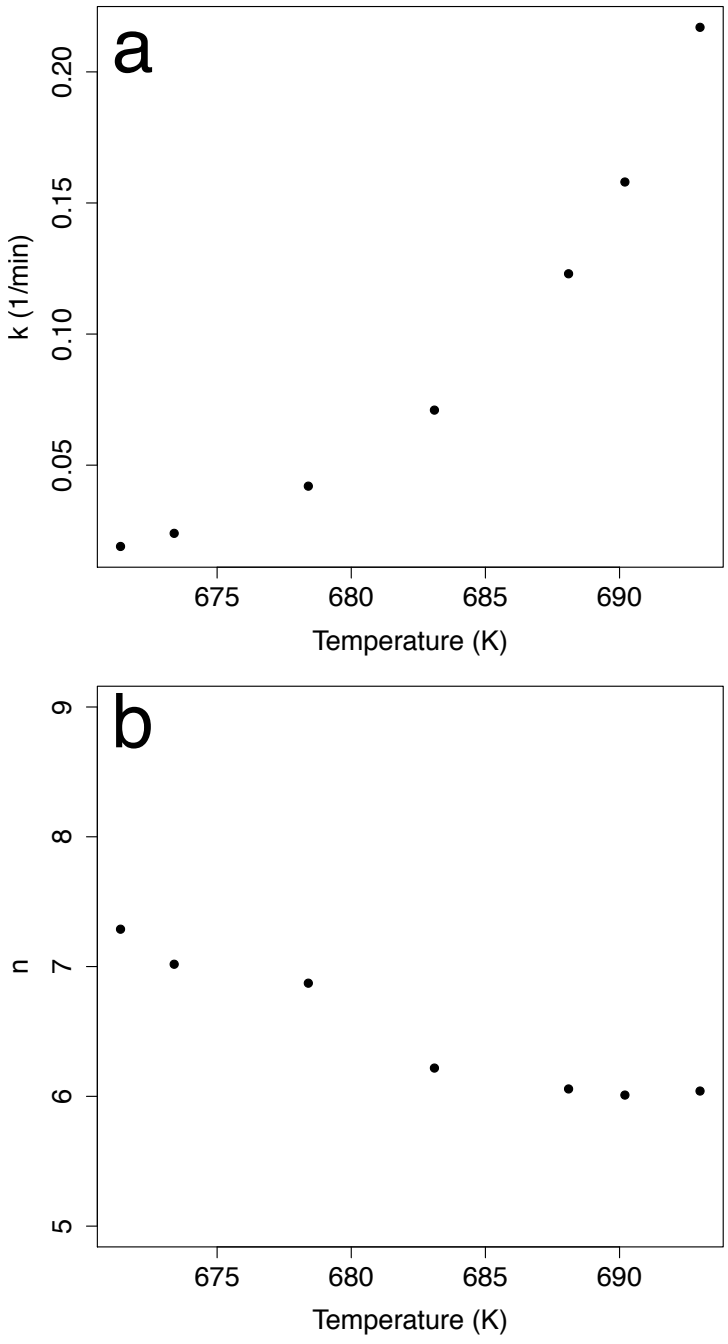

Figure 3.6 Plots showing the temperature dependence of the fitted JMAK model parameters k (a) and n (b), based on the data presented in Fig. 3.3.

CHAPTER 4. REVIEW OF ORTHO-TERPHENYL LITERATURE

This chapter features a brief chronology of studies pertaining to the properties and crystallization behavior of *o*-terphenyl (OTP), a transparent, organic, glass forming material. Upon melting (57°C), OTP forms a clear to slightly amber liquid that is remarkably resistant to crystallization and exhibits a drastic change in the temperature dependence of viscosity as it is cooled towards its glass transition temperature. As described in the following sections, OTP exhibits several anomalies with respect to its transport properties, thermal properties, and crystallization behavior.

Weiler - 1896 [66]

Weiler isolated several hydrocarbons during a study of the Wurtz-Fitting reaction including o-terphenyl (1,2-diphenylbenzene, OTP) , although it would go unidentified until the 1927 study by Bachman & Clark [67].

Bachmann & Clarke- 1927 [67]

Bachmann & Clarke isolated and identified OTP, reporting the melting and vaporization temperatures as 57°C and 332°C, respectively.

Birkett & Clews - 1937 [68]

Birkett & Clews grew large, colorless, prismatic crystals of OTP from methyl alcohol and petroleum ether. They measured a crystalline density of 1.166 g/cc in a $CaCl_2$ solution at 17°C. Through XRD measurements on the large single crystals, they deduced an or-

thorhombic space group of $P2_12_12_1$ and lattice parameters of $a = 18.6$ $\mathring{A}$, $b = 6.05$ $\mathring{A}$, and $c = 11.8$ $\mathring{A}$. Combining the density, lattice parameters, and molecular weight of an OTP molecule, they concluded that each unit cell contained four molecules. By comparing diamagnetic susceptibility measurements from the single crystals with computed susceptibilities based on possible molecular orientations within the crystal they deduced that, within the single crystals (i) neither of the side phenyl groups can be perpendicular to the central phenyl group, (ii) the most likely structure is one in which the two side phenyl groups are rotated about 50° relative to the plane of the central phenyl group, (iii) the vector bisecting the angle between the side phenyl group bonds is nearly parallel with the $\overline{a}$ lattice vector.

Allen & Pingert - 1942 [69]

Allen & Pingert published a detailed study of the synthesis and purification of OTP, noting that it can be readily separated from other polyaryls through solution recrystallization.

Karle & Brockway- 1944 [70]

Karle & Brockway studied the structure of OTP molecules in the vapor phase using electron diffraction and concluded that the phenyl rings were not coplanar, but rather orthogonal to the central phenyl ring on average. Independent deviations of the side phenyl groups could range up to ± 15°, but larger deviations would have to be in phase.

Good et al. - 1953 [71]

Good et al. reported that the liquid density of OTP decreases linearly from 1.22 to 0.62 g/cc between 70 to 150°C, and that it boils at 327°C. They also reported on the solubility of OTP with *p*-terphenyl (PTP, a molecular isomer to OTP), stating that a single eutectic point exists at a mole fraction and temperature of 0.0155 and 55.75°C, respectively. No solid solubility was detected by XRD measurements.

Andrews & Ubbelohde - 1955 [72]

Andrews and Ubbelohde reported on the vapor pressure, viscosity (η) and molar volume of OTP in addition to other polyphenyls. When $\log_{10}(\eta)$ is plotted against $(1/T)$, benzene, diphenyl, and *p*-terphenyl exhibited very linear trends, while PTP and, to a greater extent, OTP displayed significant departure from linearity, a behavior commonly associated with the formation of clusters and an increasing activation energy for viscous flow. Since OTP also exhibits a pronounced ability supercool, they proposed that the structure of such clusters must differ from aggregates that act as crystal nuclei. They also cite the unusually low ratio of the latent heat of vaporization to activation energy of viscous flow ($\Delta H_{vap}/E_\eta$) as further evidence of a "highly associated liquid", indicating that larger holes must form in the melt in order for molecular movement to occur.

They go on to mention that no evidence exists to suggest extensive deviations of the the angles between the phenyl group planes, and this rigidity must significantly influence molecular packing in the melt and the flow characteristics for OTP. Calculations of the volume required to rotate a polyphenyl molecule (diphenyl, PTP, MTP, and OTP) about three mutually perpendicular axes through its centroid and comparing this to the molar volume of liquid suggests that rotation of these molecules should be prohibited in the liquid state, especially near their respective freezing points, and that rotation should actually be prohibited up to the respective boiling points, based on thermal expansion data.

Greet & Turnbull - 1967 [7]

Greet & Turnbull [7] measured the specific volume of liquid and solid (crystal and glassy) OTP from the equilibrium melting temperature to below the glass transition temperature, which they report as approximately -30°C for "ordinary cooling rates". Mercury capillary and HCl solution dilatometers were used to measure the specific volume of the amorphous and crystalline samples, respectively. These results are stated to agree fairly well with

those of Andrews & Ubbelohde [72]. The melting temperature, T_m = 329 K (56°C, heat of fusion, ΔH_f = 4.05 kcal/mol, and heat capacities of liquid, glass, and crystal were measured with DSC. They also measured the viscosity of liquid OTP from 20 to -30° C and noted that when combined with the higher temperature data of Andrews & Ubbelohde, the temperature dependence of viscosity - over 10 orders of magnitude - fits very well to the equation:

$$\eta = A \exp\left[\frac{B}{(T - T_0}\right] \tag{4.1}$$

where $A = 4.65{\times}10^{-4}$, B = 689 K, and T_0 = 231 K.

Greet & Turnbull also reported on the crystallization behavior of OTP, stating that crystallization from the melt required slow cooling, and that nucleation was suppressed for samples that were undercooled to room temperature and thoroughly outgassed, delaying crystallization for up to several months. They also measured the velocity of the solid-liquid interface within liquid films between microscope and cover glass slides using an optical microscope with a temperature controlled stage. They noted a cylindritic [1] morphology and that the width of the comprising grains decreased with increased undercooling. At very large undercoolings between 50-60° C, the noted a roughening of the interface and the presence of thin filaments and plates protruding ahead into the liquid. **This is likely the first reported observation of the anomalous crystallization mechanism later described as glass-crystal (GC) growth [73].** [2]

Greet - 1967 [8]

Following the procedure reported by Greet & Turnbull [7], Greet [8] measured the crystal growth velocity in liquid films of OTP formed between glass slides on a temperature controlled optical microscope. Crystallization was induced in via seeding at the edge

[1] A two dimensional radial growth pattern often referred to as spherulitic throughout the literature

[2] The GC terminology is not utilized in the literature until coined in [73], and is instead frequently referred to as anomalous crystallization / growth because it persists for undercoolings deep into the glassy state.

film. This study includes the first photograph of the faceted [3] crystal-liquid interface associated with low to moderate undercoolings. The growth rate measurements were analyzed with respect to three different models of isothermal crystallization that were prevalent at the time and featured a similar set of assumptions. In each of these models, the growth rate G is proposed to depend on the rate that molecules attach to the surface of a growing crystal interface, which is assumed to be inversely proportional to the liquid viscosity:

$$G(T) = \frac{f(t)}{\eta(T)} \tag{4.2}$$

Thus, the distinguishing feature of each model is the temperature dependence of $f(T)$. Greet tests the theories by plotting G versus different expressions derived from the models to see whether or not any of them predict the temperature dependence of the the crystal growth velocity. The model employing a two-dimensional surface nucleation was least supported and was proposed to describe crystallization from the vapor more accurately compared to crystallization within a melt [74, 75, 76]. Within the range 60 K of undercooling investigated, no kinetic transition was observed as predicted by the theory of a diffuse interface [77, 78]).

Finally, the failure of a reaction rate model [79, 74, 80] to predict the growth velocities indicated that Stokes-Einstein relationship between diffusion and viscosity [4] may be an oversimplification, in that the relationship between the shear viscosity of the liquid and the rate at which molecules attach to and detach from the interface may not be related as simply as in other systems. Shear flow in glass-forming systems, for instance, may involve the cooperative motion of entire clusters compared to the attachment of a single molecule to the interface.

[3] Greet states that, regardless of whether growth occurs in a solution or the melt, growth along the shortest lattice vector, $\overline{b} = 6.05\ \mathring{A}$, dominates and the crystal planes forming the interface are of the type {110}.

[4] Describes the diffusivity, D, of a spherical particle with radius r through a liquid with a low Reynolds number. $D = \frac{k_b T}{6\pi\eta r}$

Greet & Turnbull - 1967 [81]

Greet & Turnbull [81] measured the heat capacity of liquid and crystalline OTP from about 220 through 340 K (-53 through 67°C) to calculate the configurational entropy, $S_c(T) = S^{Liq}(T) - S^{Cry}(T)$, in order to test a consequence of the Adam & Gibbs statistical-mechanical model of the liquid state: that the temperature dependence of viscosity, η of a glass-forming liquid should be:

$$\eta = A \exp\left(\frac{B}{TS_c}\right) \tag{4.3}$$

where A and B are constants. Comparison with previously measured data revealed that the viscosity of liquid OTP changes much faster with temperature than predicted by the Adam-Gibbs model.

McCall et al . - 1969 [15]

McCall et. al. studied molecular motions in OTP using pulsed nuclear magnetic relaxation to investigate self-diffusion coefficients and relaxation times. They note that OTP behaves as expected for a typical glass forming substance, and the NMR data resembles that of a high polymer, in that the relaxation times do not reach the lattice values until well below the glass transition temperature, which they interpret as local motions becoming dominant and long-range motions ceasing as the temperature is lowered. Upon heating of crystalline OTP, molecules are noted to be nearly immobile through the melting point. Fig. 4.2 cite shows the self-diffusion coefficients for OTP with the characteristic increase of activation energy at high undercoolings.

Chang & Bestul - 1972 [16]

Using adiabatic calorimetry, Chang & Bestul measured the heat capacities from 2-329 K (-271 through 56°C = T_m), 2-240 K (-271 through -33°C = T_g), and from 240 - 360 K

(-33 through 87°C) for crystalline, glassy, and liquid OTP, respectively. The noted that above 170 K (-103°C), the temperature dependence of the heat capacity for crystalline OTP was very close to linear.

Magill & Li - 1973 [9]

Magill & Li measured the crystal growth velocity of OTP to an undercooling of 75 K (-198°C) and reported a maximum in the temperature dependence of growth velocity of 36 μm/s at 312 K (39 C). They also noted that the growth rate is not described well by the Fisher-Turnbull model for crystallization [92].

Faceted crystals were observed at all temperatures and no change in crystal structure was observed, except for the entrapment of bubbles that tended to form at the tips of growing crystals, which accelerated their growth relative to the remaining interface.

Scherer et al. - 1974 [10]

Scherer et. al. measured the growth velocity of OTP for undercoolings between 2.5 and 75°C for material in the as-received condition and material that received 153 passes of zone refinement at 0.25 cm/hr (.69 μm/s). Although the zone-refining temperature gradient was not reported, the authors used a microscope equipped with a temperature gradient stage to select a velocity for zone refinement, noting that "cellular breakdown" occurred for rates velocities greater than 0.25 cm/hr. For the growth velocity measurements, they monitored the advance of the smooth, faceted, interface as it grew into the liquid contained between microscope slides. For undercoolings greater than 40°C, they noted a "dendritic-type" growth protruding ahead of the smooth interface and recorded these velocities as well, noting that they were much faster than the propagation of the smooth interface. These measurements are shown in Fig. 4.4, which also indicates that the growth rates of the extensively zone refined OTP were not significantly different than those for the

as-received state. Bubbles were noted to appear at the growing interface, even in purified samples despite extensive zone-refinement and subsequent degassing under vacuum.

Between $T_m = 55.5°C$ and 25°C, growing crystals were well separated and non-competitive, in that lagging crystals were not overgrown or otherwise pinched off, they merely maintained their relative positions. Between 20°C and 15°C, crystallization proceeded as a macroscopically smooth interface with adjacent crystals in closer proximity but still growing together with the same velocity. Decreasing the temperature from 25°C to 15°C caused initially lagging crystals to accelerate to the leading crystals, forming a smooth interface. When subsequently heated back to 25°C, the crystals separated and return to the isolated crystal morphology characteristic of that temperature range. The facet size and spacing exhibited no systematic variation with temperature, a wide range of sizes and spacings were noted for all temperatures that they were observed.

Below 15°C, small "pointed crystals" were observed to extend into the liquid ahead of the macroscopically smooth interface. As shown in Fig 4.4, these anomalous crystals grew much faster than the interface from which they originated. DSC of OTP specimens crystallized via the faceted and anomalous mechansims revealed that both morphologies exhibit the same heats of fusion, indicating that they are likely the same crystalline phase.

Aikawa et al. - 1978 [17]

Aikawa et. al. used X-ray diffraction of a single crystal of OTP to determine the lattice parameters and molecular conformation, reporting an orthorhombic unit cell ($a = 18.583$ $\mathring{A}$, $b = 6.024$ $\mathring{A}$, and $c = 11.728$ $\mathring{A}$) and twist angles of the side phenyl rings of 62.1° and 42.5° that help alleviate steric interactions between one another. Also, the carbons of the side phenyl groups that are bonded to the central phenyl ring are significantly displaced from the plane of the central phenyl ring in opposite directions. The noted that repulsion between the side phenyl groups stretches bonds C(1)-C(6) and C(3)-C(4), while the C-C bonds between the side and central phenyl groups are shorter than the corresponding bonds in biphenyl (see Fig. 4.5). Aikawa et. al. also mention that the B and C side

phenyl groups should rotate easily in the liquid state, with the C ring allowed to take rotains between 90±47.5°, while the rotation of B is more limited and depends on the conformation of C, and vice versa. As liquid OTP is supercooled further, a random distribution of rotation angles within the range of allowed liquid values is expected to persist into the glassy state.

Brown & Levy - 1979 - [18]

Using neutron diffraction, Brown & Levy determined the lattice vectors and molecular conformation using a single crystal of OTP. They reported an orthorhombic unit cell (a = 18.583 $\mathring{A}$, b = 6.024 $\mathring{A}$, and c = 11.728 $\mathring{A}$), and twist angles of 42.1° and 62.1° in the same sense relative to the coplanar configuration of all three phenyl groups within the molecule. Their results were consistent with the predictions that Clews & Lonsdale made based on diamagnetic anisotropy measurements.

Bartsch et al. - 1993 [19]

Bartsch et. al. measured the temperature dependence of the static structure factor $S(Q)$ of OTP and noted that, unlike simple liquids, the main peak consisted of two maxima. Cooling the liquid to T_g resulted in a significant increase of the peak height of one of the maxima, at 1.9 $\mathring{A}^{-1}$, which they associated with changes in short-range intermolecular structure up to 10-15 $\mathring{A}$, stating that changes in intramolecular order were temperature independent. The increase of this maxima was continuous with increasing undercooling and therefore discarded as the cause of dynamical anomalies that were reported to abruptly occur near a critical temperature of T_c = 290 K (17°C). [5]

[5]Decoupling of translational diffusion from shear viscosity, and thus an inability of the Stokes-Einstein relationship to satisfactorily describe attachment kinetics for $T < T_C$, as noted in [8].

Biswas - 1995 [82]

Using inelastic Raman scattering on acoustically levitated OTP droplets, Biswas reported qualitative changes in Raman spectra associated with intermolecular structural transformations and also monitored the strongest Raman intensities over continuous temperature range to determine the volume fraction transformation rates during crystallizaton. Upon melting, well defined peaks associated with scattering from the crystalline lattice (and the influence of thermal expansion and internal strain) merge into a broad band related to the vibrational density of states.

Hikima et al. - 1995 [11]

Hikima et. al. studied the crystallization of OTP using adiabatic calorimetry and optical microscopy and reported two different crystallization mechanisms that occurred over separate temperature ranges. For temperatures down to 255 K (-18°C, ΔT = 75°C) they observed crystallization proceeding in a faceted manner and measured the velocity of the interface advancement as a function of temperature (see Fig. 4.8). Between 250 and 220 K (T = -23 and -53°C, ΔT = 80 and 110°C) a fine aggregate of crystals exhibiting a smooth interface was observed. The temperature dependence of the crystal growth rate exhibits a discontinuity between the two regimes, as the rate abruptly increases by several orders of magnitude around 250 K (-23°C). X-ray diffraction of samples crystallized via both mechanisms were nearly identical, indicating that both mechanisms produce the same crystalline phase. Hikima et. al. specifically note that the anomalously fast growth ceases at 250 K (-12°C) and occurs over a temperature range that is completely separate from the "ordinary", faceted, growth at lower undercoolings.[6]

To reconcile the enhanced growth rates at high undercoolings, associated with the anomolous, compact, crystallization occuring below 250 K (-23°C) Hikima et. al. propose that subcritical nuclei (embryos) in the liquid ahead of the advancing crystal are rapidly incorpo-

[6]Recent studies revealed that the anomalous growth persists to higher temperatures in the form of fast growing fibers and whiskers, to about $1.15T_g$ (281 K, 8°C). [73]

rated into the crystal upon impingement due to the similar molecular packing, effectively reducing the interfacial free energy barrier associated with advancing the crystalline front. They refered to this mechanism as **homogeneous-nucleation-based (HNB) crystallization**, and, using classical nucleation theory, and geometric arguments, calculated the temperature dependence of crystal growth velocity. As shown in Fig 4.8 and commented by the authors, the maximum calculated growth rate of $10^{-12}\mu$m/s is 10 orders of magnitude smaller than the experimentally observed maximum of $\sim 10^{-2}\mu$m/s for the corresponding growth regime. Several of these authors would later publish similar studies on triphenylethylene and 3,3'-dimethoxy-4,4'-bis(2,2-diphenylvinyl)biphenyl and report better fitting by modifying their HNB theory such that the β relaxation process controls the nucleation rate [83, 84, 85, 85, 86]

Back et al. - 1996 [87]

Back et al. measured the melting and boiling points of OTP using DSC between 50 kPa and 1.4 Mpa and reported an enthalpy of vaporization of 50.62 kJ/mol, and a boiling point of about 345°C near 1 atmosphere.

Hikima et al. - 1998 [85]

Hikima et al. reported a micrograph of OTP crystallized at various temperatures near T_g (244 K, -29°C), showing the compact form of the anomalous growth they associated with a homogeneous-nucleation-based crystallization mechanism. Similar to their 1995 publication, they again report X-ray diffraction patterns indicating that the same phase is produced regardless of the crystallization mechanism, i.e. low-undercooling faceted crystallization or high-undercooling anomalous crystallization, however, the enthalpy of fusion were found to be lower for OTP that was crystallized at high undercoolings via the anomalous crystallization mechanism. They also revised their HNB theory in an attempt reconcile the poor fitting of their original calculations [11] by associating the β relaxation

process [7] as the governing process of embryo formation and also incorporating a "nucleation enhancement effect". Although these modifications result in much better agreement with experimental measurements of crystal growth velocity (by orders of magnitude), the overall trend is still not representative of the experimentally measured values.

Magill et al. - 2000 [88]

Magill et. al. revisit their 1973 analysis of the inability of the Stokes-Einstein equation to model the shear viscosity of supercooled liquids. In this publication, they report that the use of an Arrhenius equation and two Vogel-Fulcher- Tammann-Hesse (VFTH) [8] equations are required to fit the temperature dependence of viscosity for two glass-forming liquids (trinaphthylbenzene and *o*-terphenyl) over an extensive temperature range. They note that the "crossover" from one VFTH parameterization to the other coincides with the temperature at which the Stokes-Einstein relation becomes invalid.

Wu - 2006 [89]

To better understand the origin of reported discrepancies between predicted and measured growth velocities of deeply undercooled organic liquids, Wu et. al. measured the crystal growth rates of three indomethacin polymorphs. For a 50°C temperature range, down to T_g+19°C, each polymorph exhibited the same temperature dependence of u_r. Considering that each polymorph is expected to exhibit its own site-factor temperature dependence, the deviation of u_r from a constant value at low undercoolings seems to have liquid origin. For undercoolings below T_g + 19°C, two of the three polymorphs tranistioned to a fiberlike morphology.

[7] Here, the β process (or β relaxation process) is associated with the motion of molecules in between the crystalline embryos.

[8] $\exp[-C/(T - T_\infty)]$, representing the temperature dependence of the self- diffusion coefficient in the liquid-melt, which is often reported to be the governing mass transport process during crystal growth.

Konishi & Tanaka - 2007 [12]

For a crystal growing within a glass, Tanaka [90] proposed that the volume contraction associated with crystallization should induce a negative pressure on the glass adjacent to the advancing interface, providing free volume to nearby molecules, locally increasing their mobility, and thus enhancing the crystallization rate.

Later, Konishi & Tanaka [12] reported on enhanced crystallization for OTP and two different crystal forms of salol. Similar to previous studies by others, they measured the position of the advancing crystal-glass interface over time using an optical microscope with a temperature controlled stage. The samples were films prepared between to microscope slides. They observed a discontinuous increase of the crystal growth rate near T_g, consistent with previous studies, however the increase of Form I salol was greater than for Form II, which featured a smaller volume change on crytallization. The authors suggested that the abrupt increase of crystal growth rate below T_g is associated with the dynamic balance between the free volume created and the volume relaxation that occur during growth. They argued that hydrodynamic flow is only possible for the liquid, thus diffusion is the only mechanism by which the glass may relax any stresses that arise due to the volume contractions associated with crystal growth.

Sun et al. - 2007 [73]

Sun et. al. proposed the term "GC", standing for glass-crystal, to describe the anomalously fast growth rates that abruptly appear at low temperatures, near T_g, and persist deep into the glassy state. For certain polymorphs of the glass-former 5-methyl-2[(2-nitrophenyl)amino]-3-thiophenecarbonitrile (called ROY for short), they reported a morphological evolution similar to that for other systems that exhibited GC growth: growth of large, individual, faceted crystals at low undercoolings, growth of tightly packed, space-filling crystals, with a smooth interface at higher undercoolings, and a transition to a much faster compact growth for undercoolings below T_g (259 K, -14°C). They also noted that

the enhanced growth rates associated with GC are also present in the liquid, up to $1.15T_g$ (299 K, 26°C), in the form of fast-growing fibers. As shown in Fig. 4.9, the linear growth rates associated with the fast growing fibers are consistent with the trend for the growth rates of the compact form below T_g. Although this is the first account in the literature linking these two growth regimes, the fibrous growth morphology was briefly mentioned by Greet & Turnbull [7] and Scherer et. al. [10]. Like previous reports, growth rate measurements were made by observing the advancement of the crystal interface within a film of liquid/glass between two microscope slides, using an optical microscope with a temperature controlled stage.

Regarding the homogeneous nucleation based theory proposed by Oguni et. al. [11, 85] Sun et. al. point out that an abrubt increase in the homogeneous nucleation rate over the temperature ranges where GC growth is observed is unlikely, and that when GC growth is paused and later resumed [9] it is only observed at select locations, which would require that the homogenous nucleation exhibits spatial heterogeneity.

Sun et. al. also argue against the "tension induced mobility" explanation offered by Tanaka [90, 12], pointing out that the GC growth rate is constant over time at a particular temperature, and that a building tension would imply an acceleration of the growth rate. They also point out the observation of GC growth in the form of fibers in the liquid, which is capable of relaxing stresses quickly, in contrast to the claims by Tanaka et al. [90, 12] that the anomalous growth only occurs in the rigid glassy state. They mention that the β relaxation is common to both viscous liquids and glasses and merges with the α relaxation (bulk structural relaxation) around $1.2T_g$, which is approximately the temperature at which the transition from compact crystallite (spherulitic) growth to fibrous-GC growth is observed for both ROY and OTP.

[9] By temporarily raising the temperature of the sample.

Ediger et al. - 2008 [21]

Ediger et. al. [21] reviewed isothermal crystal growth models that originated from Frenkel [91] and Turnbull & Fischer [92], stating that such models are only empirically correct at small undercoolings, and fail to describe crystal growth rates for materials that exhibit substantial supercooling. Specifically, they mention that the assumption of proportionality between different metrics of mass transfer, such as D, D_r, and η^{-1} (the self-diffusion coefficient, rotational self-diffusion coefficient, and inverse viscosity, respectively) does not tend to persist to large undercoolings. They go on to compare reduced crystal growth rates , u_{kin}, with viscosity for 15 liquids and establish that, for a given glass-forming liquid $u_{kin} \propto \eta^{-\zeta}$ where $\zeta < 1$ and is highly correlated to the fragility index, m. In their analysis, u_{kin} is equal to $u/(1 - \exp[-\Delta G/RT]) \approx u/(1 - \exp[-\Delta S_m/R])$ where u is the observed growth rate, ΔG is the free energy difference between the liquid and crystal, and ΔS_m is the entropy of melting. Note that u_{kin} is able to predict the growth rates for high undercoolings, as demonstrated in Fig. 4.10. Fig. 4.11 illustrates that, for several classes of glass-forming liquids, $u_{kin} \propto \eta^{-\zeta}$ where $\zeta < 1$. Comparison with Fig. 4.12 reveals a correlation between ζ and m. Thus, crystal growth kinetics are shown to systematically depend on a property of that is strictly related to liquid dynamics. This finding is counter to the conventional perspective that crystal growth rates are controlled by the *crystal-liquid* interface through a function f describing the fraction of sites on the interface that are available for attachment. The failure of this perspective, employing common growth models is well documented [93, 94]. Ediger et. al. also point out the interesting fact that all three crystal forms of Indomethacin feature $\zeta = 0.76$, even though they exhibit substantially different interface structures. They argue that the slopes in Fig. 4.11 being less than 1 ($\zeta < 1$) implies spatially heterogeneous dynamics in the liquid, and they speculate that this is manifested as a decoupling of transport properties, i.e. local diffusivities, viscosities, etc. can vary substantially from location to location in the liquid. Such heterogeneity is expected to be less pronounced for strong liquids, such as SiO_2 which, in fact, features nearly identical temperature dependencies of self-diffusivity, viscosity, and kinetic growth rate.

Based on their analysis, Ediger et. al. offer the following *empirical* equation for the observed growth rate of glass- forming liquids:

$$u = \frac{a}{\tau_o}\left(\frac{\eta(T)}{\eta_o}\right)^{-(1.1-0.005m)} \exp\left(\frac{-\Delta S_m}{R}\right)\left[1-\exp\left(\frac{-\Delta G(T)}{RT}\right)\right] \tag{4.4}$$

where a is the lattice spacing, $\eta_o = 10^4$ Pa s, and τ_o is the structural relaxation time when $\eta = \eta_o$. Ediger et. al. emphesize that metallic liquids and polymeric liquids were not included in the analysis because (i) metallic systems generally solidify very rapidly when the composition of the liquid and crystal are the same (making viscosity measurements of the undercooled liquid difficult, and thus uncommon) and and they tend to exhibit nonlinear growth rates versus time when the compositions differ, and (ii) the molecular weight / polymer chain length influences the viscosity of polymeric materials more than the influence of temperature.

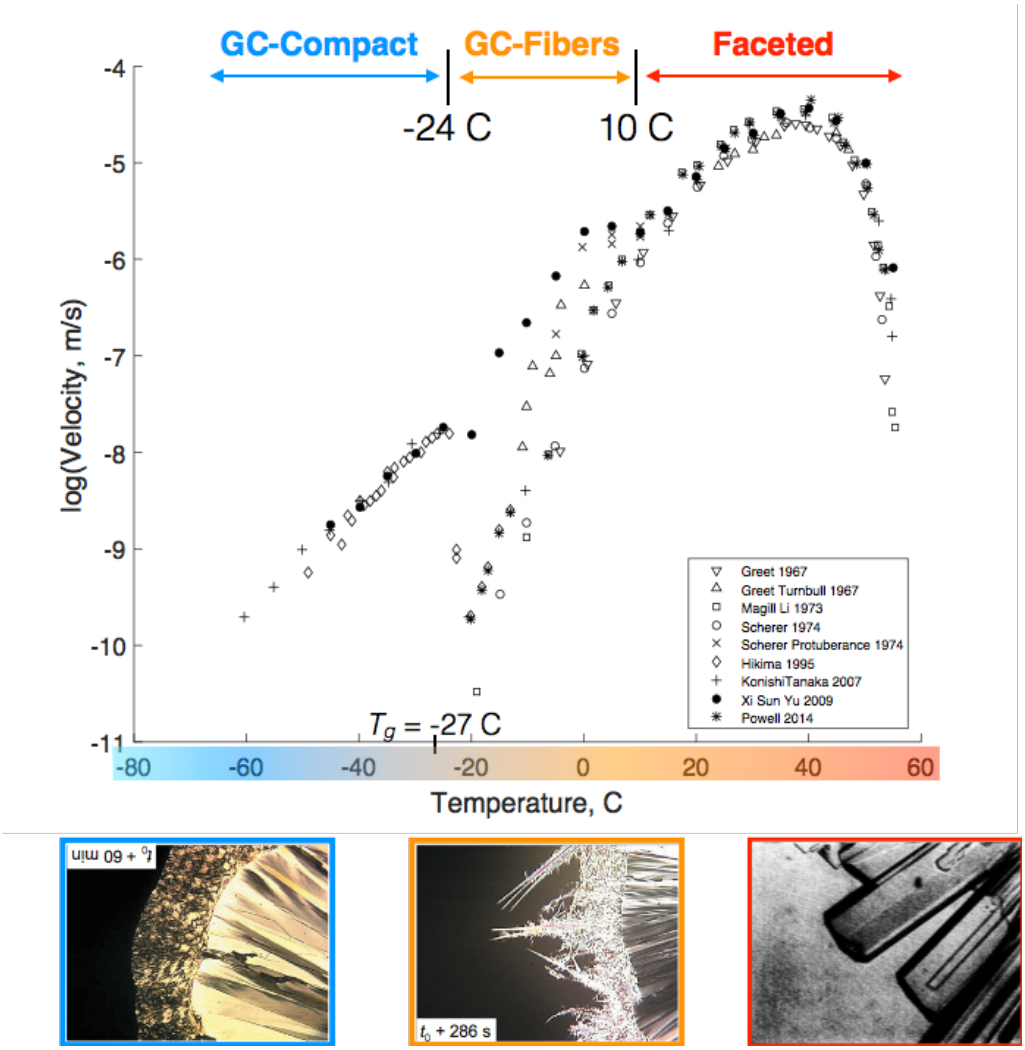

Figure 4.1 A summary of the glass-crystal growth studies for *o*-terphenyl under isothermal conditions [7, 8, 9, 10, 11, 12, 13, 14]. For low undercoolings, down to about 10°C, crystallization proceeds in a faceted manner [8]. The velocity of the smooth faceted front reaches a maximum of 45.7 micron per second around (40°C), and then decreases with further undercooling, due to the decreased molecular mobility (increasing viscosity) of the liquid. Around 10 °C, the glass-crystal growth manifests as individual fiber and whisker crystals protruding from the slower growing faceted front. As the undercooling is increased further, the glass-crystal growth is said to be fully activated and a compact form of growth ensues, which is also much faster than the advancement of the previously established faceted front. [13]

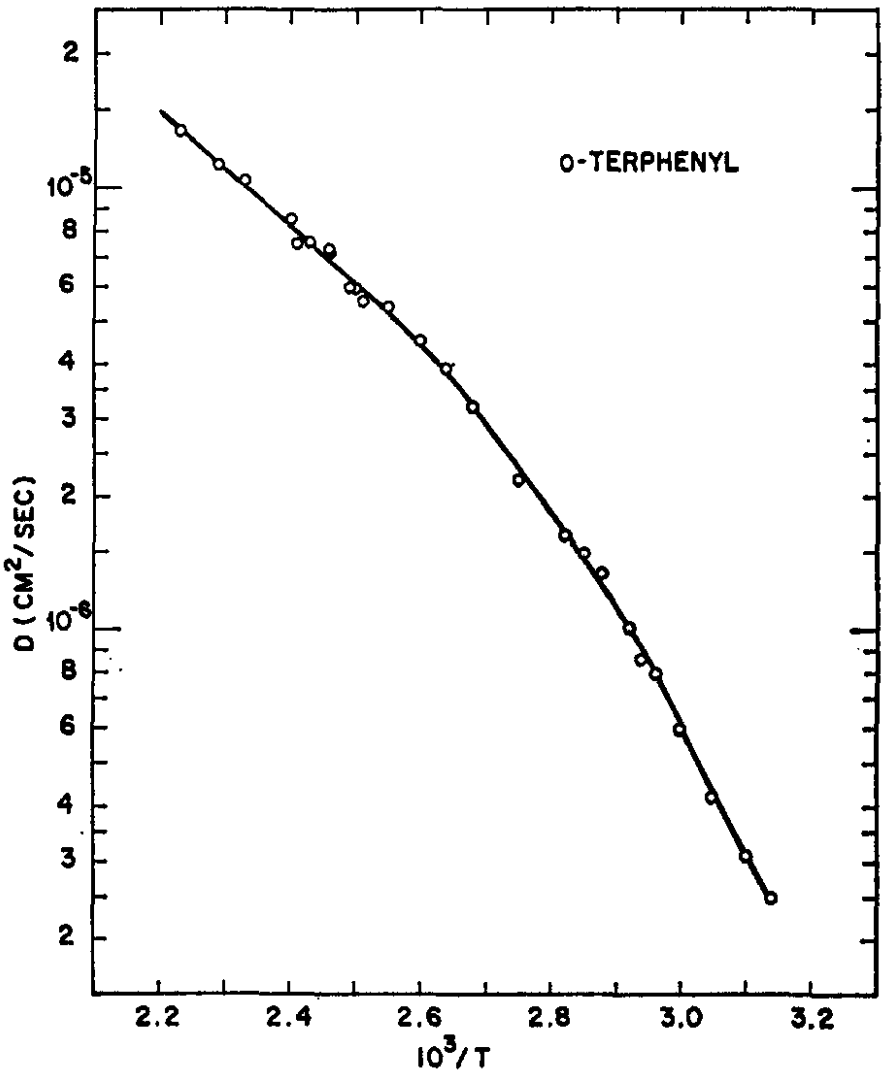

FIG. 2. Self-diffusion coefficients for *o*-terphenyl as a function of temperature.

Figure 4.2 As reported in [15].

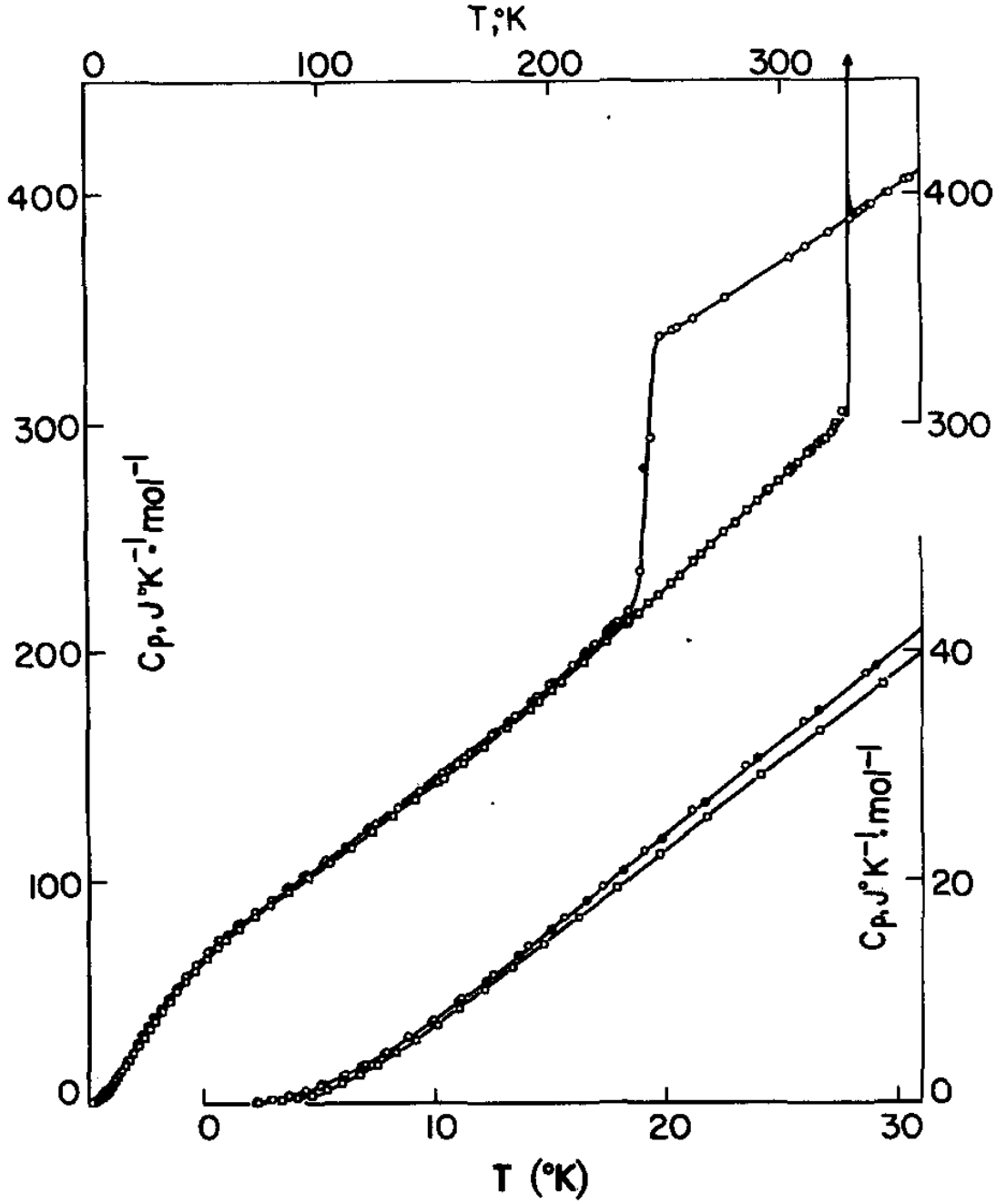

FIG. 1. Heat capacity of *o*-terphenyl: □, crystal; ●, annealed glass; ○, quenched glass and liquid.

Figure 4.3 As reported in [16].

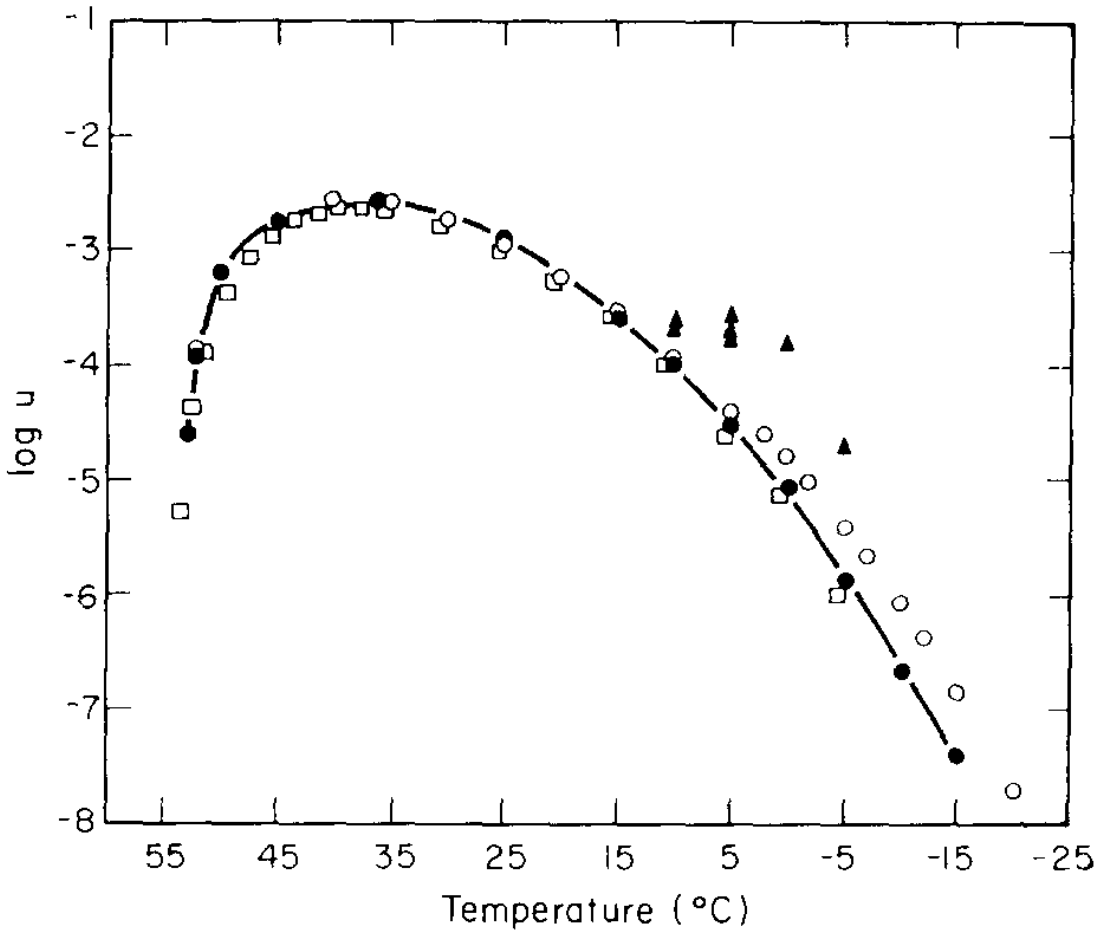

Fig. 3. Growth rate versus temperature relation for o-terphenyl: (○) as received; (●) ultra purity; (▲) protuberances ahead of flat interface; ( ) data of ref. 8.

Figure 4.4 As reported in [10].

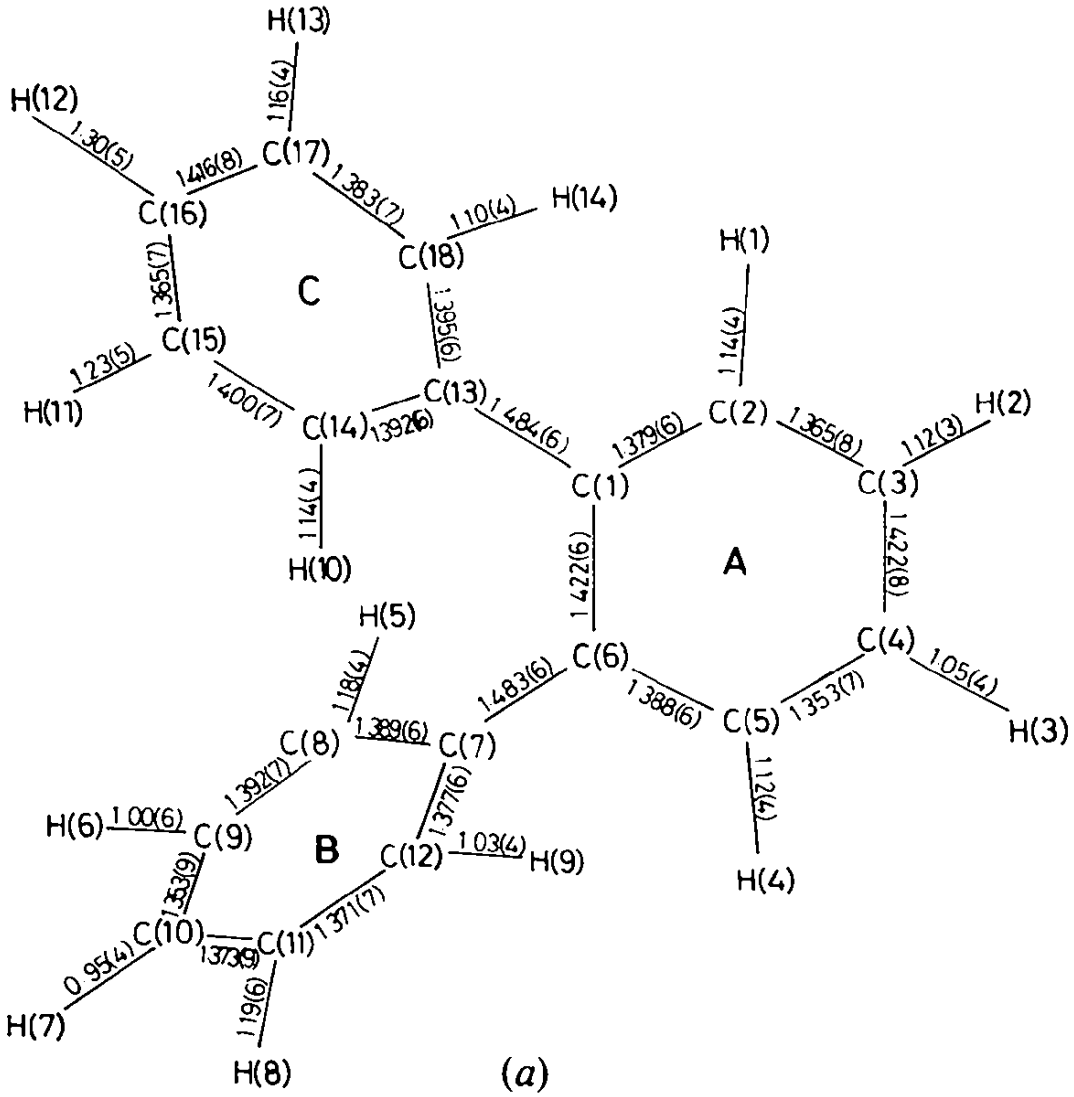

Figure 4.5 As reported in [17].

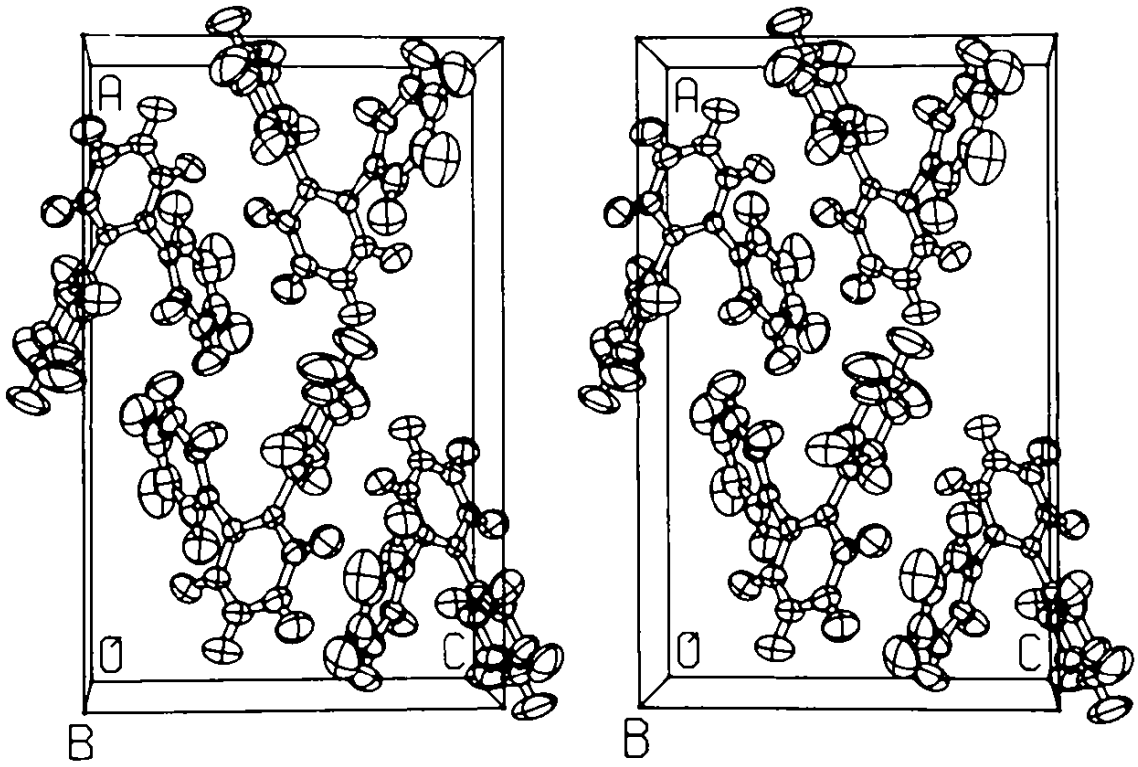

Fig. 1. Stereoscopic drawing showing the packing of molecules in the *o*-terphenyl crystal. Atoms are represented by their ellipsoids of 50% probability (Johnson, 1976). The shortest intermolecular distances (in no way unusual) are: C···C, 3·60; C···H, 2·82; H···H, 2·42 Å.

Figure 4.6 As reported in [18].

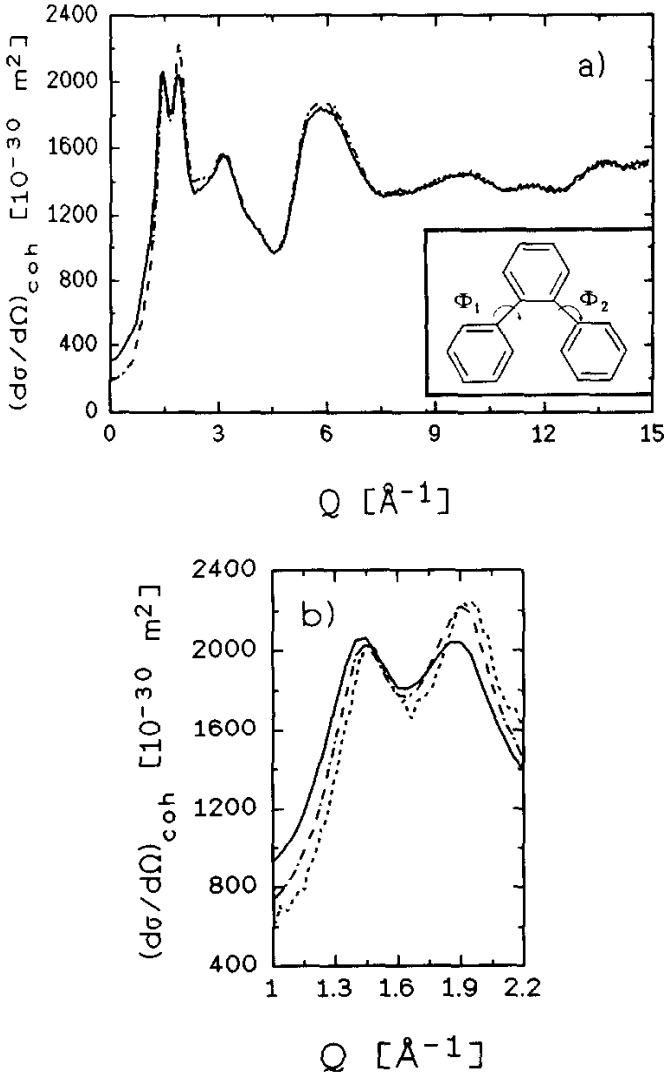

Fig. 1. Fully corrected static structure factor $(d\sigma/d\Omega)_{coh} \sim S(Q)$ of deuterated ortho-terphenyl at 314 K (——), 255 K (–·–·–) and 200 K (– – –; for clarity only depicted in (b)) as measured at the instrument D20 at the ILL, Grenoble. Note the increase at $Q = 1.9$ Å^{-1} with decreasing temperature.

Figure 4.7 As reported in [19].

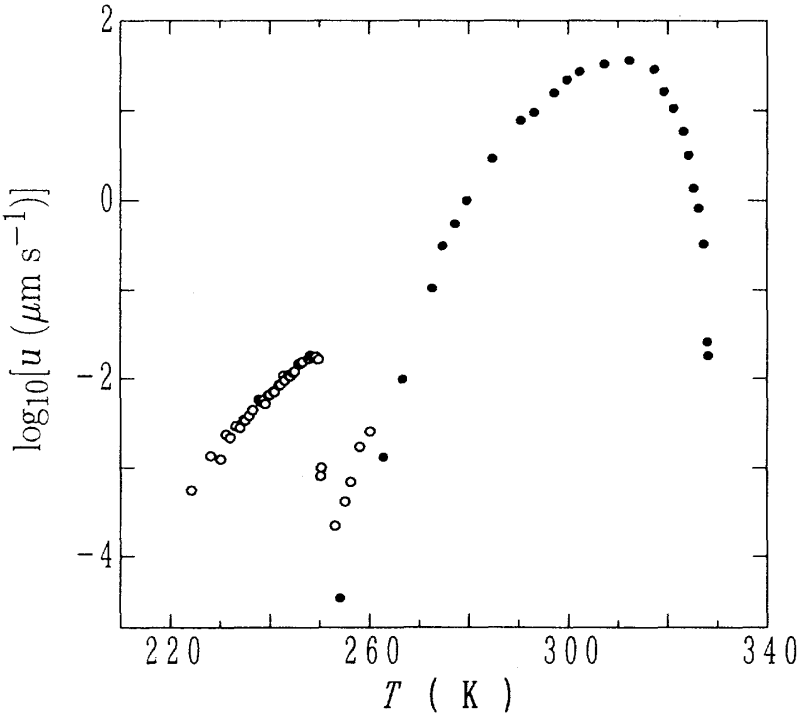

FIG. 8. Crystal-growth rate vs temperature relation for *o*-terphenyl: ○ data obtained in this work; ● data from Ref. 13.

Figure 4.8 As reported in [11].

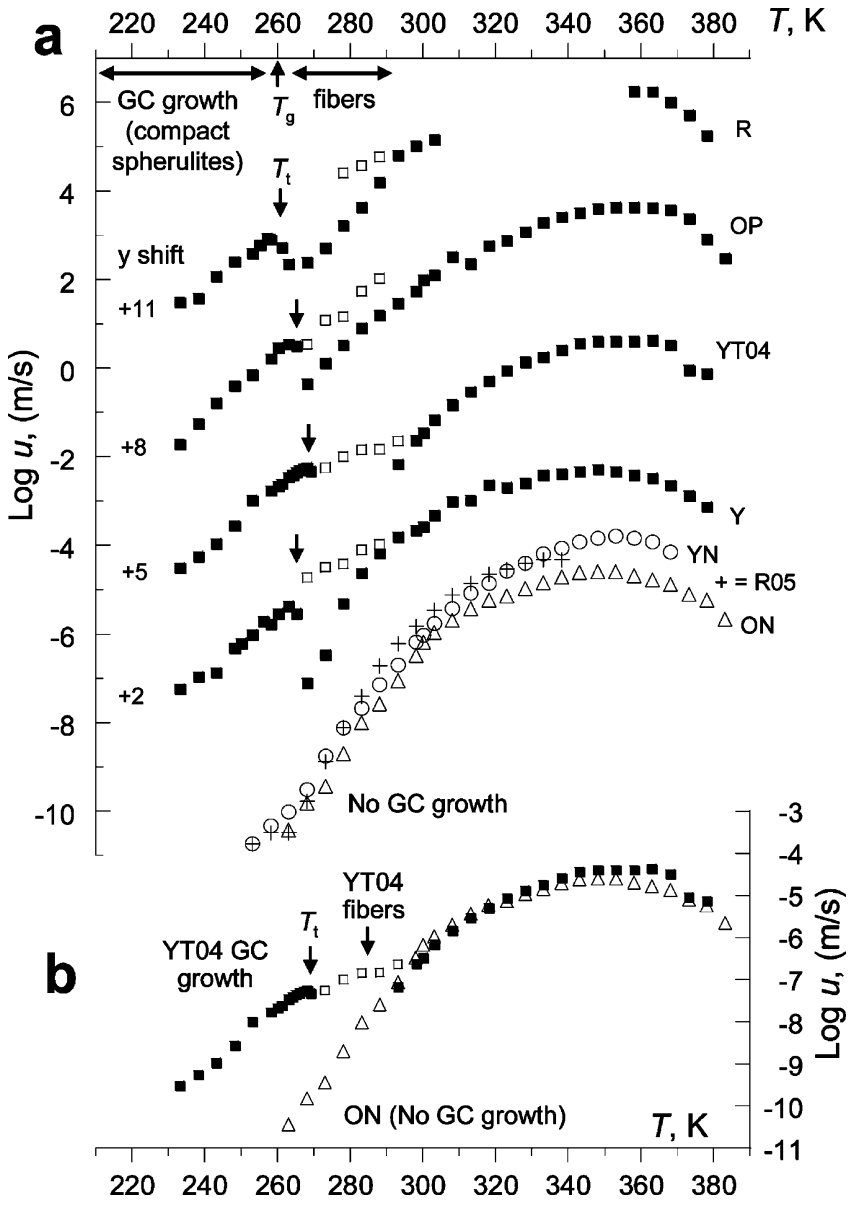

Figure 4.9 As reported in [20]: "Growth kinetics of ROY polymorphs in offset(a) and overlay (b) views. For clarity, the overlay compares only one polymorph (YT04) that shows GC growth and another (ON) that does not. "□" are growth rates of fast-growing fibers. Data points below log(u) = -10 are upper bounds. The growth of R05 could not be measured above 340 K because of polymorphic conversion and the fast growth of YN."

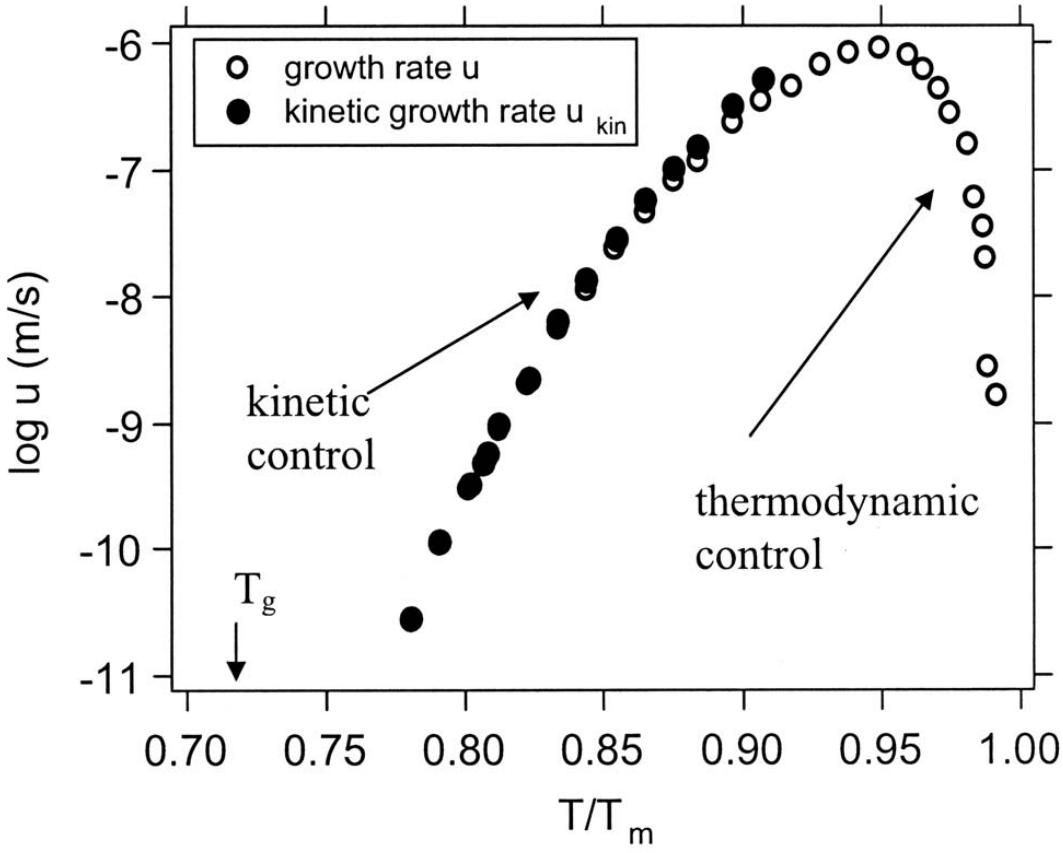

FIG. 1. Experimentally measured crystal growth rates for supercooled tris-(naphthylbenzene) (Ref. 3). Near T_m, the growth rate is controlled by the thermodynamic driving force for crystallization. As T_g is approached, mobility in the liquid limits the rate at which the crystal can grow. Using Eq. (1), growth rates for the low temperature regime can be corrected to yield the kinetic part of the growth rate u_{kin}.

Figure 4.10 As reported in [21]

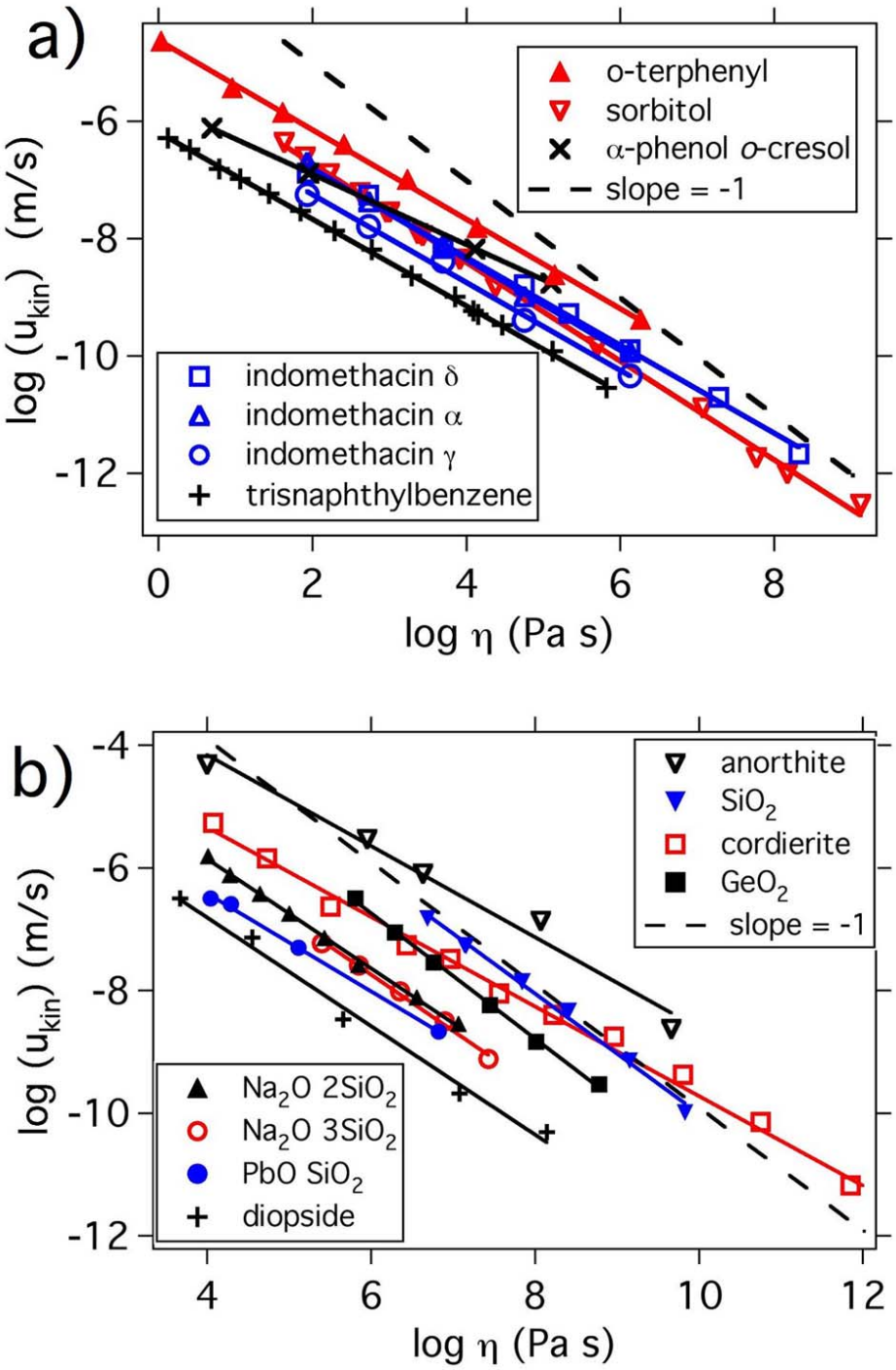

FIG. 2. (Color online) The crystal growth rate, corrected for the thermodynamic driving force, plotted against the supercooled liquid viscosity η for (a) organic and (b) inorganic liquids. In all cases, the data are well described by a straight line in the log-log format, usually with a slope significantly less than unity. References for growth rate data, viscosity, and thermodynamic parameters are given in Tables I and II.

Figure 4.11 As reported in [21]

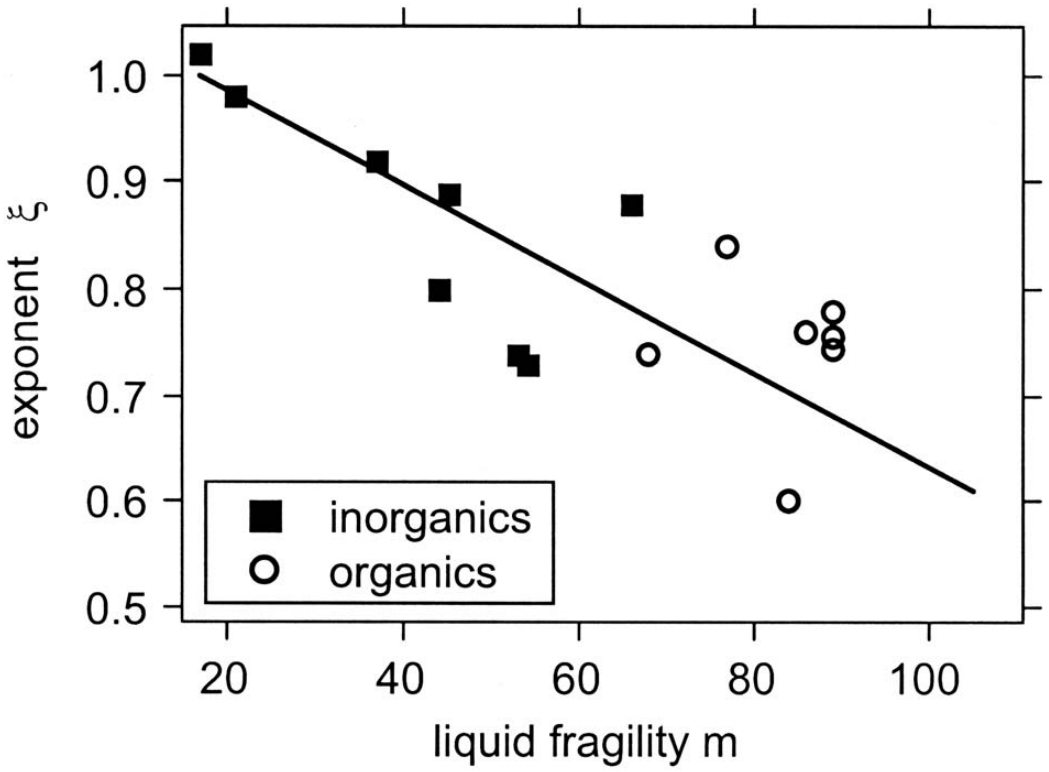

FIG. 3. The exponent ξ, representing the dependence of crystal growth rates on viscosity, plotted as a function of the supercooled liquid fragility. The fragility m is calculated from the temperature dependence of the viscosity, with references given in Tables I and II. The line is a guide to the eye. The typical uncertainty in ξ is 0.05.

Figure 4.12 As reported in [21]

CHAPTER 5. LOW-TEMPERATURE DIRECTIONAL SOLIDIFICATION APPARATUS

5.1 Background

At present, only eleven materials are reported to exhibit the anomalous crystallization behavior at high undercoolings (GC growth) that begins as fast growing individual whiskers and fibers just above T_g and transitions to a compact growth with a smooth interface below T_g. These organic glass-forming materials are summarized in Table 1.2. Although there is no specific set of characteristics that allow prediction of whether a material will exhibit GC growth or not, a few general trends exist amongst those that do, namely those featuring i) molecules with one ore more phenyl rings and/or a propeller / 3-fold symmetry, ii) non-close-packed crystal structures, iii) and a high entropy of fusion, which often manifests as faceted crystal growth [95].

Greet & Turnbull provided the first report of GC growth in 1967 for OTP [7], noting thin filaments and plates protruding from the previously established smooth interface for undercoolings greater than 50°C ($T < 7$°C). Their study also included the first report of isothermal crystal growth velocities for OTP. Since then, OTP has become the most studied material that exhibits GC growth, partly due to its unusually high glass transition temperature (-30°C). Isothermal crystal growth velocities have been reported in several different studies, through experiments that use an optical microscope with a temperature controlled stage to monitor the time required for a seeded crystal to advance a known distance within a film of liquid OTP contained between microscope slides. In all of these cases, the reported temperatures correspond to that of the microscope stage. The compiled results from isothermal growth studies are shown in Fig 4.1.

Although the crystallization rates of OTP measured under such "isothermal" conditions are consistent, the method is limited in that the temperature within the specimen - and more importantly at the solidifying interface - is unknown. Latent heat is liberated at the interface during solidification, which warms the surrounding liquid. This heat must diffuse away such that the surrounding liquid is colder than the advancing solid in order for solidification to proceed. Thus, in the experiments described above the reported temperatures - those corresponding to the microscope stage - may not correspond with the temperature of the solidifying interface. For this reason, a low-temperature directional solidification apparatus was constructed that is capable of studying the crystallization rate by translating a specimen through a known thermal gradient with a known constant velocity and measuring the temperature at the interface after it has established steady state growth. Solidification within a thermal gradient is also advantageous because (i) heat, including latent heat, is directed away from the interface through the solid versus towards the adjacent liquid where it could accumulate and further influence the crystallization rate, (ii) the thermal gradient and specimen slide geometry tend to produce aligned growth morphologies, (iii) the thermal gradient tends to suppress non-planar growth modes which can facilitate interface temperature measurements and (iv) complex motion profiles may allow access to transient states that would be difficult or impossible to achieve under other conditions, where the growth velocity is not an adjustable parameter. The remainder of this chapter describes the design and construction of a low-temperature directional solidification apparatus for studying solidification of low-melting point materials.

5.2 General Description

Similar to previously reported Bridgeman-type designs [96], this apparatus allows for the independent control of a temperature field and its uniaxial motion relative to a specimen slide that is fixed in the laboratory frame. As shown in Figs. 5.2 and 5.3, a movable insulating enclosure featuring heated and cooled metal blocks, or zones, surrounds the specimen slide over a portion of its length between its ends, which are supported by posts. The supporting posts and the bottom surfaces of the channel that passes through the enclosure and metal blocks are the same height, so that the specimen slide is in good thermal contact with the hot and

cold zones that dictate the thermal field. The enclosure assembly is attached to a linear servo motor that enables relative motion - typically constant-velocity displacements - between the thermal field and the stationary specimen. A microscope and camera assembly mounted to an independent two-axis motorized stage is also attached to the linear servo, allowing adjustments to the field of view that are independent of motion occurring on the primary servo axis. This entire apparatus rests on a self-leveling table and is surrounded by a Lexan polycarbonate shield to limit the influence of ambient air currents on the temperature profile.

5.3 LTDS Equipment Specifications and Capabilities

5.3.1 Linear Servo Motor

The motor that provides primary axis motion is a Parker 404LXR series linear servo. The complete model number tags and corresponding specifications are listed in Table 5.1. The accuracy of the encoder was independently checked for velocities of 1, 10, and 100 micron per second by viewing motion across a calibrated scalebar using the microscope and digital camera attached to the servo, in the configuration shown in Fig. 5.4. To calculate instantaneous velocities, the 0.1 mm distance between divisions was divided by the time elapsed between the arrival of division marks to the field of view. For each velocity, measurements from the left, middle, and right side of the servo were collected. The average measured velocities were 0.98, 9.99, and 100.48 with standard deviations of 0.17, 0.18 and 6.50, respectively. In its present service condition, this linear servo model can provide velocities down to at least 0.1 micron per second. The bearings of the motor mechanically limit the maximum velocity to 3 meters per second, although the encoder resolution further limits this to 0.3 meters per second. Ultimately, the true maximum velocity will depend on service conditions such as the load which must be translated and resistances to motion. This particular motor has been routinely operated at 100 mm/s, which far exceeds the needs of most directional solidification experiments.

5.3.2 Optics & Digital Camera

The optics of the LTDS apparatus consists of a Navitar 12x series zoom lens that provides a right-angle light path between an infinity-corrected long working distance objective lens and 12.8 megapixel Olympus DP-72 color CCD camera. Coupled with a solid-state hard drive equipped desktop computer, full frame color images can be steadily acquired up to about 13 frames per second.

5.3.3 Thermal Field

The thermal field is produced by flowing hot and cold fluids in closed loops between temperature controlled recirculating baths and the hot and cold zones, respectively. The heat transfer fluids for the hot and cold zones are an ethylene glycol & water mixture (.30 vol % ethylene glycol) and MultiTherm 501, respectively. The lower and upper limits for these cold zone and hot zone fluids are -30°C and 260°C, respectively. The power-limited temperatures of the identical recirculating baths are about -10°C, and 185°C. The FEP (Fluorinated Ethylene Propylene) tubing that serves as the fluid conduit features lower and upper service temperature limits of -75° C and 205°C. Thermal gradients up to about 5°C are attainable, although the several factors will determine the specific temperature profile, including the magnitude of the fluid temperatures reaching the hot and cold zones, the spacing between the zones, the thermal contact between the specimen slide and the hot and cold zones, the thermal conductivity of the slide / specimen, etc.

Table 5.1 Specifications for the linear servo motor.

Series	Travel	Model	Mounting	Grade	Drive Type	Home Sensor
404	T05	LXR	M	P	D13	H3
	200 mm		Metric	Precision	8 Pole Motor	No Current Seeking (Normally Open)
Limit Sensor	Cable Management	Z Channel Location	Encoder Option	Environmental	Digital Drive	Pinning Option
L2	CM05	Z3	E4	R1	A6	P1
Nc Current Seeking (Normally Closed)	3.0 m OEM Cable Set GEM	Center Position	0.1 µm Resolution	Strip Steel		No Multi-Axis Pinning

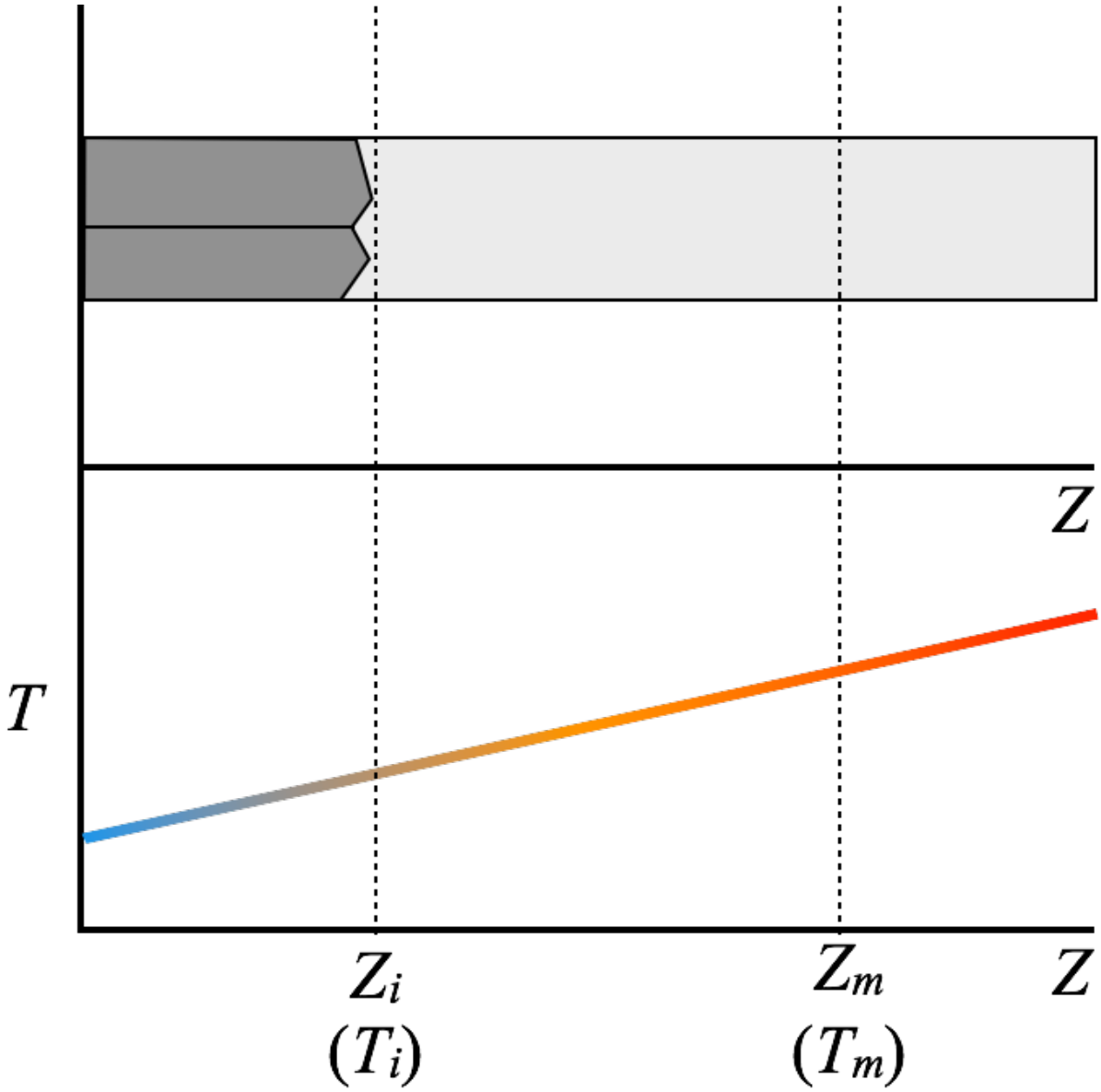

Figure 5.1 A schematic of steady state directional solidification. Initially, a thermal field is established and the portion of the specimen at temperatures greater than the melting temperature (or liquidus temperature for alloys) melts. Once an equilibrated solid-liquid interface has been established, a constant relative velocity between the thermal field and specimen slide is imposed. The interface will recede towards colder temperatures. If the interface appears stationary with respect to the thermal field, it is growing at the same rate as the imposed velocity, at an undercooling given by $T_m - T_i$.

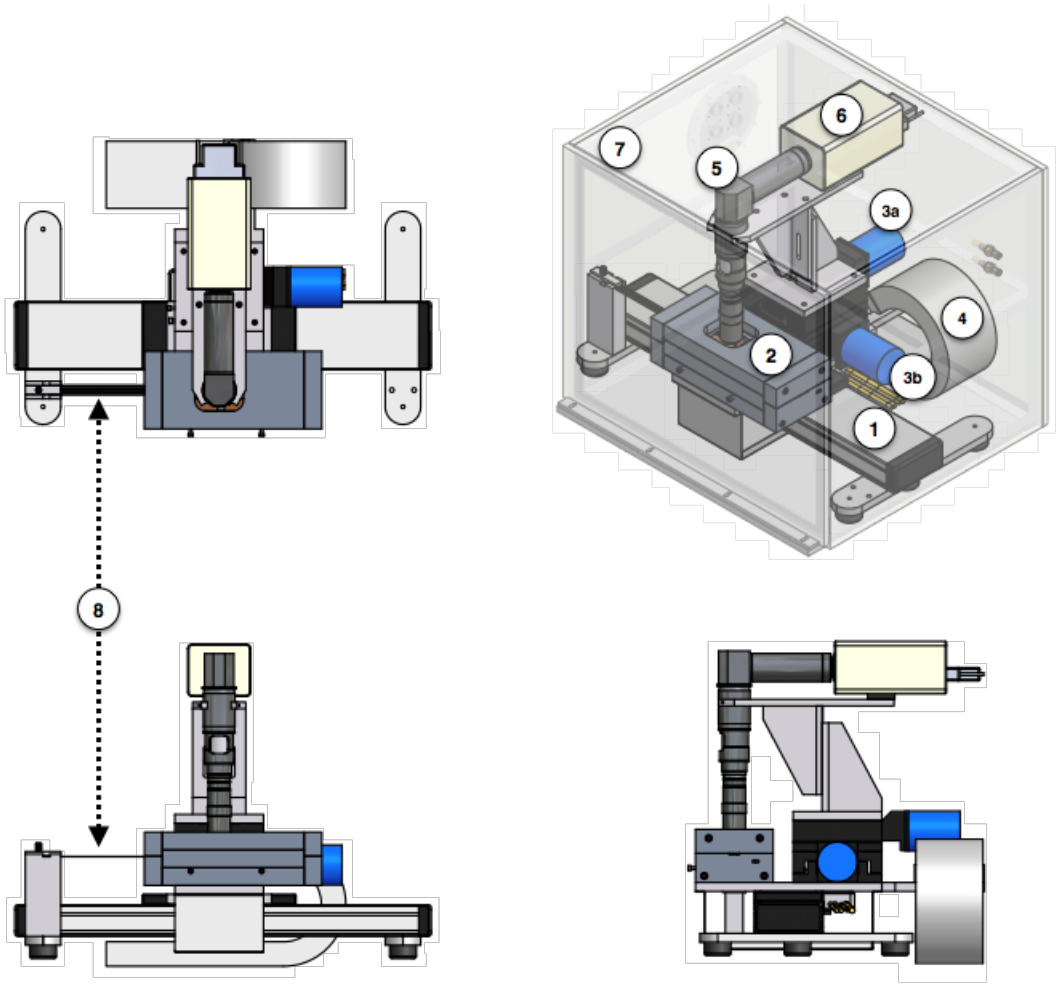

Figure 5.2 Computer drawing of the low-temperature directional solidification apparatus. 1 - linear servo (primary axis), 2 - thermal field enclosure, 3a,b - stepper motors attached to a two-axis stage that manipulates the microscope field of view, 4 - cable carriage, 5 - microscope optics with right angle adapter, 6 - digital camera, 7 - Lexan polycarbonate enclosure, 8 - stationary specimen slide.

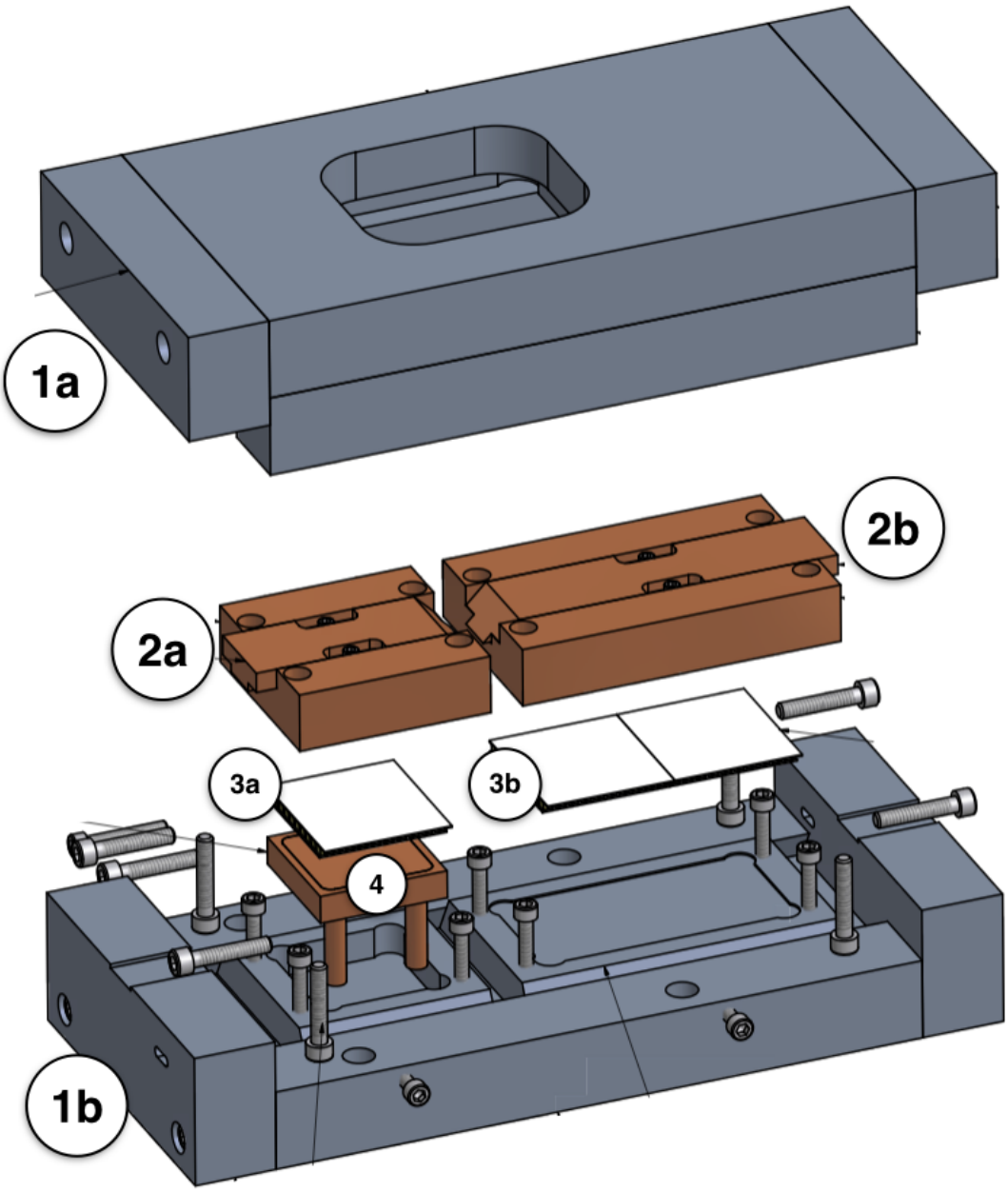

Figure 5.3 A computer-drawn exploded view of thermal field enclosure. 1a,b - Insulating housing, 2a - cold zone, 2b - hot zone, 3a - cold zone thermoelectric pad, 3b - hot zone thermoelectric pad, 4 - cold zone auxiliary fluid cooling pad.

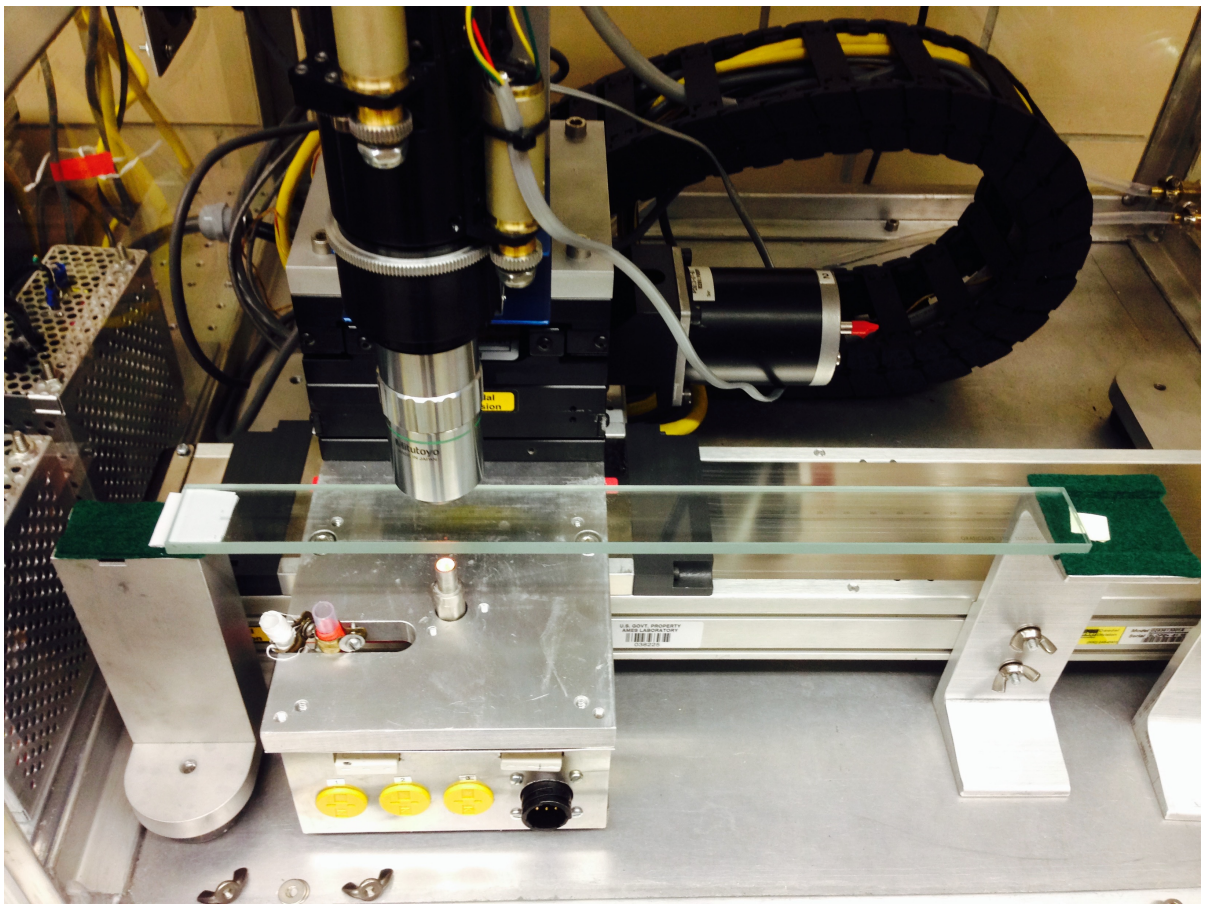

Figure 5.4 The setup used to verify the accuracy of programmed servo velocities. The glass slide features 300 mm of 0.1 mm divisions.

CHAPTER 6. PURIFICATION OF O-TERPHENYL

400 grams of 99% purity *o*-terphenyl (OTP = 1,2-diphenylbenzene, CAS 84-15-1) was purchased from Sigma Aldrich (Vendor Lot # MKBJ3853V). The as-received OTP was in the form of white crystalline plates but formed a viscous yellow liquid upon melting in air. Two different techniques were employed in an attempt to purify the OTP, namely, distillation and solution recrystallization.

6.1 Vapor distillation.

The distillation apparatus, shown schematically in Fig. 6.1, consists of a boiler flask, distillation column, glass thermometer, condenser, collection flask, heat tape, and a vacuum system. The heat tape was set to 320° C, the recirculating condenser fluid set to 40°C, and the distillation glassware was evacuated to -30 mm Hg by temporarily opening the vacuum valve. After a few minutes, the 20 gram charge of as-received OTP melted and formed a yellow liquid in the boiler flask. The vacuum valve was then slowly opened a slight amount, causing the liquid to slowly boil. About eight minutes later, a vapor cloud had developed and condensation was noted on the inner walls of the boiler flask and condenser, which slowly dripped into the collection flask to form a yellow liquid. The OTP dripped from the condenser to the collection flask at a rate of 1-2 drips per second for about an hour and fifteen minutes, leaving only a small pool of brown liquid in the boiler flask.

6.2 Solution recrystallization.

200 grams of as-received OTP were slowly melted in a beaker on a hot plate, forming approximately 200 mL yellow liquid. 1700 mL of 45°C methanol was added to the beaker

100 mL at a time until the OTP was completely dissolved. The OTP-methanol solution in the beaker was allowed to free-cool to room temperature, and then placed in an ice bath for approximately 12 hours. The next day, about 150 grams of very fine needle-like crystals were collected via vacuum filtration.

6.3 Purity analysis - Gas Chromatography & Mass Spectrometry

6.3.1 Background

GC-MS is a method of chemical analysis that relies on gas-chromatography and mass spectrometry measurements to identify chemical species within a sample. Typically, a material of interest is dissolved in a standard solvent, evaporated, and subsequently injected to a gas chromatograph, or column, by flowing an inert carrier gas over the solution. The column is a coil of very fine hollow tubing that features a polymeric coating on its interior. Once the vaporized sample + solvent + carrier gas mixture, referred to as the analyte, enters the column, the individual chemical constituents interact with the coating in different ways. Specifically, the rate at which the carrier gas flow pushes different chemical species through the column depends on their relative adsorption strengths, which is highly dependent the size/mass and shape of the chemical species. Thus, chemically distinct species in a sample are collected into separate packets that travel through and emerge from the column at different times. Acquiring mass-spectra as a function of time and comparing to a library of standard spectra allows the identification of chemical species in a sample. For this work, an Agilent 6890 GC-MS was used to qualitatively investigate the relative purities of OTP in as received, vapor distilled, and solution crystallized states.

6.3.2 GC-MS Sample Preparation Protocol

Step 1 - Preparation of Internal Standard

5.12 mg of eicosane was dissolved in 500 mL of methylene chloride. All sample solutions utilized this stock solution as a solvent to ensure that the concentration of the eicosane internal standard is uniform throughout all of the subsequently prepared samples.

Step 2 - Preparation of solutions for quantifying impurities

54.48 mg of as-received, 50.53 mg of vapor distilled, and 55.84 mg of solution crystallized OTP were placed into separate 25 mL volumetric flasks and constituted using the stock solution prepared in Step 1.

Step 3 - Preparation of sample vials for GC-MS

Approximately 1.5 mL of each solution were placed into glass GC-MS vials and immediately capped using separate disposable glass pipettes. The vials were then loaded into the GC-MS auto-sampler carousel.

Step 4 - GC-MS Method

GC-MS was carried out according to the standard operating procedure, with the exception of the injection volume being 2 microliters, split 50:1, rather than 1 microliter.

6.3.3 GC-MS Results

Fig. 6.6 shows the gas chromatograms for each of the OTP conditions that were investigated, and reveals the presence of four detectible impurities in the as-received and vapor distilled OTP. Comparison of the mass spectra acquired during the impurity peaks with a library of standard mass spectra indicated that the impurities were, in decreasing concentration, $C_{15}H_{12}$ 1-phenylnaphthalene, $C_{15}H_{12}$ 2-phenylindene, $C_{12}H_{14}$ biphenyl, and $C_{16}H_{14}$ endo-*o*-phenylenenaphthalene 1,2,3,4-tetrahydro- . The persistence of thes impurities after vapor distillation is not surprising, considering that at least two of them, 1-phenylnapthalene and biphenyl, have vapor pressures [22] that are similar or significantly greater than the vapor pressure of OTP near the distillation temperature of 320°C, as shown in Fig. 6.7. It is likely that the very fine crystals that grew slowly from solution feature less of the trace impurities because i) the trace impurities were redistributed over a much larger volume in solution, decreasing their probability of encountering a growing OTP crystal and ii) the slow-growing and

very fine scale crystals are less accommodating of impurity entrapment. The lack of impurity peak detection on the gas chromatogram of solution crystallized OTP suggests that its purity was improved over the 99% purity advertised by the manufacturer, although a quantitative measure of the purity was not investigated. Fig. 6.8 shows melting endotherms for OTP in each condition, measured by DSC. OTP in the as-received and vapor distilled conditions exhibited very similar melting behavior while the melting point was raised about 2°C for OTP that was crystallized from solution, consistent with the impurity levels measured via GC-MS, since impurities are often assumed to lower the freezing point of a substance. All subsequent work with OTP specimens utilized solution crystallized OTP.

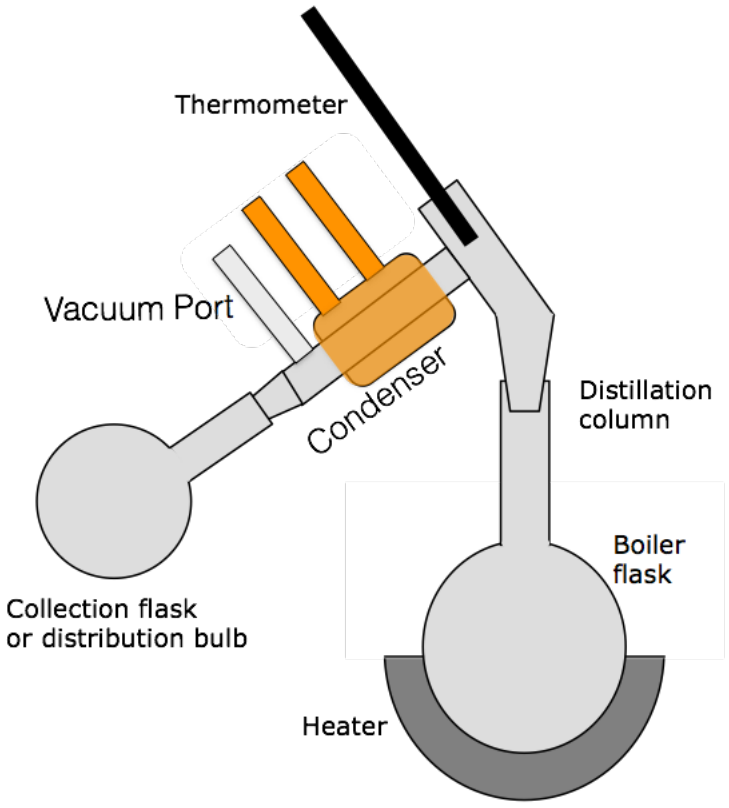

Figure 6.1 A schematic of the glassware used for the vapor distillation apparatus.

Figure 6.2 A photograph of vapor-distilled OTP condensing and accumulating in the collection bulb.The boiler flask is surrounded with heat tape and insulating wool. The orange condenser fluid is a 50-50 by volume mixture of water and antifreeze.

Figure 6.3 The 150 gram collection of fine OTP needles that crystallized from methanol.

Figure 6.4 A magnified view of the OTP needles that crystallized from methanol.

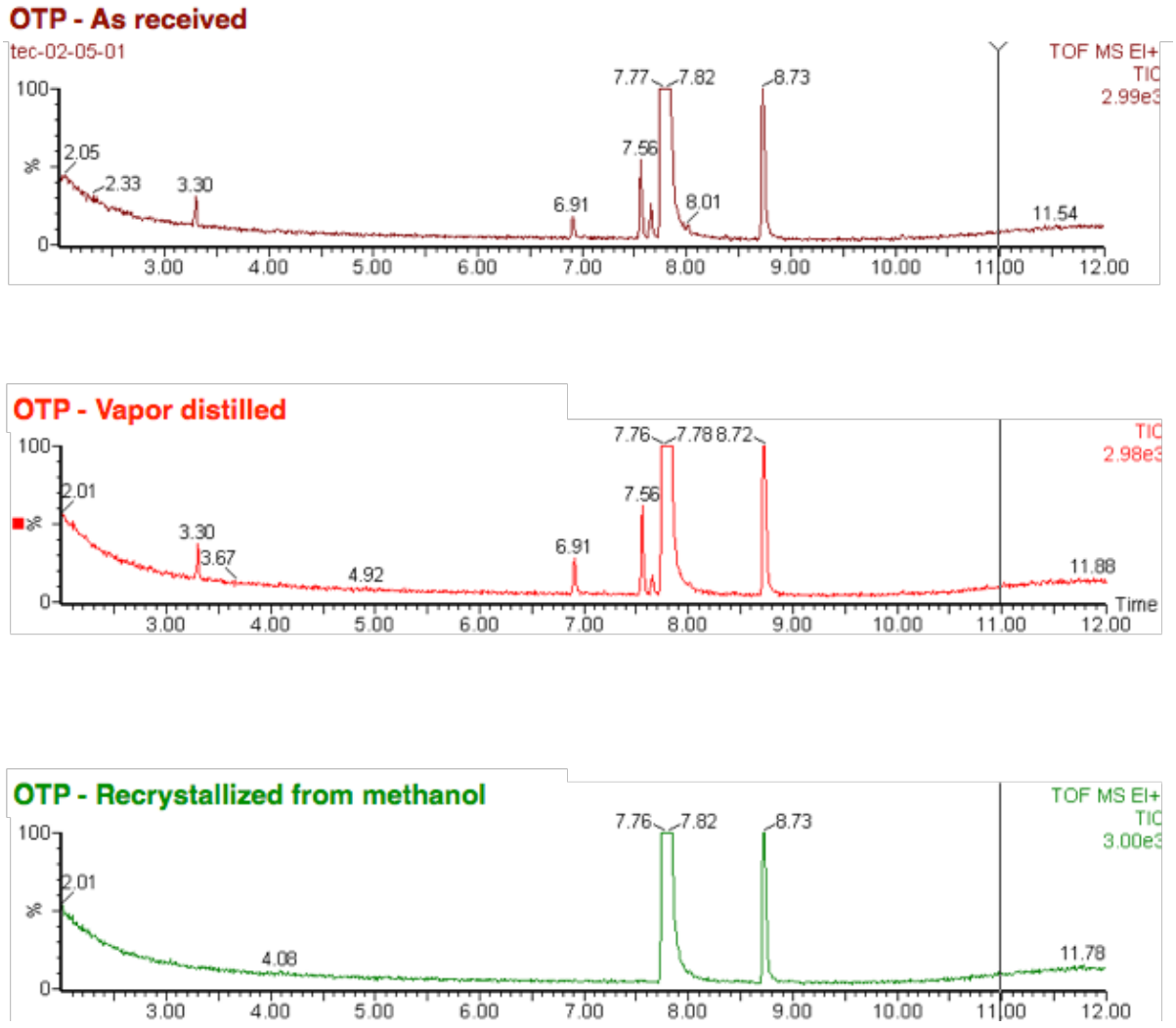

Figure 6.5 A comparison of GC chromatographs for the different OTP conditions. As-received and vapor distilled OTP featured the same four impurities (identified in Fig. 6.6), which were not detected in the solution crystallized OTP. x-axis: minutes, y-axes: percent, normalized Total Ion Current.

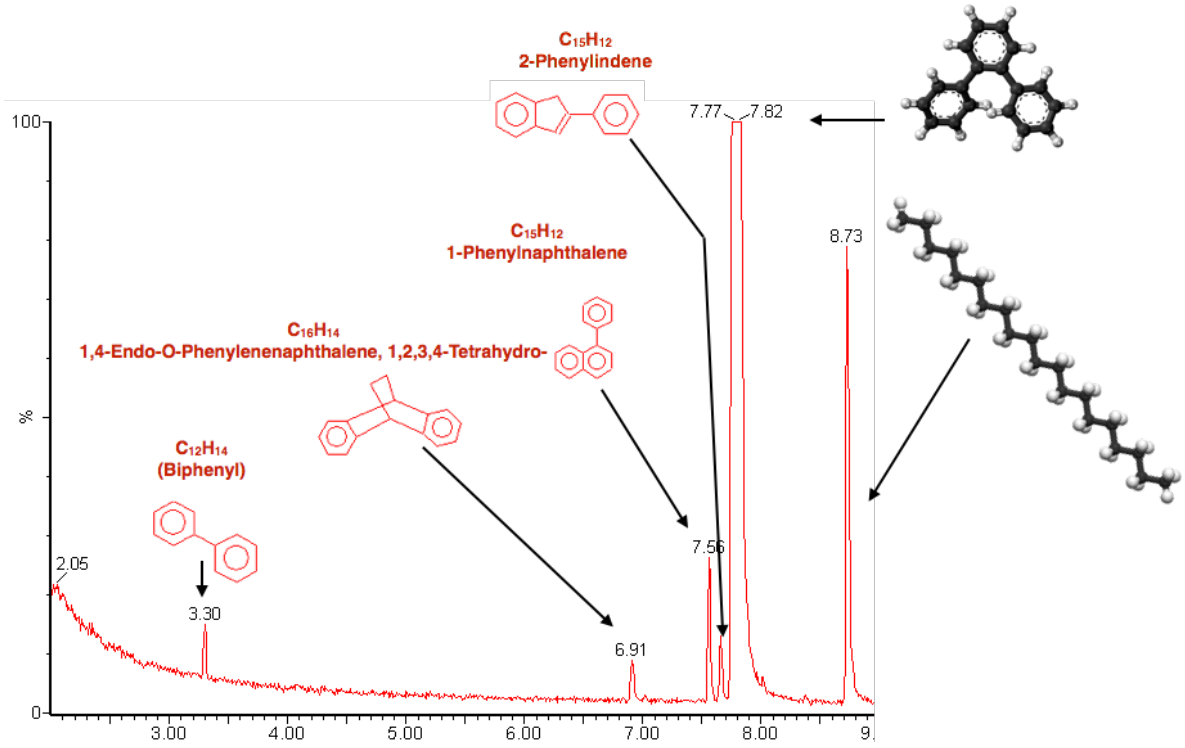

Figure 6.6 Identification of the four impurity peaks based on mass spectra. The saturated peak at 7.77 minutes is due to the main component (OTP). The peak at 8.73 minutes is due to the eicosane internal standard.

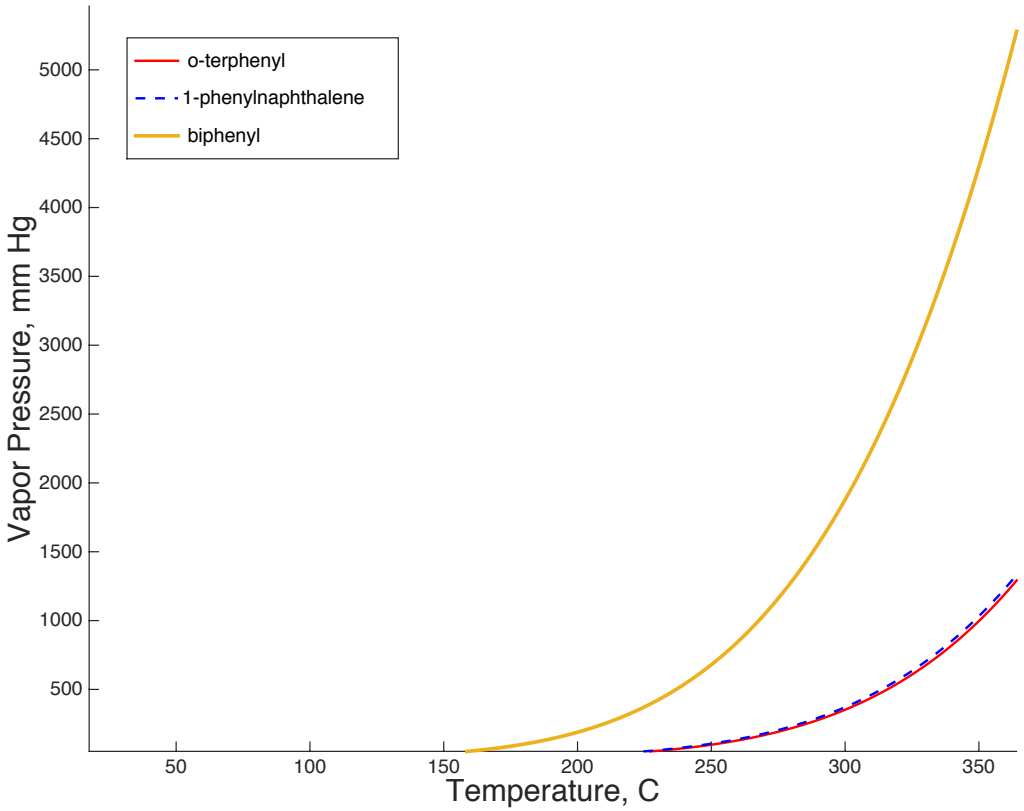

Figure 6.7 Saturated vapor pressures for *o*-terphenyl, 1-phenylnaphthalene, and biphenyl calculated using the Antoine equation and coefficients from [22].

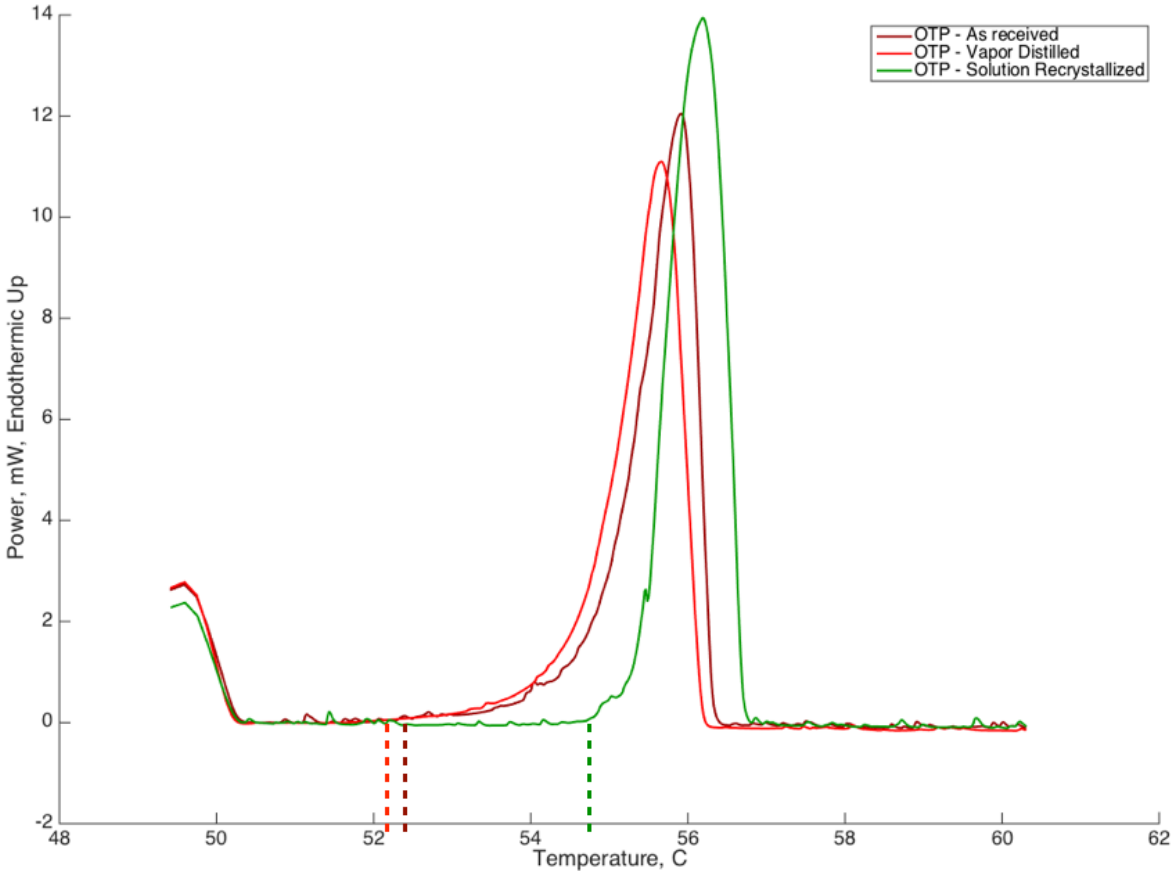

Figure 6.8 Melting endotherms for OTP in as-received, vapor distilled, and solution crystallized conditions, featuring melting temperatures of 52.4, 52.2, and 54.4° C, respectively.

CHAPTER 7. DIRECTIONAL SOLIDIFICATION OF ORTHO-TERPHENYL

7.1 Specimen Slide Preparation

A typical directional solidification experiment using the apparatus described in Ch. 5 involves two glass slides containing the material of interest, namely, a longer *observation slide* for viewing solidification and a shorter *temperature slide* featuring carefully positioned thermocouples within the same material. These slides are placed in the apparatus such that the observation slide is stationary with respect to the laboratory frame and the temperature slide is stationary with respect to the thermal field enclosure. Thus, the temperature slide travels along with the thermal field enclosure, measuring its variation over time via thermocouples at specific locations within the slide. Since heat transfer is not instantaneous, the actual temperature profile (temperature as a function of position) within the observation slide will depend on factors such as the magnitude of the imposed thermal field, the geometry of the glass slides, the thermal conductivities of the slides and specimen, and the imposed thermal field velocity. Therefore, a single thermocouple is placed in the observation slide so the temperature can be measured as a function of position between the hot and cold zones. An experiment is usually designed such that the sample thermocouple begins in alignment with the hot zone edge, so that the temperature profile is collected at the beginning of the experiment upon advancement of the thermal field. Temperature profiles collected in this manner are subsequently used to assign temperature values to features within the field of view, such as the solid-liquid interface, based on their position.

A 600 mm long observation slide and a 150 mm long temperature slide were prepared by filling 0.4mm x 4mm ID borosilicate slides, featuring previously positioned thermocouples, with

solution recrystallized OTP according to the geometries indicated in Fig 7.1. Slides were filled by applying vacuum suction to one end of the slide and inserting the other open end into OTP liquid melted in a beaker on a hot plate. After a slide was filled to a target length it was removed from the liquid and the vacuum released. The open end previously connected to vacuum was flame sealed and the other, filled, end was sealed with epoxy. Care was taken not to fill the slides excessively because the thermal expansion upon melting of OTP is quite large (>10%) resulting in frequent cracking and breaking, especially for completely filled slides and situations where material in the middle of the slide was melted and the surrounding crystal provided no room for expansion.

7.2 Temperature Profiles

The hot and cold bath temperatures were set to 85°C and -5°C, corresponding to temperatures within the hot and cold zone of about 75°C and 5°C, respectively. The observation and temperature slides were inserted into the apparatus and secured with aluminum-backed foil tape such that the cold and hot thermocouple pairs spanned the inner cold and hot zone edges, respectively, so that temperatures just within and just outside each zone could be monitored over time (see Fig. 7.1 and Fig. 5.3). [1] The temperature profile (temperature as a function of position) was measured between the hot and cold zones by monitoring the stationary thermocouple in the observation slide as the thermal field passed over it at a prescribed velocity. The measurements began with the specimen thermocouple aligned with the left edge of the hot zone and ended with the specimen thermocouple measuring a temperature about 5 mm to the left of the cold zone edge (essentially aligned with the leftmost thermocouple in the temperature slide). The velocity-dependent temperature profiles are shown in Fig. 7.2. Each profile was fit to 6-parameter polynomial so that subsequent measurements of the interface position could be used to compute corresponding interface temperatures for each velocity.

[1] The rightmost thermocouple stopped functioning a few days after the temperature slide was made, so no temperature measurements within the hot zone were recorded by this thermocouple, except for the free growth experiments described in Ch.7.4.

7.3 Directional Solidification of OTP

The relationship between crystal growth velocity and interface temperature (undercooling) for OTP was investigated by measuring the temperature at which crystals grew in a thermal gradient under steady state conditions for several velocities. Experiments were started by establishing an equilibrated interface within a thermal field ($\approx 3^{\circ}$C). After a steady and nominally flat solid-liquid interface was established, the thermal field was advanced at a constant velocity and the interface was tracked through independent displacements of the camera assembly (see Fig. 5.2). As described in 7.2, the single thermocouple in the observation slide begins in alignment with the hot zone edge. Thus, the thermal profile is measured at the beginning of each experiment and is later used to compute the interface temperature based on its position in the field of view. The influence of the observation slide thermocouple on the ensuing solidification is assumed to be negligible because (i) the interface starts only a few millimeters behind it in the thermal field and the wires are routed back through the solid (see Fig. 7.1 and Fig. 7.7) and (ii) the steady state measurements are taken much later in the experiments, at least several minutes after the interface has passed the thermocouple. Fig. 7.3 includes the constant velocity directional solidification measurements in addition to isothermal measurements reported in the literature.

Fig. 7.4 features an image of the equilibrated interface ($t = 0$ seconds) and two images of the interface growing at steady state for each of the prescribed velocities. The interface temperatures that are listed correspond to those in Fig. 7.3, and were calculated from the average interface position within four different images of steady state growth that were taken at least a few minutes apart. For the velocities investigated, the interface generally grew as distinct faceted crystals that formed a nearly planar interface with the liquid. Low velocities were associated with a few (3-5) wide crystals ranging rom 0.5 - 1 mm in width, that sometimes featured notable space / porosity in the form of channels between adjacent crystals, parallel to the growth direction. Over the course of an experiment, new faceted crystals emerged by nucleating (i) in the region between adjacent crystals, on the surfaces parallel to the growth

direction, (ii) as a consequence of crystal fracturing due to thermal stresses [2], and (iii) by the splitting of a crystal. In some cases, bubbles within the liquid were large enough to significantly disrupt a crystal, resulting in a splitting of the crystal (see Fig. 7.5 or its extinction due to the unhindered growth of surrounding crystals. As a result, the specific crystals comprising the leading edge of the interface changed over time, as new crystals emerged and others were overgrown. Nonetheless, the nominal interface position and appearance (number of crystals, crystal spacing, etc.) did not change significantly over time for a given velocity.

As shown in Fig. 7.3, the crystal growth rate - undercooling behavior of OTP followed a similar trend as previous reports, however, the results from the present work are shifted down in temperature by 5-10°C. As the velocity increased the interface adopted a more planar configuration comprised of narrower crystals, and the incorporation of bubbles, presumably dissolved air, changed. At low velocities, bubbles occasionally nucleated on the face [3] of a growing crystal and were subsequently entrapped in the advancing solid as a individual porosity sites. There was an even greater tendency for gas to continuously partition and coalesce on the face crystals and in the space between adjacent crystals. In some cases, extensive *smearing* of a bubble essentially formed a macroscopic crack. Although the identity of the gas was not investigated, it is assumed to be air and not a decomposition product or OTP vapor. It is worth noting that similar bubble formation and behavior has been reported for OTP that was extensively zone refined [10] and also for salol [98, 97].

Although a velocity of 60 microns per second was attempted twice, no steady state faceted growth was observed. Instead, the interface receded and only a few crystals grew fast enough to stay within field of view. The sharp corners of these crystals eventually rounded and over time they coarsened prior to slowing to the point of being covered by the cold zone, as shown in Fig. 7.6. Fig. 7.11 shows a similar progression for a different 60 micron per second experiment, where the velocity was stopped just before the receding interface was completely covered by the cold zone. The interface was then allowed to grow freely, during which it transitioned to a fibrous morphology around 1,400 seconds, during which thin whiskers and fibers, often

[2] As noted in [97].

[3] Points along the smooth interface between the tip and root of a growing faceted crystal.

with bubbles attached to their tips, grew individually and chaotically resulting in a very fine scale polycrystalline mass with considerable porosity (see Fit. 7.11 and Fig. 7.12). The fibrous growth lasted about 700 seconds, after which the growth transitioned to a few sites of radially growing crystallites. As these spherulites grew, less favorably oriented crystals (those not parallel with the long axis of the slide) were overgrown or otherwise terminated, establishing a faceted interface comprised of just several grains as before.

7.4 Free Growth Under The Constraint of a Thermal Gradient

The temperature dependence of crystal growth velocity for OTP was also investigated by allowing crystals to grow under the constraint of a thermal gradient ($\approx 3^\circ$ C/mm), but without an imposed velocity as before. These experiments started with an equilibrated interface near the hot zone edge and measured its position as a function of time after the thermal field was rapidly advanced (1 mm/s) such that cold zone was brought into close proximity with the interface. The initial, equilibrated, interface was also aligned with the thermocouple in the observation slide so the cooling rate of the interface could be measured. This also provided an estimate of the time required for the specimen to re-equilibrate and conform to the newly positioned thermal field. As shown in in Fig. 7.9, the transient lasted about three minutes. Once the temperature re-equilibrated, the interface position was tracked using independent displacements of the camera assembly. From those position measurements, velocities and temperatures were computed using a previously measured temperature profile collected at 1 micron per second [4], shown in Fig. 7.8. A schematic of this "free growth" process is shown in Fig. 7.7, and the results are shown in Fig. 7.10. Although overall trend agrees well with previous reports, the free growth velocities are shifted down in temperature by about 5°C compared to the previously reported isothermal studies. The morphology of the interface during free growth followed a progression similar to that described in the previous section and in Fig. 7.11, with the exception that it did not form and grow smooth crystals that receded prior to the transformation to fibrous growth.

[4] As shown in Fig. 7.2, the temperature profiles measured at 1 and 5 micron per second are nearly identical. The 1 micron per second velocity is slow enough that the *time variation* of the thermal field becomes significant, as indicated by the higher noise associated with that profile. Therefore, it should be reasonable to associate the *stationary* thermal field with a temperature profile measured at such a low velocity.

Instead, the faceted interface grew rapidly over a short distance (about 20 micron per second for 0.45 mm) before changing to fibrous growth. After about 8 minutes of fibrous growth over about 8 mm, a smooth interface composed of radially growing crystals emerged until a set of preferentially oriented faceted crystals dominated the interface. These interface morphologies are distinguished from one another in Fig. 7.10, which features plots of the interface velocity as a function of undercooling for two different free cooling experiments.

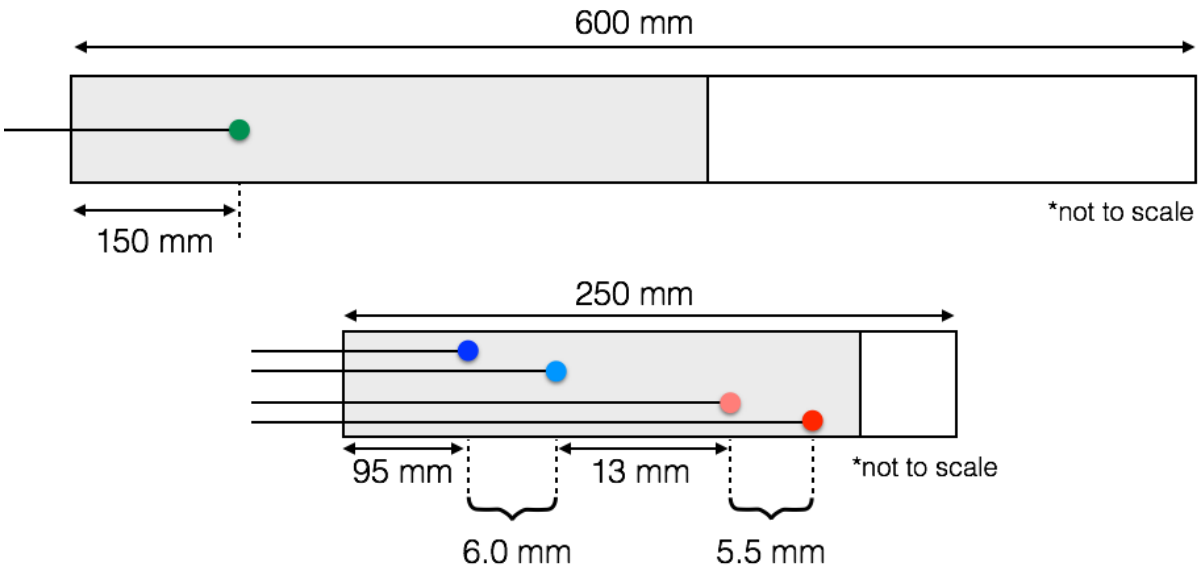

Figure 7.1 Nominal specimen slide geometries and thermocouple locations. Slides are rectangular (0.4mm x 4.0mm ID) and made of borosilicate glass. Top: observation slide. Bottom: temperature slide. Note the cold (left pair) and hot (right pair) thermocouple pairs in the temperature slide.

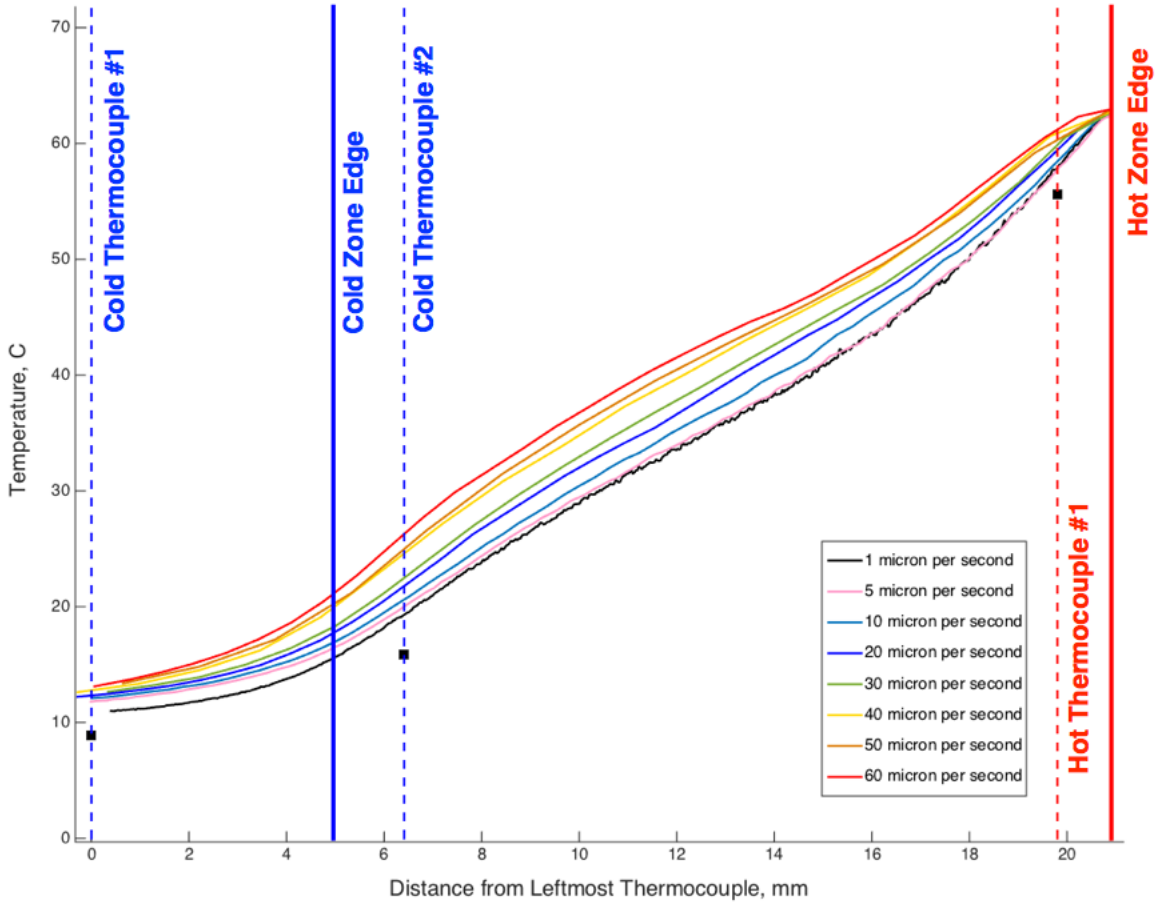

Figure 7.2 Velocity-dependent temperature profiles measured as described in the text. For higher velocities, a given position between the temperature zones is associated with a higher temperature due to the decreased time available for the specimen to re-equilibrate as the thermal field passes. Black squares indicate the thermocouple measurements within the temperature slide at their respective positions, averaged over time for all of the listed experiments. [2015-LTDS-79, -83, -84, -85, -86, -87, -88, -89, and -90]

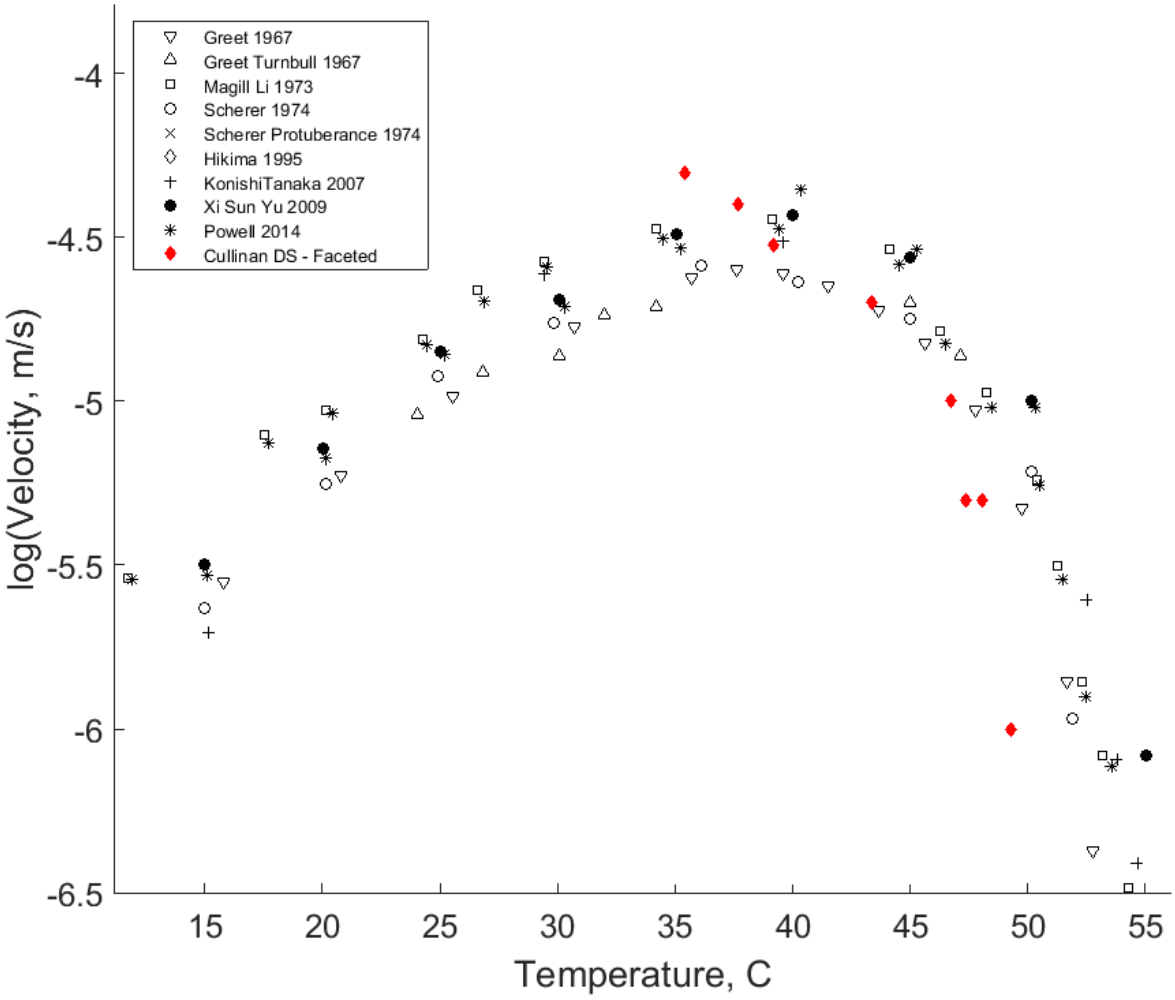

Figure 7.3 Velocity-undercooling measurements for OTP solidified under directional solidification conditions (red, present study) and isothermal conditions (black, as reported in the listed studies). [2015-LTDS-84, -85, -86, -87, -88, -89]

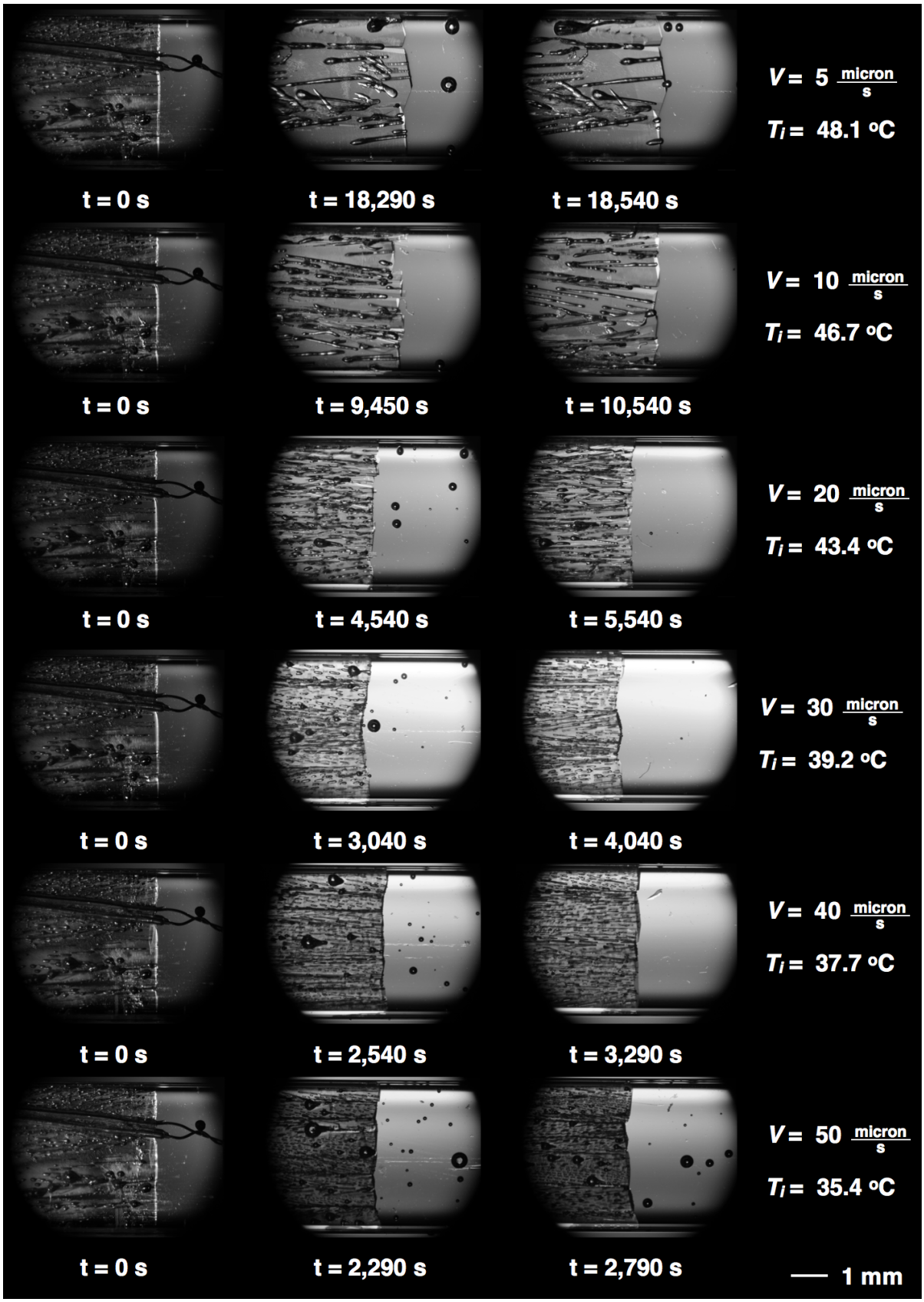

Figure 7.4 Morphology evolutions for velocities that established steady state growth. [2015-LTDS-84, -85, -86, -87, -88, and -89].

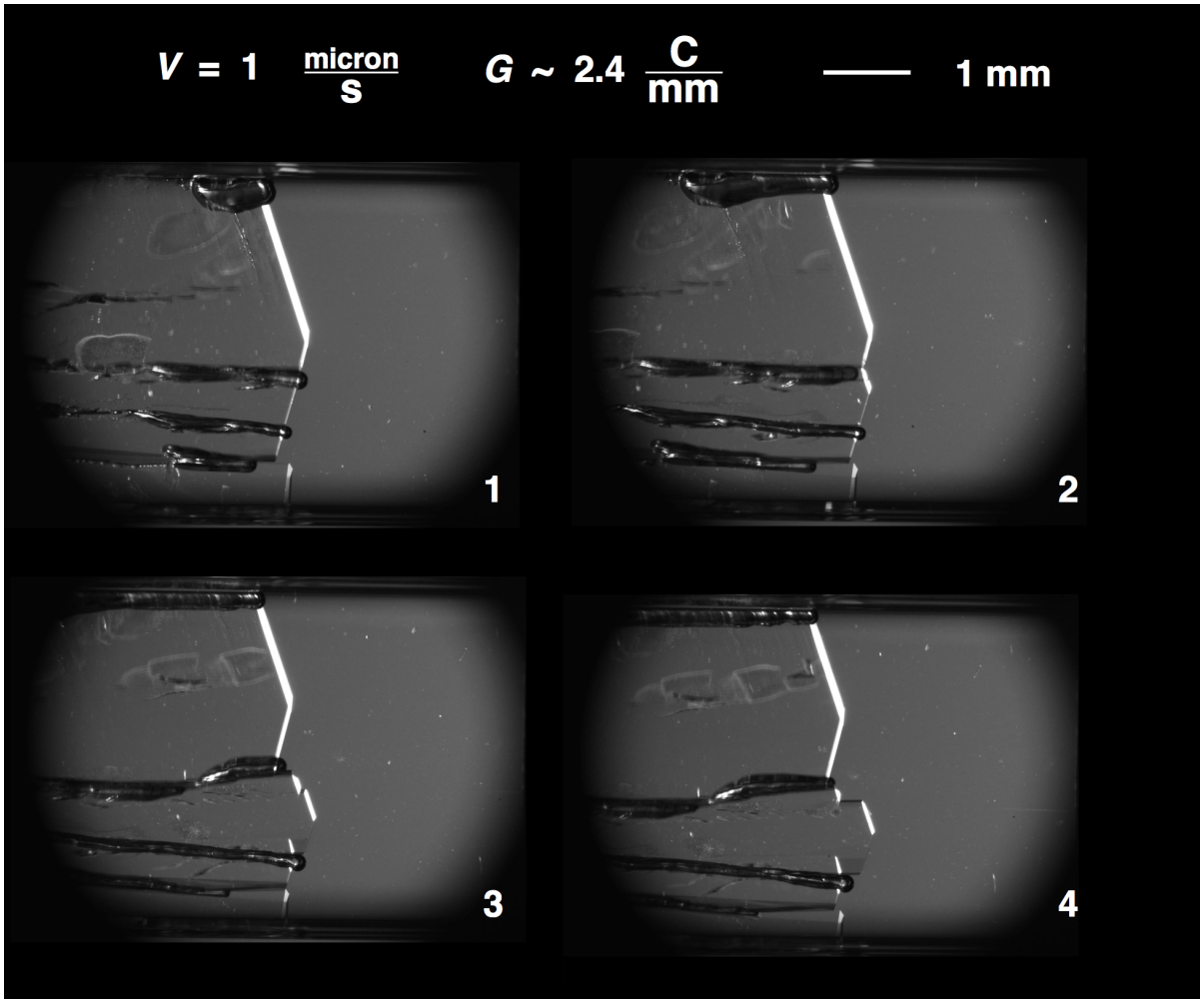

Figure 7.5 A progression of images showing splitting of a large faceted crystal due to the continuous incorporation of gas that acts to slow the top portion of the facet. As a result, the facet tip shifts upwards and the crystal splits. Such disruptions to growth and accommodations by the interface are frequent during growth at slow growth ($<$ 10 micron per second). At higher velocities, the crystals comprising interface are less dynamic, since gas tends to be incorporated in discrete pockets rather than continuous channels. Approximately 15 minutes separates each of the frames. [2015-LTDS-36]

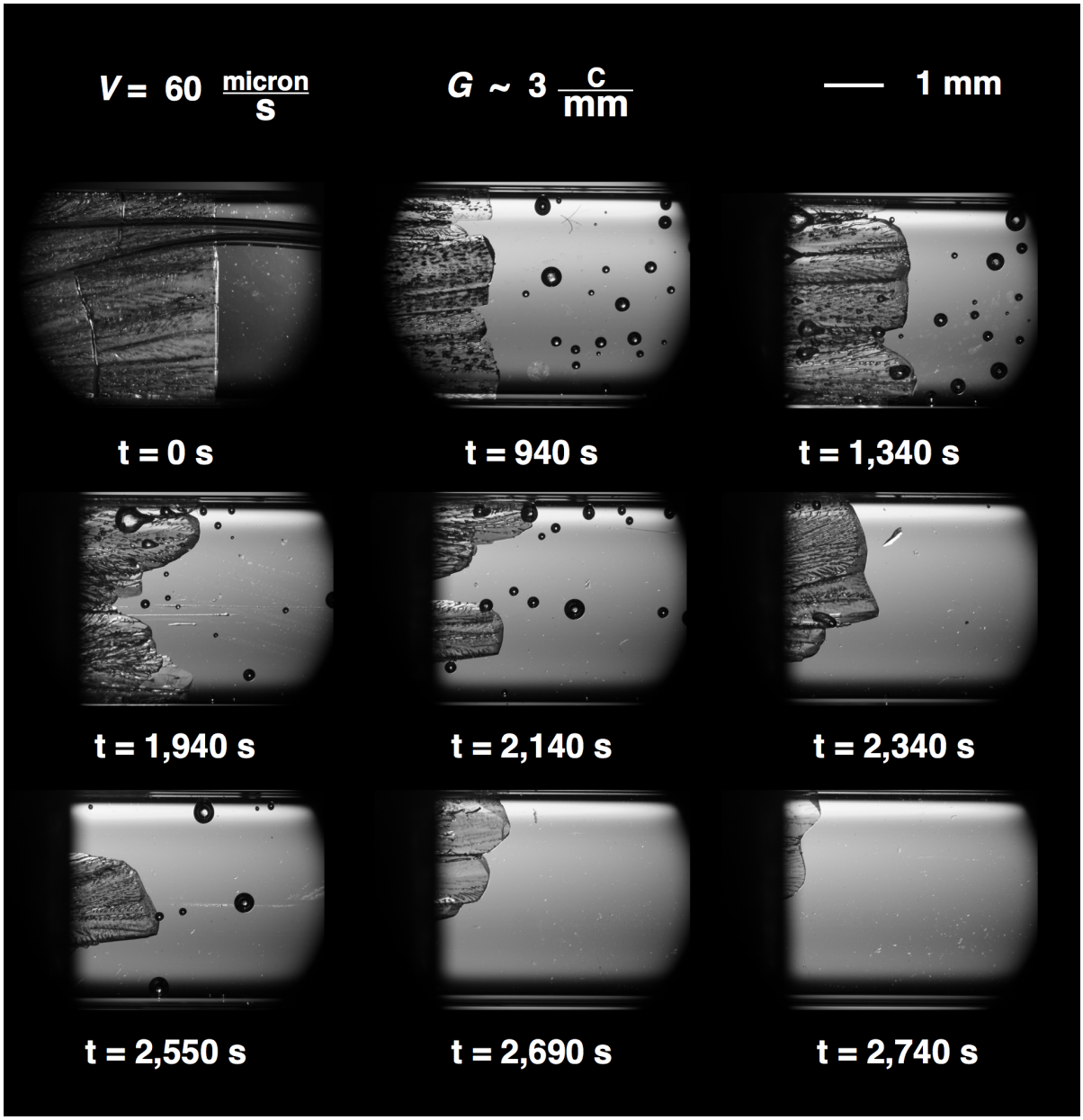

Figure 7.6 Morphology evolution for 60 micron per second growth. The interface initially grows as a faceted front, but transitions to a smooth interface before receding from the field of view, unable to grow at the imposed velocity. [2015-LTDS-91]

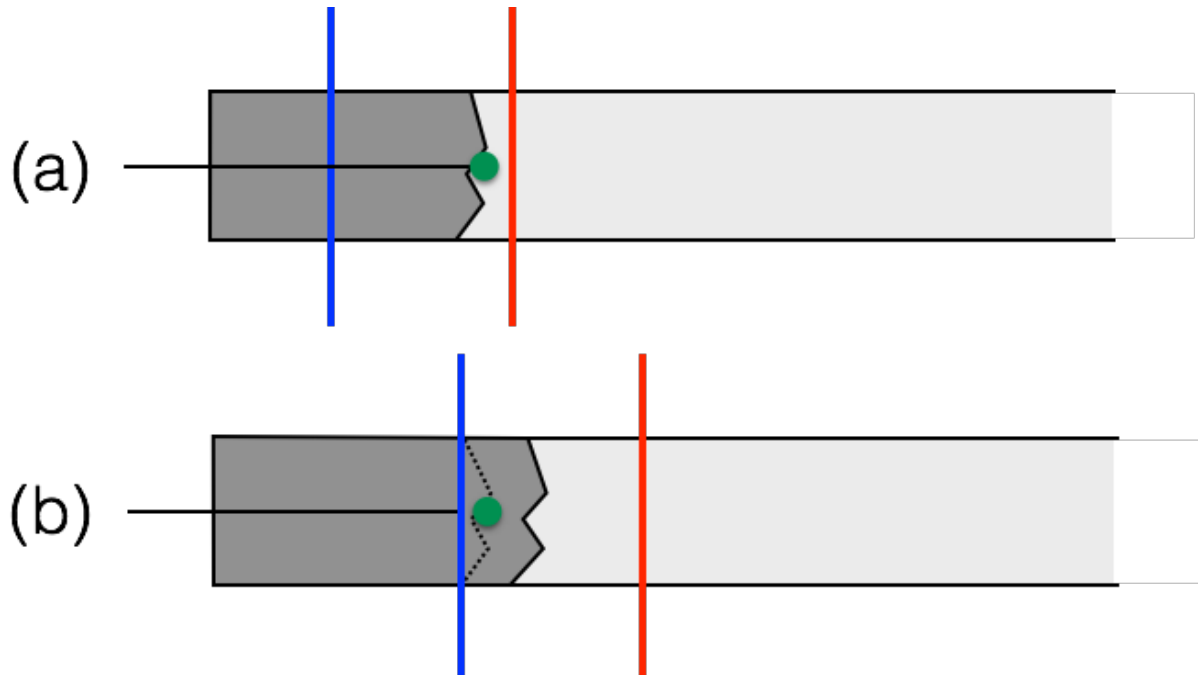

Figure 7.7 A schematic of a free growth experiment utilizing a rapid advancement of the thermal field. Red and blue lines refer to the hot and cold zone edges, respectively. (a) The initial equilibrated solid-liquid interface aligned with the sample thermocouple. (b) After the rapid advancement of the thermal field, the interface grows. The temperature profile within the specimen re-equilibrates based on the newly positioned thermal field after a few minutes, as shown in Fig. 7.9. Velocity and temperature measurements of the interface are made once the temperature reading of the sample thermocouple has re-equilibrated. Temperatures

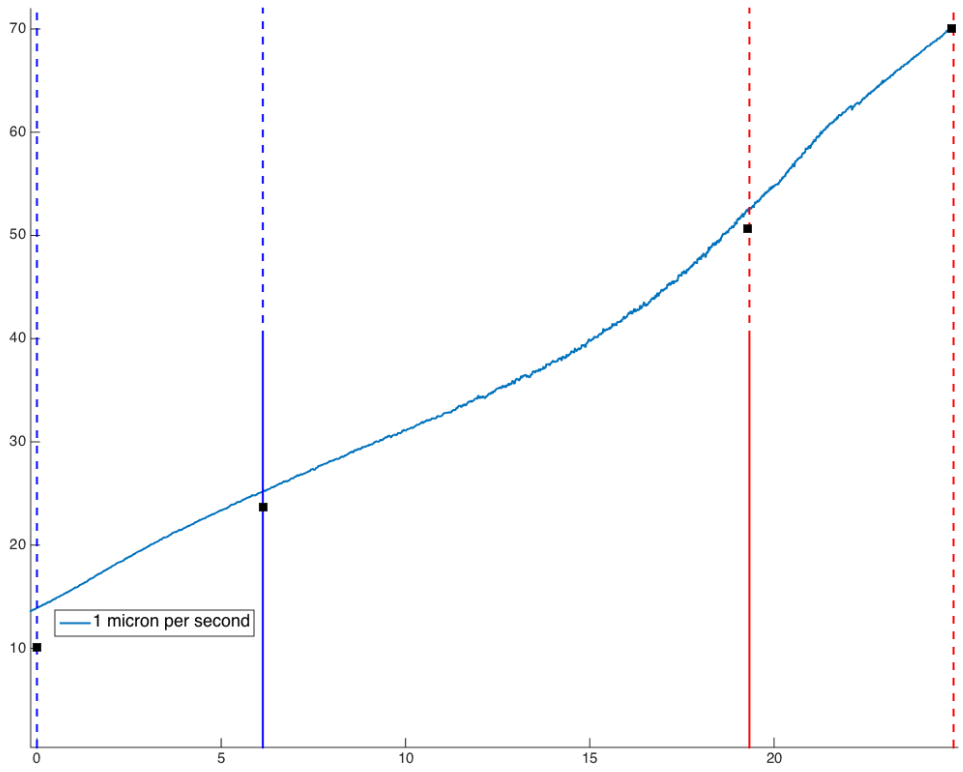

Figure 7.8 The low velocity profile used to compute temperatures based on position measurements during free growth experiments. The nominal temperature gradient associated with this profile is 1.8°C/mm. Black squares indicate the average thermocouple measurements within the temperature slide at their respective positions. [LTDS Notebook 2, Page 121]

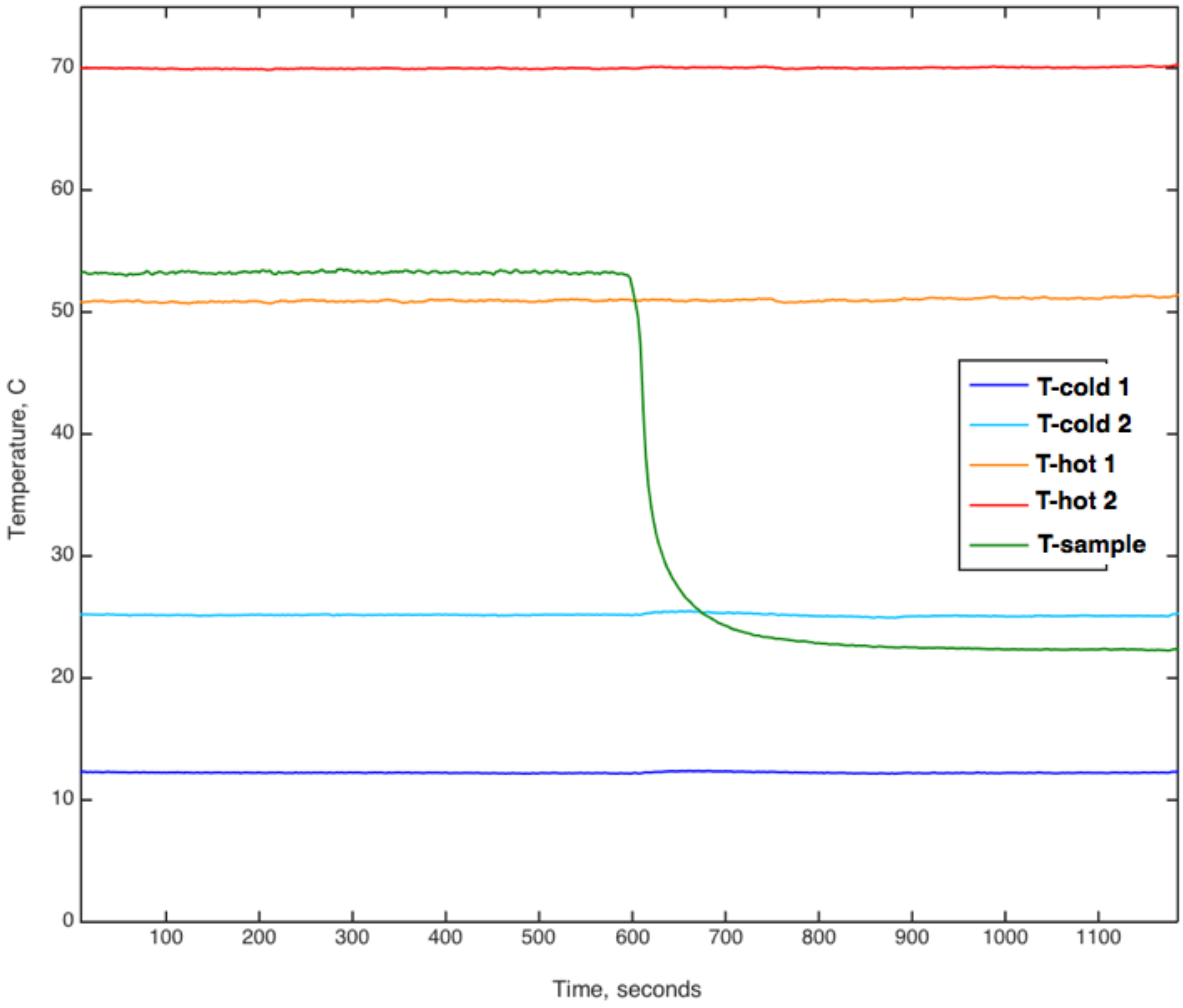

Figure 7.9 Temperatures measured in the profile slide (red, orange, light and dark blue) and in the specimen slide (green) during the free growth experiments. The rapid advancement of the thermal field (1 mm/s) resulted in a transient period where the temperature profile in the specimen adjusts to colder temperatures, as indicated by the sharp decrease in temperature just around 600 sec. The temperature transient lasts about three minutes, and all of the interface velocity and temperature measurements are taken after this period. [2015-LTDS-77]

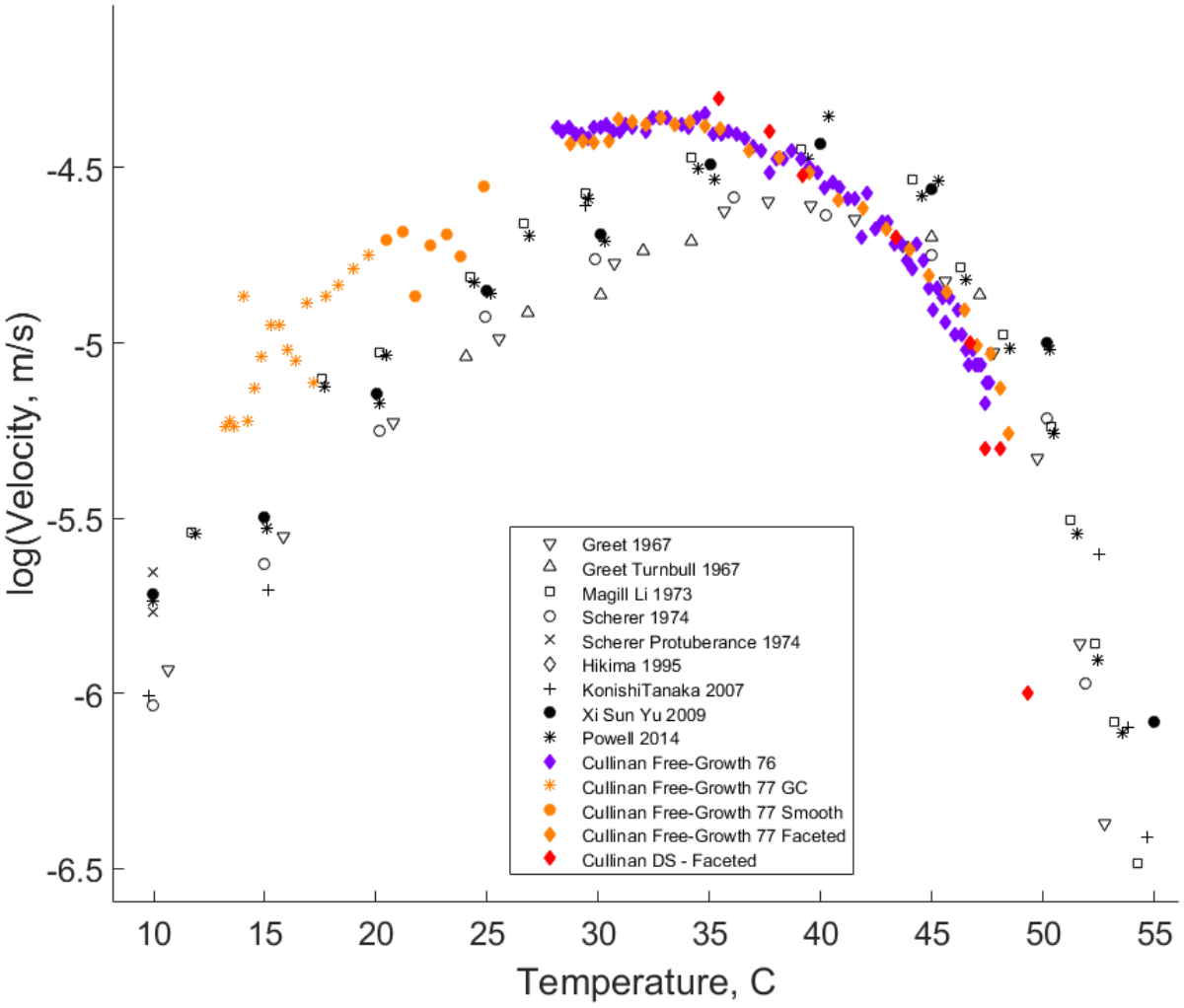

Figure 7.10 Measurements from two free growth experiments (purple & orange, 2015-LTDS-76 & -77) superimposed on previously reported isothermal measurements (black) of crystal growth velocity as a function of temperature for OTP. For the free growth data, diamonds, circles, and asterisks indicate faceted, smooth / rounded, and GC-fibrous morphologies, respectfully.

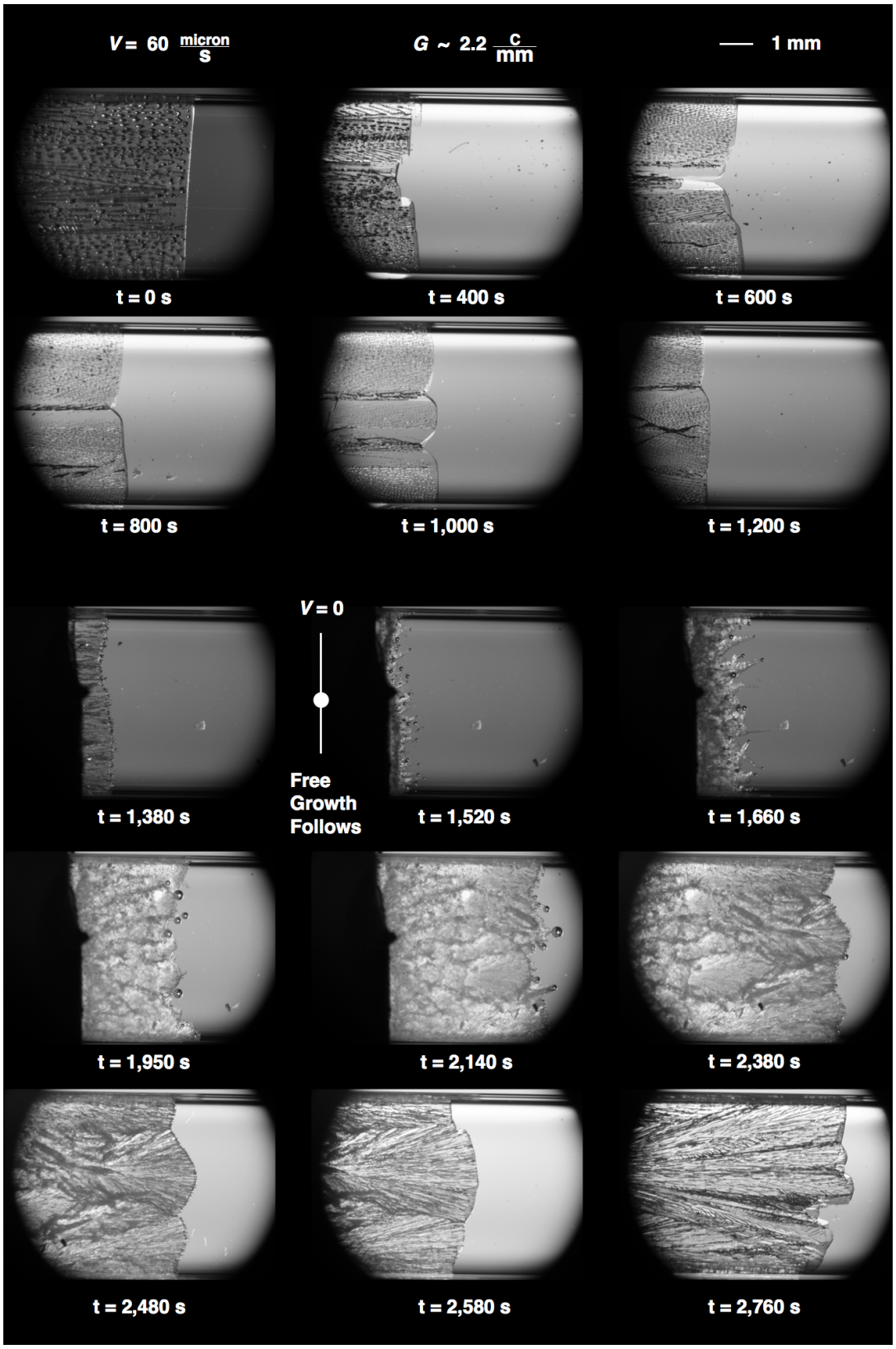

Figure 7.11 Morphology evolution for 60 micron per second growth, followed by free growth. [2015-LTDS-58]

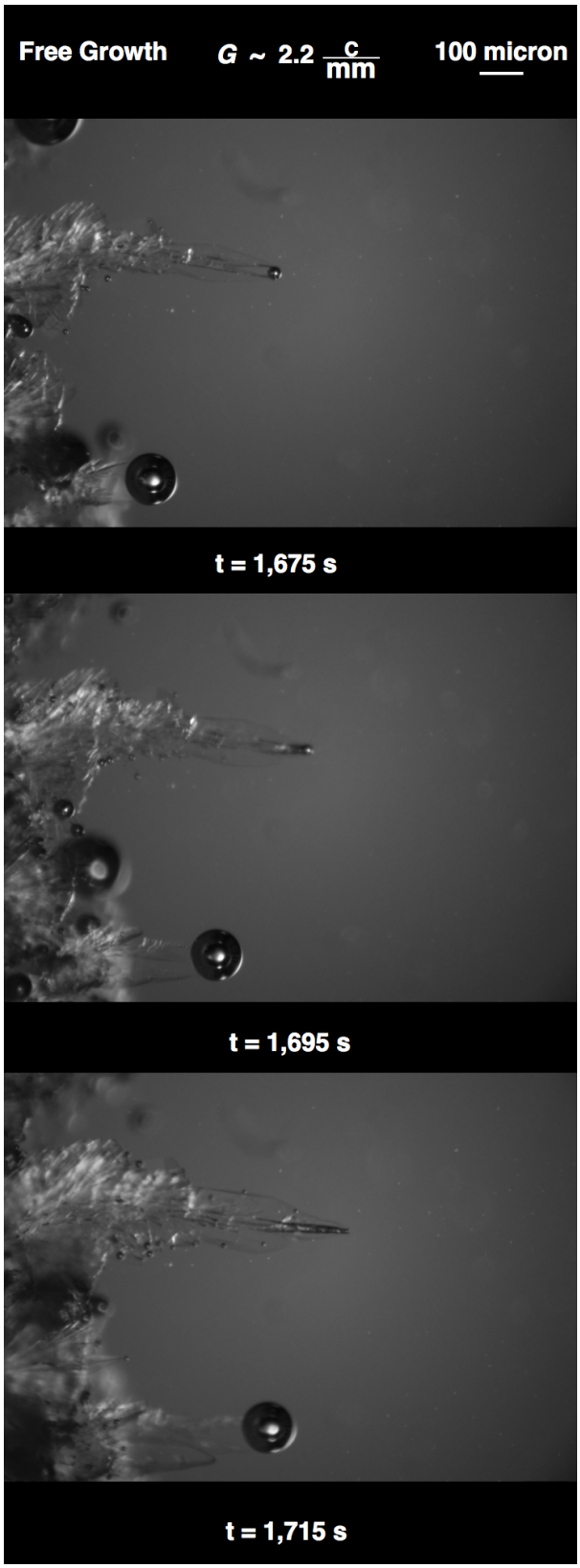

Figure 7.12 A magnified view of the fibrous growth during free growth of OTP. Times correspond to those in Fig. 7.11. [2015-LTDS-58]

CHAPTER 8. SUMMARY

The work presented in this thesis falls under two broad themes: isothermal crystallization of the metallic glass $Cu_{50}Zr_{50}$ and directional solidification of the glass-forming organic material *o*-terphenyl. The crystallization of a glassy $Cu_{50}Zr_{50}$ precursor via a structural evolution involving metastable phase formation and the anomalous crystallization morphology of deeply undercooled liquid *o*-terphenyl are both examples of transformations that occur far from equilibrium. Although there is great technological interest in metastable materials (amorphous and crystalline), prediction and control of the phases and structures that are evolved along such far-from-equilibrium pathways requires an understanding of the mechanisms and kinetics that govern the transformation dynamics.

8.1 Devitrification of $Cu_{50}Zr_{50}$

Although the devitrification of melt-quenched $Cu_{50}Zr_{50}$ has been studied extensively, the reported phase evolutions vary considerably, and many of the studies utilized poor characterization methods and/or featured inadequate reporting. Thus, a clear description of the prevailing mechanisms and related kinetics that reconciled various observations of phase evolution with system thermodynamics was lacking in the literature. Following a recent publication by Kalay et al. [6], the present work aimed to unravel the rapid initial phase evolution during the crystallization of melt-spun $Cu_{50}Zr_{50}$ through the use of isothermal annealing at temperatures near but below the onset of crystallization. Studying the transformation in this slow response regime allowed sufficient time for *in-situ* high-energy X-ray diffraction measurements and the preparation of partially annealed samples for TEM microstructural analysis.

The isothermal results indicate that devitrification of melt-spun $Cu_{50}Zr_{50}$ occurs via three stages: (i) $Cu_{10}Zr_7$ crystallites nucleate and grow, leaving a Zr enriched zone in the glass surrounding the growing particles; (ii) when the Cu:Zr atom ratio within the interface surrounding the $Cu_{10}Zr_7$ crystallites approaches 1:2, $CuZr_2$ nucleates and grows until it consumes the Zr-rich region of glass; (iii) the CuZr phase nucleates epitaxially on the $CuZr_2$ phase, assisted by the reduced nucleation barrier associated with the crystallographic similarity of the phases. Growth of the CuZr phase continues until the crystallites are completely impinged and devitrification is complete. We emphasize, once again, that the phase fractions measured after isothermal annealing are very consistent with the early phase fractions measured for specimens that were devitrified via a constant heating rate, as shown in Fig. A.12. We therefore assert that the devitrification mechanism observed during the slow-response isothermal annealing is similar to, if not the same as, the early stage devitrification mechanism during constant heating. These results provide the most systematic and consistent survey of the devitrification response to date and highlight the need for multi-method and *in-situ* characterization to adequately describe such transformations. This work also included an analysis of the isothermal devitrification kinetics using new procedure for directly fitting thermal analysis data to the commonly used JMAK expression (see Eqn. A.1). The values of JMAK parameters, k and n, computed via this direct method are shown to (i) be less sensitive to the subjective process of data truncation and (ii) require little to no data processing prior to fitting, unlike the methods commonly employed throughout the literature.

8.2 Purification and Directional Solidification of *o*-Terphenyl

Two different methods were attempted to purify *o*-terphenyl beyond the as-received condition, namely, vapor distillation and crystallization from solution. Through gas-chromatography & mass spectroscopy (GC-MS) and differential scanning calorimetry (DSC) measurements, it was concluded that only the *o*-terphenyl that was slowly crystallized from methyl alcohol featured an improvement in purity. This is likely a consequence of the impurities featuring vapor pressures that were similar to and greater than *o*-terphenyl (as shown in Fig. 6.7) rendering vapor distillation ineffective.

A directional solidification apparatus was constructed that was capable of studying crystallization of *o*-terphenyl. In particular, the design of the apparatus featured (i) a large separation of the hot and cold zones, (ii) optics that could be moved independent of the thermal field, (iii) the ability to monitor solidification over long-distances (up to about 400mm). These features allowed crystallization to be tracked over the large range of interface undercoolings exhibited by this system. The vast majority of solidification studies for *o*-terphenyl measured the velocity of crystals as they advanced in a liquid with a known, yet nominal, temperature. The present work features the first systematic study of crystallization of *o*-terphenyl using the well established method of directional solidification [1], during which the temperature of the solid-liquid interface is measured as it grows within a thermal gradient for two scenarios: (i) a constant relative velocity between the thermal gradient and sample, and (ii) free growth within a thermal gradient. Fig. 7.10 indicates that the crystallization rate - undercooling relationship for these scenarios is the same, with the exception that the system can be driven to adopt higher growth velocities compared to free and isothermal growth for temperatures between at least 34 and 38°C. Fig. 7.10 also indicates that the velocity - undercooling relations measured via directional solidification are shifted down in temperature by 5-10°C with respect to previously reported isothermal measurements.

The results presented in this thesis indicate that directional solidification (DS) of OTP is feasible and produces morphologies that are similar to those reported for isothermal conditions. The apparent shift of velocity-undercooling DS measurements to lower temperatures implies that the solidification response of OTP depends on the thermal constraints to which it is subjected. The origin of this discrepancy is complicated by the fact that no one has reported velocity-undercooling measurements under isothermal conditions (employing careful measurement of the interface temperatures) *and* under thermal gradient conditions *for the same batch of OTP*. Comparison between such data sets would minimize uncertainties that arise when comparing results from different studies, especially the influence of varying purity levels which are rarely quantified.

[1] Directional solidification of OTP was reported by Scherer et. al., who used the technique in the form of zone refinement [10], and by Shangguan & Hunt who reported a series of micrographs showing faceted OTP growing at 3.3 micron per second within a gradient of 3.5 C per mm [99].

The fibrous form of glass-crystal (GC) growth was observed during a free growth experiment within a thermal gradient and the general appearance and characteristics of its growth were similar to those reported for isothermal conditions, with one important exception. Fibers emerged from the halted faceted interface and grew independently and chaotically, coarsening over time (see Fig. 7.12). Unlike previous reports, however, the tips of growing whiskers and fibers were frequently attached to, and seemingly led by, bubbles [2] that continuously nucleated and coalesced as solidification proceeded. The fastest growing and farthest reaching fibers were typically thin and attached to relatively small bubbles (up to about 200 micron). As bubbles merged grew they eventually became trapped as porosity in the advancing crystalline mass. It is unclear whether previous studies observed this type of bubble behavior during fibrous-GC growth because they are not mentioned and not present in published micrographs. Although the formation and migration bubbles seems to enhance the growth of individual fibers, their significance, and perhaps necessity, in regard to GC growth remains unclear.

[2] Presumably air

APPENDIX A. KINETICS AND MECHANISMS OF ISOTHERMAL DEVITRIFICATION IN AMORPHOUS $Cu_{50}Zr_{50}$

Modified from a paper published in Metallurgical and Materials Transactions A.[1]

T.E. Cullinan[2], I. Kalay [3] , Y.E. Kalay [4], M.J. Kramer [5], R.E. Napolitano [6]

Abstract

The crystallization kinetics and microstructural dynamics associated with devitrifying a melt-spun $Cu_{50}Zr_{50}$ metallic glass were investigated using isothermal treatments, *in-situ* high-energy synchrotron X-ray diffraction, conventional and high-resolution transmission electron microscopy, and differential scanning calorimetry. The analysis of isothermal transformations allows us to more clearly unravel the complex interplay between nucleation and growth of competing stable and metastable phases. The isothermal devitrification response was found to involve the $Cu_{10}Zr_7$, and $CuZr_2$, and CuZr phases, consistent with previously reported constant heating rate experiments, but here we have resolved the phase evolution and structural characteristics of the transformation, including the very early stages of crystallization. At 671 K (398°C), the isothermal transformation starts with the formation of the $Cu_{10}Zr_7$ phase, which grows in a generally equiaxed morphology. At a size of approximately 100 nm, the growth of the $Cu_{10}Zr_7$ particles is interrupted by the precipitation of a thin layer of the $CuZr_2$ phase,

[1]Reprinted with permission of Metallurgical and Materials Transaction A, 46, 600-613, 2014

[2]Graduate Student, Primary Author, Department of Materials Science and Engineering, Iowa State University

[3]Assistant Professor, Department of Materials Science and Engineering, Cankaya University, 06790, Ankara, Turkey

[4]Associate Professor, Department of Metallurgical and Materials Engineering, Middle East Technical University, Ankara 06800, Turkey

[5]Materials Sciences and Engineering, Ames Laboratory, U.S. Department of Energy, Ames, Iowa 50011, USA

[6]Major Professor, Corresponding Author, Department of Materials Science and Engineering, Iowa State University

upon which the metastable CuZr (B2) grows epitaxially. Crystallization kinetics are quantified here though *in-situ* measurements (HEXRD, DSC) and *ex-situ* microstructural analysis (TEM, HRTEM). Finally, the influence of chemical partitioning, diffusion, and crystallographic orientation on this sequence are examined.

Introduction

The rapid solidification of metallic alloys may give rise to a hierarchy of non-equilibrium effects, ranging from small departures from local chemical equilibrium to large scale trapping of solutes and crystal defects, the growth of metastable crystalline phases, and even the formation of glassy or amorphous solids. Moreover, these non-equilibrium freezing products can be further transformed during subsequent heat treatments to yield novel structures with remarkable properties. Indeed, various far-from-equilibrium transformation pathways can provide access to phases and structures that may be difficult or impossible to achieve through more conventional avenues.

In particular, amorphous metals provide transformation pathways that remain largely unexplored, and there is great interest in exploiting the novel structures and enhanced properties that may be derived from the full or partial crystallization of an amorphous metal [33, 34]. Prediction and control of the phases and structures that are evolved along such far-from-equilibrium pathways, however, require an understanding of the mechanisms and kinetics that govern the transformation dynamics.

The devitrification of Cu-Zr binary metallic glasses has been studied extensively, partly because this system features strong glass formation tendency [3] and a wide composition range within which glassy alloys can be achieved by quenching from the melt [4, 5], as shown in Fig A.1. In addition, several intermetallic compounds that reside within or near this glass-forming range may play a role in the devitrification behavior, potentially appearing as stable, metastable, or transient phases. While several studies of the kinetics and phase evolution during constant heating rate (CHR) and isothermal (ISO) devitrification of melt-quenched and mechanically alloyed $Cu_{50}Zr_{50}$ have been reported (see, for example, [35, 36, 37, 38, 39, 40, 41, 42, 43, 44, 46, 47, 48, 49, 50, 51, 52, 53, 54, 55, 56, 57, 58, 59, 60, 61, 6, 62, 63] and [45,

47], respectively), these studies generally fall short of completely describing the devitrification behavior as a result of poor data arising from the chosen experimental method (e.g. conventional XRD rather than HEXRD) or insufficient data arising from too few (or no) experimental measurements and microstructural observations. In addition to the shortcomings associated with experimental methods, additional questions arise from unclear or unreported procedures for data fitting and analysis. Given these limitations, a clear description of the prevailing mechanisms and related kinetics has yet to emerge that reconciles the various observations of phase evolution with system thermodynamics.

In Table A, we summarize the studies that reported on the phase evolution during CHR devitrification of $Cu_{50}Zr_{50}$ [7], most of which used diffraction methods to determine the phase(s) that were observed to form upon heating an amorphous specimen to a selected temperature. Although the results of the initial crystallization and subsequent phase evolution vary considerably, a few trends are noted among the reports. The first transformation upon heating amorphous $Cu_{50}Zr_{50}$ was most frequently reported as an exothermic event, beginning around 720 K, that was associated with complete crystallization [8] involving the formation of $Cu_{10}Zr_7$ and $CuZr_2$. Of the five [41, 47, 50, 58, 62] studies that shared this result in common, two [58, 62] reported a second exothermic event around 773 K and 783 K, respectively, during thermal analysis. Only one [58] of those studies reported on the phase evolution corresponding with the second exotherm, associating it with the growth (increased fraction) of $CuZr_2$. This result is consistent with the phases that are most commonly reported as being present after the second exotherm, namely, $Cu_{10}Zr_7$ and $CuZr_2$.

One of the challenges associated with investigating such transformations is that the X-ray diffraction (XRD) patterns for the relevant phases are largely overlapping and difficult to deconvolute. Also, conventional XRD is less capable of detecting nano-sized crystallites compared to high-energy X-ray diffraction (HEXRD), especially when crystalline phase fraction is small. In a recent investigation using a heating rate of 10 K/min for the devitrification of

[7] We use italics here to indicate that the notation is a shorthand description of composition and not a chemical formula.

[8] By this we mean the sample no longer features an amorphous fraction. This does not necessarily imply that the resulting crystalline phase(s) are the final products of a given phase evolution.

melt-spun $Cu_{50}Zr_{50}$, Kalay et al. [6] reported a sequence involving the initial formation of the $Cu_{10}Zr_7$, $CuZr_2$, and CuZr phases [9] followed by a gradual decomposition of the metastable CuZr into $Cu_{10}Zr_7$, and $CuZr_2$. Differing from the observations of Freed et al. [35] for this heating rate, Kalay et al. found that the initial three-phase devitrification occurred too rapidly for the transformation kinetics of the individual phase(s) to be resolved. However, by applying a quantitative modeling approach to analyze *in-situ* HEXRD patterns, it was determined that the initial devitrification resulted in relative phase fractions of 0.399, 0.223, and 0.378 (by weight) for $Cu_{10}Zr_7$, $CuZr_2$, and CuZr, respectively. Moreover, this method enabled full quantification of the phase-resolved kinetics of the slower post-crystallization decomposition reaction that began partway through the first, sharp, exotherm and ended shortly after the broad second exotherm, resulting in a fully CuZr structure.

Even for the relatively low heating rate of 10 K/min, the initial devitrification was too rapid to allow the initial phase evolution to be resolved, particularly the order in which the phase(s) precipitated from the amorphous ribbon. Thus, the present study aims to provide a more comprehensive picture of the kinetic landscape surrounding the initial devitrification response of a melt-spun $Cu_{50}Zr_{50}$ glass through isothermal annealing. This enables selection of specific treatment temperatures to effect a relatively slow transformation, permitting a more detailed measurement and analysis of the phase evolution kinetics and associated mechanisms via *in-situ* HEXRD measurements and post-annealing electron microscopy.

We begin by reviewing the relatively few studies that have utilized isothermal annealing to investigate the devitrification of $Cu_{50}Zr_{50}$, which are summarized in Table A. Using DSC, Polk et. al. [36] measured the thermal response of melt-spun $Cu_{50}Zr_{50}$ during isothermal annealing treatments conducted at 5 K intervals from 690 to 715 K, although they only reported the DSC trace for 700 K. Unfortunately, no phase evolution or kinetic analysis was reported.

Using differential isothermal calorimetry (DIC), Louzguine-Luzgin et al. [54] annealed melt-spun ribbons of $Cu_{50}Zr_{50}$ at 693, 698, and 710 K. XRD of ribbon that was annealed for 20 min at 698 K (annealed slightly longer than was required for the exotherm to return to the

[9] Unless otherwise indicated, the $Cu_{10}Zr_7$, $CuZr_2$, and CuZr phases are assumed to exhibit the $oC68$, $tI6$, and $cP2$ (B2) structures, respectively.

baseline signal) indicated that a monoclinic form of CuZr precipitated from the glass during the isothermal annealing. They stated that this phase was metastable and transformed to $Cu_{10}Zr_7$ and $CuZr_2$ at higher temperatures. The DIC traces were also integrated and fit to a modified[3] form of the Johnson-Mehl-Avrami-Kolmogorov (JMAK) model, Eqn. A.1, resulting in Avrami exponent, n, values between 2.2 and 2.4. Later studies, by mostly the same authors, reaffirmed the formation of a metastable monoclinic CuZr phase during isothermal annealing and reported n values of approximately 2.5, although the temperature(s) investigated were not specified [60, 61].

In addition to the CHR experiments summarized in Table A, a study by Pauly et. al. [58] also utilized isothermal annealing to investigate the devitrification kinetics of melt-spun $Cu_{50}Zr_{50}$. The authors fit a modified [10] form of the JMAK model to isothermal annealing data acquired at 701, 703, 705, 707, and 709 K and calculated activation energies of crystallization using the fitted parameters k and n. Unfortunately, only the average value of 3.6 for n was reported.

Experimental Methods

An ingot of $Cu_{50}Zr_{50}$ nominal composition was prepared from high-purity constituents (0.9999 Cu and 0.9995 Zr, by weight) via arc melting in an argon atmosphere. The ingot was remelted and quenched on a water-cooled copper hearth three times to ensure chemical homogeneity. The ingot was melted a fourth time in a graphite crucible under 0.33 atm helium and rapidly solidified into thin ribbons, nominally 2.5 mm wide and 45 μm thick, by free-jet melt spinning onto a rotating copper wheel with a tangential velocity of 25 m/s. The as-spun ribbon specimens were verified to be amorphous through DSC, HEXRD, and TEM analysis, as reported elsewhere [6].

Devitrification response was investigated through isothermal (ISO) and quench-interrupted (QI) treatments using a Perkin Elmer Pyris 1 DSC. A 10 mg amorphous melt-spun ribbon specimen, sealed in an aluminum pan, was employed for each treatment. Sealed specimens were held at 323 K for 10 minutes to allow the instrument to stabilize prior to heating at

[10] The authors introduced a term, τ, associated with an incubation time: $f_C(t) = 1 - \exp\left[-\left(k[t-\tau]\right)^n\right]$

100 K/min from 323 K to a target temperature, after which they were held isothermally until the first measured exotherm was complete, resulting in a fully crystallized specimen. [11] The isothermal hold temperatures were 671.4, 673.4, 678.4, 683.1, 688.1, 690.2, and 693.0 K, with a maximum variation of ± 0.065 K for the duration of the treatments. Microstructural evolution during devitrification was investigated with isothermal quench-interrupted (QI) treatments that utilized a low temperature (671 K) hold terminated by a quench after partial crystallization. The isothermal hold times for these specimens were 23, 30, 37, 44, 49, and 75 min. For all ISO and QI experiments, a 20 mL/min flow of high-purity nitrogen was utilized to limit sample oxidation.

Microstructural analysis including transmission, scanning transmission, and high-resolution transmission electron microscopy (TEM, STEM, and HRTEM, respectively) using a FEI-Tecnai G2-F20. In preparation for microscopy, specimens were thinned by double-sided electrolytic jet polishing at 10 V using a solution of 33 vol.% nitric acid (in methanol) at 242 K. Quantitative micro-chemical analysis was performed using an EDAX energy dispersive X-ray spectroscopy (EDS) unit.

Results

The observed isothermal crystallization behavior is summarized by the DSC traces plotted in Fig. A.2a. Each trace exhibits a single exothermic crystallization peak, and the variation of peak location and shape indicates the temperature dependence of the overall transformation kinetics. Integration of the heat flux vs time curves yields the time-evolution of the transformed fractions for the respective hold temperatures (Fig. A.2b). The corresponding isothermal transformation (IT) contour diagram is then constructed from the full set of integrated traces, as shown in Fig. A.2c.

While we certainly cannot presume that the same set of nucleation and growth processes controls the devitrification response over the range of temperatures examined here, the general appearance of the transformation curves in Fig. A.2b does not indicate any dramatic changes

[11] We assume that such a low-temperature holding and rapid heating has a negligible effect on the subsequently measured thermal responses.

in the operative mechanisms. However, we have no reason to expect that a single mechanism or even a single phase dominates the behavior, or even that any steady nucleation or growth rates prevail. Acknowledging these issues fully, we choose for convenience to summarize the overall kinetics using the common exponential form of the Johnson-Mehl-Avrami-Kolmogorov formulation.

We emphasize that this choice is intended only to provide an empirical description of our measurements. Moreover, we make no presumption that the value of any of the empirical fitting parameters implies a correlation to any crystallization mechanism. Rather, it is our assertion that such a correlation is not prudent here, given the complexity of the far-from-equilibrium transformation which consists of multiple nucleation mechanisms that are simultaneously active, as indicated by Figs. A.6-A.7.

Accordingly, we take the fraction crystallized, f_C, as

$$f_C(t) = 1 - \exp\left[-(kt)^n\right], \tag{A.1}$$

where the model parameters, k, and n, are taken as fitting constants that are listed in Table A.1 and plotted in Fig. A.3. Once again, we resist, at this time, making any specific mechanistic interpretations related to the values of these constants, as is often done (without proper justification), and simply use the formulation as an empirical representation of the reaction kinetics. The details of the fitting procedure are presented in the appendix.

For a more detailed analysis of the isothermal response, we select a low isothermal hold temperature (671 K) for quench-interrupted treatments and examine the structure at various stages of crystallization, as indicated by the crystallized fraction, f_C. After 23 minutes at 671 K ($f_C << 0.01$), fine $Cu_{10}Zr_7$ particles (3-5 nm) are observed to be dispersed within the amorphous alloy, as shown by the HRTEM image and associated fast Fourier transform (FFT) patterns in Fig. A.4. After 30 minutes ($f_C \approx 0.01$), the structure remains as $Cu_{10}Zr_7$ growing from the amorphous bulk, as shown in Fig. A.5. After 37 minutes at 671 K ($f_C \approx 0.05$), a dispersion of very fine platelets, approximately 10-20 nm in length, are observed along with the growing $Cu_{10}Zr_7$ phase. This is shown in Fig. A.6, with an EDS map indicating the chemical partitioning that accompanies the growth of the $Cu_{10}Zr_7$ phase and the associated Zr

enrichment of the surrounding amorphous material. A related feature, observed after 37 minutes of annealing, is the appearance of a small amount of the $CuZr_2$ and CuZr phases. The nucleation scenario is revealed in Fig. A.7, where it appears that the $CuZr_2$ phase nucleates on the surface of the growing $Cu_{10}Zr_7$ particle. There, it grows to only a small thickness before it is interrupted by nucleation and general growth of the CuZr phase, with subsequent growth occurring radially outward from the original particle, resulting in a nodular three-phase morphology after 44 minutes ($f_C \approx 0.2$), as shown in Fig. A.8. The transformation proceeds in this manner until the material is fully crystallized. The prevailing nodular structure, characteristic of this $Cu_{10}Zr_7$ - $CuZr_2$ - CuZr phase sequence, is clearly revealed by the microstructures observed after 49 minutes ($f_C \approx 0.4$) and 75 minutes ($f_C > 0.99$) at 671 K, as shown in Figs. A.9 and A.10, respectively.

With the microstructural evidence clearly supporting a three-phase scenario for the devitrification response, we now revisit the *in-situ* HEXRD investigation to resolve the formation of the individual phases during crystallization. Using an independent set of isothermal HEXRD measurements obtained at 673 K, we employ a Rietveld refinement strategy, detailed elsewhere [6], to determine the time-evolution of the individual phase fractions during devitrification from the glass. While we were not able to extend the data below approximately $f_C = 0.15$, the analysis clearly shows that the $Cu_{10}Zr_7$ phase dominates the early devitrification behavior, with $CuZr_2$ and CuZr following. In addition, the individual phase fractions present when the material is fully crystallized ($f_C = 0.39$, 0.22, and 0.39 for $Cu_{10}Zr_7$, Cu_2Zr, CuZr, respectively) are consistent with the previous findings reported by Kalay et al. [6], where the subsequent phase decomposition was resolved.

Discussion

The investigation reported here employs isothermal treatment in a carefully selected slow-response regime. The approach taken here provides a view of the crystallization process with never-before achieved fidelity. The distinguishing features of this work are listed below:

- The application of *in-situ* HEXRD yields high quality data with sufficient temporal resolution so as to enable Reitveld analysis, for the fist time providing here quantitative phase-resolved time-evolution data for the crystallization process itself.

- The analysis of quench-interrupted specimens with HRTEM provides a clear view of the microstructural transformation pathway associated with the phase evolution sequence.

- The self consistent picture of the phase evolution sequence described by the combination of these techniques provides a new level of detail and clarity for our understanding of the crystallization mechanisms in $Cu_{50}Zr_{50}$, and the associated kinetics.

- The evolution sequence observed here is quantitatively consistent with our previously reported CHR analysis, suggesting that the details regarding the transformation path provided by the current work may be relevant for the CHR transitions as well, even though the rate of transformation precludes direct *in-situ* study.

Given these characteristics, the current work offers an unprecedented level of detail, where direct *in-situ* diffraction evidence, supported by detailed microstructural analysis are used together to interpret the thermal analysis measurements, for which the details of phase evolution and individual transformation steps are generally convoluted with each other and with instrument response. Our isothermal results clearly illustrate several important characteristics of the devitrification response that presumably occur during the early stages of constant heating rate devitrification, but are too rapid to resolve. Microstructural analysis of the QI specimens indicates that the $Cu_{10}Zr_7$ phase nucleates first from the glass, where its growth occurs with concomitant Cu-depletion and Zr-enrichment in the surrounding $Cu_{50}Zr_{50}$ glass. $Cu_{10}Zr_7$ particles grow to a size of 100-150 nm before the $CuZr_2$ phase nucleates on the glass/$Cu_{10}Zr_7$ interface. The observation of this limiting size suggests that it is controlled by the solute balance associated with the growth of the partitioning $Cu_{10}Zr_7$ phase and on the resulting shift

in driving force, favoring the local formation of the $CuZr_2$ phase in the Zr-enriched glass. The limited extent of growth observed for the $CuZr_2$ phase further supports this description, since the driving force for its growth would decay very rapidly over a short radial distance away from the growing $Cu_{10}Zr_7$ particle. In addition, the epitaxial relationship between the $CuZr_2$ and CuZr phases, shown in Fig. A.11, essentially eliminates the nucleation barrier and promotes rapid formation of the CuZr phase as soon as it is energetically driven, which occurs when the Zr-enriched region of glass is consumed by growth of the thin layer of $CuZr_2$.

The generally nodular appearance of the overall microstructure implies that this mechanism of $Cu_{10}Zr_7/CuZr_2$ seeding of the CuZr phase is favored over nucleation and growth of the CuZr directly from the glass. (We qualify this statement by noting that the fine plate-like phase remains unidentified but consistent with the $CuZr_2$ $C11_b$ structure.) Moreover, since the $Cu_{10}Zr_7/CuZr_2/CuZr$ sequence gives rise to the appearance of CuZr very early in the overall transformation (i.e. $f_C = 0.05$) and since CuZr does not nucleate directly from the glass, the overall kinetic response is mainly controlled by the growth kinetics of the B2 phase (which were investigated for higher temperatures in a recent molecular dynamics study [100]). Fig. A.12 indicates that the phase fractions after complete isothermal crystallization agree well with the initial phase fractions from recently reported CHR results [6]. Thus, we assert that the phase selection mechanisms are similar for both the ISO and CHR crystallization cases, and that these results identify, generally, the initial crystallization sequence for melt-spun $Cu_{50}Zr_{50}$.

A meaningful comparison of our isothermal annealing results to previous investigations relies on unreported details of those studies, such as melt-spinning parameters the mass of thermal analysis samples, the thermal history of the isothermally annealed samples [12], and all of the fitted JMAK parameters including the temperature(s) they correspond to and how they were computed. Despite these issues, we elect to include a very basic comparison here for completeness. The isothermal traces we report in Fig. A.2 feature characteristic times (onset, peak, offset) that are on the same order of magnitude as those reported by of Polk [36], Louzguine-Luzgin [54] et al., and Pauly et al. [58]. All three of these reports indicate isothermal responses that are slower than our data would suggest, if extrapolated. For the

[12] Specifically, the heating rate used to reach the annealing temperatures.

temperature we report in common with Louzguine-Luzgin et al. (693 K), for example, our exotherm has completed and returned to the baseline signal approximately four minutes before their exotherm initially deflects.

Conclusions

We present, for the first time, a complete description of the structural evolution that occurs during isothermal devitrification of melt-spun $Cu_{50}Zr_{50}$, based on *in-situ* high-energy X-Ray diffraction, *ex-situ* electron microscopy, and thermal analysis. Our HEXRD and TEM results show that the isothermal devitrification of melt-spun $Cu_{50}Zr_{50}$ occurs via three stages: (i) $Cu_{10}Zr_7$ crystallites nucleate and grow, leaving a Zr enriched zone in the glass surrounding the growing particles; [13]; (ii) when the Cu:Zr atom ratio within the interface surrounding the $Cu_{10}Zr_7$ crystallites approaches 1:2, $CuZr_2$ nucleates and grows until it consumes the Zr-rich region of glass; (iii) the CuZr phase nucleates epitaxially on the $CuZr_2$ phase, assisted by the reduced nucleation barrier associated with the crystallographic similarity of the phases. Growth of the CuZr phase continues until the crystallites are completely impinged and devitrification is complete. We emphasize, once again, that the phase fractions measured after isothermal annealing are very consistent with the early phase fractions measured for specimens that were devitrified via a constant heating rate, as shown in Fig. A.12. We therefore assert that the devitrification mechanism observed during the slow-response isothermal annealing is similar to, if not the same as, the early stage devitrification mechanism during constant heating.

Appendix - JMAK Fitting Procedure

The magnitude and overall shape of thermal analysis measurements depends on a variety of factors, some of which are related to the specimen itself (such as its geometry, mass, and thermal history) while others are related to the specific instrument and heating steps that are used. Nonetheless, isothermal reactions measured by differential calorimetry (DSC, DTA, etc.) frequently exhibit bell-shaped signals superimposed on a relatively constant baseline signal

[13] During this stage, small plate-like crystals also precipitated within the amorphous matrix. They were too small to identify and their effect on the crystallization pathway requires further investigation.

associated with maintaining the temperature of interest. A common method for determining the JMAK parameters (k and n) from constant temperature data involves computing a normalized cumulative integral over the thermal analysis event (peak) that corresponds to the isothermal transformation of interest. These methods assume that the magnitude of the measured signal is directly related to the transformation rate. A plot of the normalized cumulative integral (of a bell shaped curve) versus time is sigmoidal, equaling zero at the lower integration bound and equaling one at the upper integration bound. Such a curve can be fit to the JMAK expression, $f(t) = 1 - \exp\left[-(kt)^n\right]$, to determine the reaction rate constant, k, and Avrami exponent, n. This type of analysis assumes that the normalized cumulative integral corresponds with the time-dependent volume fraction of the system that has transformed. An alternative analysis involves plotting $\ln(-\ln(1-f))$ versus $\ln(t)$ and computing k and n from the slope and intercept of the log-linearized expression for $f(t)$: $\ln(-\ln(1-f)) = n\ln(k) + n\ln(t)$.

Although constant temperature thermal analysis measurements often seem to be ideally shaped for such analysis, they tend to exhibit features and artifacts that must be addressed in order to ensure that a fit is accurate. Perhaps the biggest challenge involves accounting for a non-constant baseline signal [14], even when an instrument background signal is subtracted. This is especially problematic when the transformation of interest occurs so rapidly that the measured signal associated with the instrument ramping to the isothermal holding temperature overlaps the signal for the transformation of interest. This is usually not an issue for slower transformations where sufficient time is available for the instrument to establish a relatively constant baseline signal prior to, and after, the transformation of interest. In either case however, proper analysis requires careful truncation, since the fitting results for the methods described above are sensitive to the choice of integration bounds, as we demonstrate in Fig. A.13c-f. This is especially true for the log-linearization method, where the logarithmic plot is linear over a smaller range as the amount of truncation increases, as shown in Fig. A.13e for the fitting of

[14] According to the JMAK expression, a valid cumulative distribution function, f should equal zero at $t = 0$, and approach one as t approaches infinity. Thus, df/dt is bell-shaped, equals zero at $t = 0$, and asymptotically approaches zero as t approaches infinity. A DSC trace is not likely to share the second and third properties exactly in common with df/dt, even if we account for the trace approaching a non-zero constant (C). However, the signal surrounding a thermal event is often fairly constant during isothermal annealing, and such a trace can be approximated fairly well by a scaled and shifted form of df/dt.

our raw 688.1 K isothermal data set. The nonlinear artifacts that arise in the logarithmic plot introduce the need to further limit the amount of data that is considered when constructing a line from which n and k are computed.

To avoid the complexities associated with data truncation, we have computed the JMAK parameters n and k from the raw isothermal DSC signals (with the exception of the 673.4 K data set, as we describe below). We begin by considering the time derivative of the JMAK expression, df/dt, which is essentially a probability density function for the cumulative distribution function $f(t)$. In order to approximate an isothermal DSC signal, $\dot{Q}$, we scale and shift $\frac{df}{dt}$ by the factors S and C, respectively. Thus,

$$\dot{Q} \approx S\left[\frac{df}{dt}\right] + C = S\left[(kn)(kt)^{(n-1)}\exp[-(kt)^n]\right] + C \tag{A.2}$$

Fitting [15] this expression to an isothermal DSC signal with a relatively constant baseline results in n and k values that i) are less sensitive to the extent of data truncation and ii) describe the DSC trace with high accuracy, as we demonstrate in Fig. A.13b for four different truncation scenarios. This method was applied to each of our raw [16] isothermal data sets, resulting in fitted parameters that are listed in Table A.1. For each fitting, the corresponding data set was truncated such that only the points surrounding the isothermal peak down to one percent of the peak height were considered.

Acknowledgements

This work was supported by the U.S. Department of Energy, Office of Basic Energy Science, Division of Materials Sciences and Engineering. The research was performed at the Ames Laboratory. Ames Laboratory is operated for the U.S. Department of Energy by Iowa State University under Contract No. DE-AC02-07CH11358.

[15] Via non-linear regression.

[16] With the exception of the 673.4 K data set, the thermal analysis data was not altered prior to data fitting. The 673.4 K data set warranted a background subtraction to remove a slight curvature that was imparted on the baseline by the instrument. This correction consisted of subtracting a signal that was measured under the same conditions as the 673.4 K ISO experiment, except in the absence of a specimen.

Synchrotron experiments were performed at the Advanced Photon Source, Argonne National Laboratory, under Grant No. DE-AC02-06CH11357.

The authors thank Will Landau (Department of Statistics, Iowa State University) for assisting with the development of the “direct” JMAK fitting procedure.

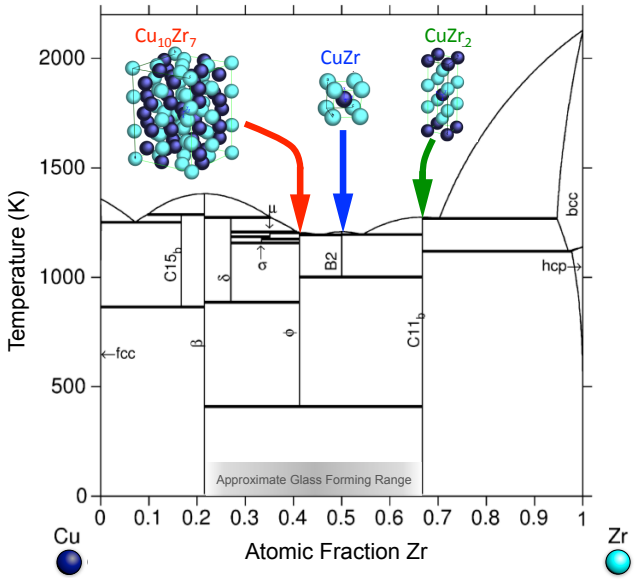

Figure A.1 The equilibrium Cu-Zr phase diagram [23]. Three intermetallic phases relevant to the current work are indicated. The shading of the composition axis indicates the approximate range over which the Cu-Zr system exhibits strong glass-forming tendency.

Table A.1 A summary of phase-resolved studies that employed constant heating rates for the devitrification of amorphous $Cu_{50}Zr_{50}$. The phase(s) that are listed as precipitating from the amorphous precursor are associated with the first observed exotherm, and the phase(s) listed as subsequent phase evolution correspond to a second exotherm, if observed.

Ref.	**Phase(s) Precipitating From Amorphous Precursor**								**Subsequent Phase Evolution**							
	Thermal Analysis				**Resulting Phase(s)**				**Thermal Analysis**				**Resulting Phase(s)**			
	Meth.	**Rate (K/min)**	T_x **(K)**	T_p **(K)**	**Meth.**	**$Cu_{10}Zr_7$**	**$CuZr_2$**	**CuZr**	**Meth.**	**Rate (K/min)**	T_x **(K)**	T_p **(K)**	**Meth.**	**$Cu_{10}Zr_7$**	**$CuZr_2$**	**CuZr**
[35]	DSC	10	715†	724	TEM ♢ XRD ♢				DSC	10	728†	731	TEM XRD			■
[36]	DSC	10 20 40 80 160	722.0 728.5 736.0 745.5 754.0	726.0 733.5 741.0 750.5 760.5	XRD			■–α								
[38]	DSC	50		774	XRD			■–**O**	DSC	50		794	SPEC			ℝ(■–**O**)
[39]	DSC	40		735†	XRD		□		DSC	40		781†	XRD	■	■	
[41]	DTA	20	716	721†	XRD	■	■									
[43]	DTXD	0.835	672		DTXD			■	DTXD	0.835			DTXD	■	■	
[44]	DSC DSC DSC	10 20 50	685†	716.2 725.4 738.9	SPEC			■ or ■–**O**								
[46]	DSC	25	703†	728	FIM	□			DSC	25	753†	788	FIM	■	■	
[47] *	DTA	20	736†	796†	XRD	■	■									
[50]	DSC	4	714†	719†	XRD	■	■									
[57]	DSC	20	738†	740†	XRD	■										
[58]	DSC	40	724	725	XRD	■	■		DSC	40		773†	HEXRD XRD	■	𝔾(■)	
[59] ♠	DSC	10	707		XRD HRTEM	■										
[6] ♣	DSC	10	703	708	HEXRD	■	■	■	DSC	10	738	749	HEXRD	■	■	
[62]	DSC	20	719†	726†	SAXS WAXS	■	■		DSC	20	760†	783†				
[63] ♦	RES	10	719.6		XRD	■	■		RES	10	997		XRD			■

Table A.2 Table 1 - Continued

Unless otherwise indicated, all of the studies pertain to the devitrification of melt-spun ribbons of $Cu_{50}Zr_{50}$.

* In the case of [47], the samples were mechanically alloyed via ball milling.

♠ In the case of [59], the samples were prepared via gas atomization. HRTEM revealed $Cu_{10}Zr_7$ nanocrystals, approximately 5 nm in size, in the as atomized powder.

♣ In the case of [6], transformation temperatures based on *in-situ* HEXRD data agreed well with onset and peak temperatures measured via DSC, as shown in Fig. A.12b.

The *in-situ* HEXRD results also indicated that a third transformation occurred between 1002 K and 1045 K and corresponded to the re-formation of CuZr (at the expense of $Cu_{10}Zr_7$ and $CuZr_2$) Once formed, CuZr phase persisted during further heating until it melted at 1233 K .

♦ [63] reported resistivity measurements taken while heating an initially amorphous specimen from 300 K to a little beyond 1100 K. Although they reported two separate transformations, the first spanned a temperature range that was commonly associated with two exotherms, one sharp starting around 720 K and one broad starting several degrees higher. The second transformation they report, corresponding to the transformation of $Cu_{10}Zr_7$ and $CuZr_2$ into CuZr (B2), is a separate transformation that is not reported in the thermal analysis results of the other references listed in the table, because those experiments did were not conducted to such high temperatures. The second transformation reported by [63] (the formation of CuZr from $Cu_{10}Zr_7$ and CuZr2) is consistent with the Cu-Zr phase diagram [23] and the HEXRD results of [6], however.

Unless otherwise indicated, the $Cu_{10}Zr_7$, $CuZr_2$, and CuZr phases are assumed to exhibit the $oC68$, $tI6$, and $cP2$ structures, respectively.

■ Phase was present after the corresponding exotherm, and the resulting structure was fully crystalline and comprised of the indicated phase(s).
□ Phase was present after the corresponding exotherm, but the specimen remained partially amorphous.
♢ The first exothermic event corresponded with partial crystallization of an unidentified metastable phase.

–**O** Orthorhombic form of the corresponding stoichiometry.
–$\boldsymbol{\alpha}$ The first exothermic event corresponded with the complete crystallization of an α-ZrCu phase, that was reported as being similar to $Cu_{10}Zr_7$ [36]. The α-ZrCu phase was found "after the DSC scan of an amorphous sample." The reference is not clear as to which scan(s) this result applies to.

$\mathbb{R}$ The authors of the corresponding study attributed the second exotherm to recrystallization of the indicated phase.
$\mathbb{G}$ The authors of the corresponding study attributed the second exotherm to growth of the indicated phase.

$\boldsymbol{T_x}$ and $\boldsymbol{T_p}$ refer to the temperatures associated with the onset and peak of an exothermic event recorded by thermal analysis, respectively.
† The listed value is an estimate made by the present authors based on data presented in the corresponding reference.

SPEC - The authors of the corresponding study speculated this finding. In the case of [44] the conclusion was based on previously published studies [65, 38].

DSC - Differential Scanning Calorimetry
DTA - Differential Thermal Analysis
DTXD - Dynamic Temperature X-ray Diffraction

XRD - X-ray Diffraction
HEXRD - High-Energy X-ray Diffraction
SAXS - Small-Angle X-ray Scattering
WAXS - Wide-Angle X-ray Scattering

TEM - Transmission Electron Microscopy
HRTEM - High-Resolution Transmission Electron Microscopy
FIM - Field Ion Microscopy

RES - Resistivity

Table A.3 A summary of phase-resolved studies that employed isothermal annealing for the devitrification of melt-spun $Cu_{50}Zr_{50}$.

Ref.	**Phase(s) Precipitating From Amorphous Precursor**											
	Thermal Analysis / JMAK Fitting							**Resulting Phase(s)**				
	Method	**Temp. (K)**	t_x **(min)**	t_p **(min)**	k	n	τ	**Method(s)**	**α-CuZr**	**CuZr-M**	**$Cu_{10}Zr_7$**	**$CuZr_2$**
[36]*	DSC	700	4.6	8.3				Not Specified	■			
[54]	DIC	693	11.1	15.1	—	2.2 - 2.4	—					
		698	7.6	10.5				XRD		■		
		710	5.0	6.1								
[58]	DSC	701	2.3	4.5	—	3.6	—	SPEC			■	■
		703	1.6	3.5							■	■
		705	1.3	2.8							■	■
		707	0.9	2.3							■	■
		709	0.8	1.9							■	■
[60, 61]	Not Specified				—	2.5	—	XRD		■		

■ Phase was present after the corresponding exotherm, and the resulting structure was fully crystalline and comprised of the indicated phase(s).

t_x and t_p refer to the annealing times associated with the onset and peak of an exothermic event measured during isothermal annealing, respectively. These values were inferred by the present authors and t_x was taken as the annealing time associated with a signal value equal to one percent of the peak time, relative to the baseline signal.

References [54, 58, 61] used a modified form of the JMAK expression that incorporated an explicit incubation time, τ: $f_C(t) = 1 - \exp\left[-\left(k[t-\tau]\right)^n\right]$

— The corresponding parameter was used for fitting, but the value(s) were not reported. t_x, as defined above, should be a reasonable estimate for τ.

* The authors of [36] mentioned that they measured the thermal response of melt-spun $Cu_{50}Zr_{50}$ during isothermal annealing treatments conducted at 5 K intervals from 690 to 715 K, although they only reported the DSC trace for 700 K. No kinetic analysis was reported.

DSC - Differential Scanning Calorimetry
DIC - Differential Isothermal Calorimetry

XRD - X-ray Diffraction

SPEC - The corresponding reference did not indicate how the phases were determined as products of the isothermal annealing treatments listed.

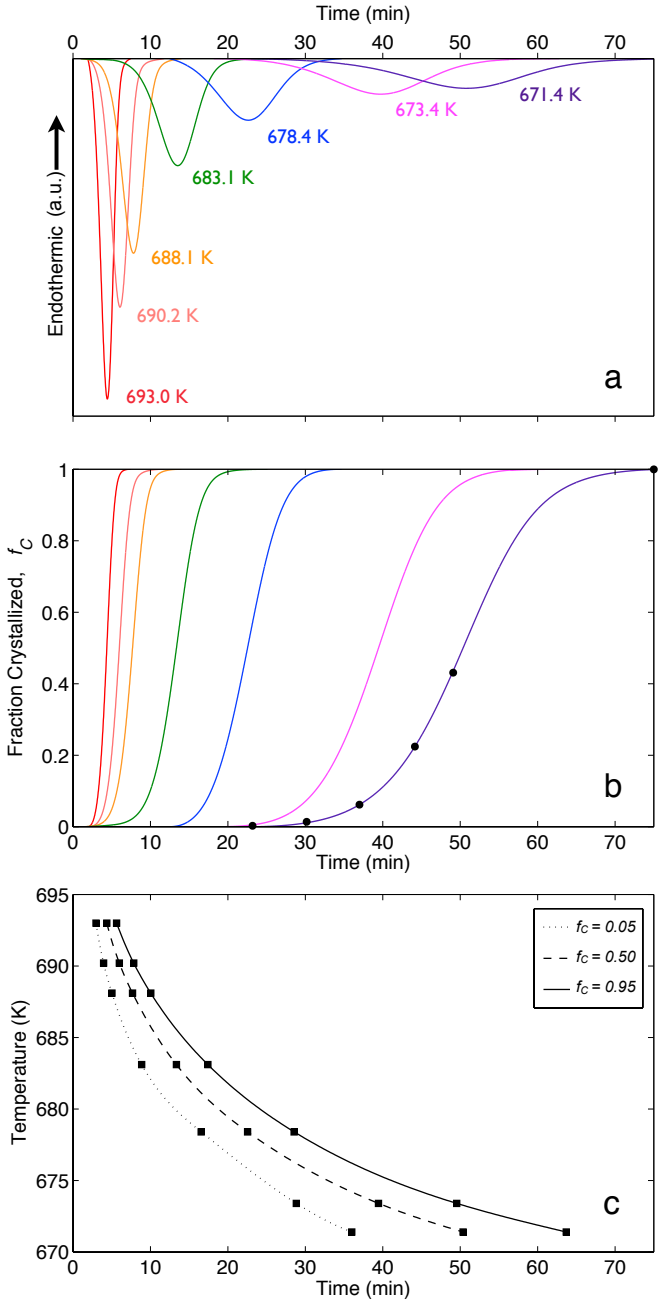

Figure A.2 Results for isothermal DSC experiments: (a) DSC traces for the indicated temperatures (shifted to a common baseline), (b) corresponding plots of fraction crystallized versus time (Note: • denotes the times selected for the QI experiments), and (c) the IT diagram for the overall isothermal crystallization event. Note: ■ denotes calculated times based on i) the isothermal temperatures investigated and ii) the fractions of interest.

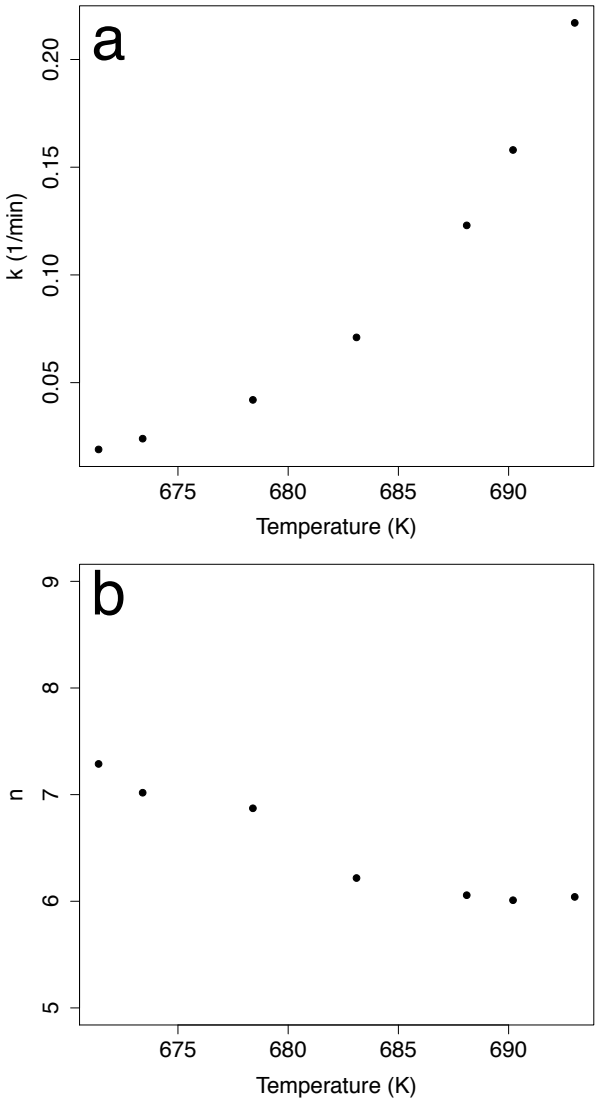

Figure A.3 Plots showing the temperature dependence of the fitted JMAK model parameters k (a) and n (b). The parameters were fit according to the method described in the appendix.

Table A.1 Fitted JMAK Parameters, computed as described in the appendix.

Hold. Temp. (K)	k (1/min)	n	S mW · min	C mW
671.4	0.019	7.288	6.214	11.403
673.4	0.024	7.018	6.180	-0.002
678.4	0.042	6.872	6.238	12.801
683.1	0.071	6.218	7.104	18.356
688.1	0.123	6.057	7.677	21.689
690.2	0.158	6.010	7.701	21.446
693.0	0.217	6.041	7.762	34.344

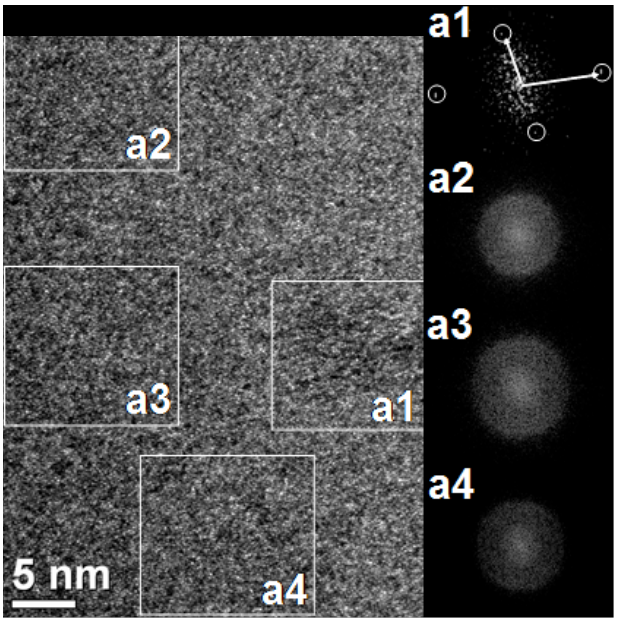

Figure A.4 HRTEM image of melt-spun $Cu_{50}Zr_{50}$ isothermally annealed at 671 K for 23 min. Insets: Corresponding FFT patterns where a1 shows the [334] zone axis of $Cu_{10}Zr_7$ nanocrystals and a2-a4 indicate amorphous regions.

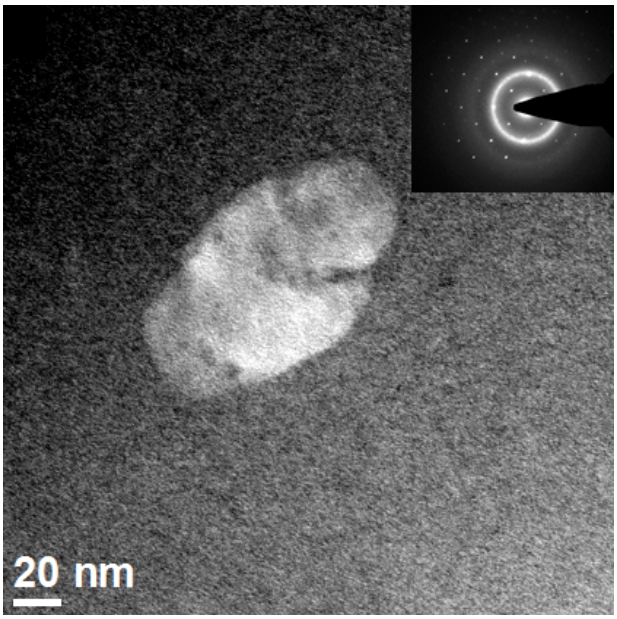

Figure A.5 A BF image of melt-spun $Cu_{50}Zr_{50}$ isothermally annealed at 671 K for 30 min, with corresponding SAED pattern showing the [$\bar{2}$,3,3] zone axis of the $Cu_{10}Zr_7$ nanocrystal.

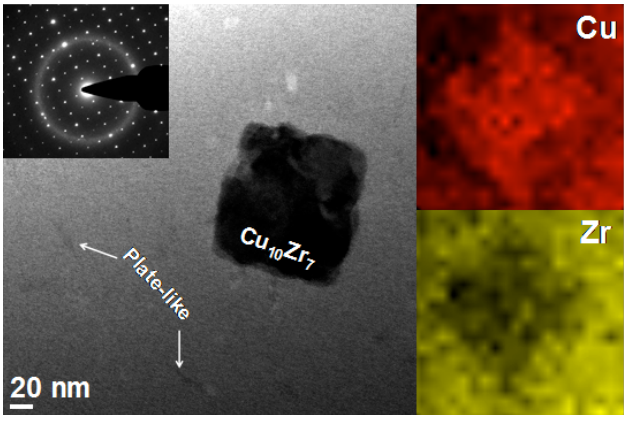

Figure A.6 A BF image of melt-spun $Cu_{50}Zr_{50}$ isothermally annealed at 671 K for 37 min. Insets: SAED pattern of the [100] zone axis and EDS element mappings of the $Cu_{10}Zr_7$ nanocrystal.

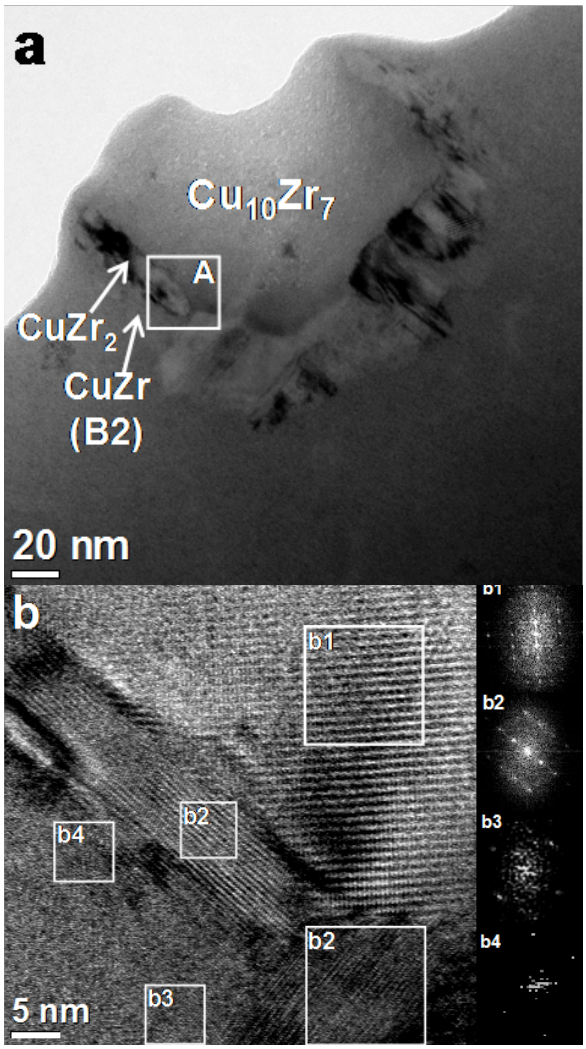

Figure A.7 (a) A BF image of melt-spun $Cu_{50}Zr_{50}$ isothermally annealed at 671 K for 37 min. (b) HRTEM image of region A showing the $Cu_{10}Zr_7$, $CuZr_2$, and CuZr (B2) phases. The insets are FFT images of regions b1-b4. Region b1 shows the [100] zone axis of the $Cu_{10}Zr_7$. The two regions labeled b2 show the [100] zone axis of two differently oriented $CuZr_2$ crystals. Regions b3-b4 show the [100] zone axis of the CuZr (B2) phase.

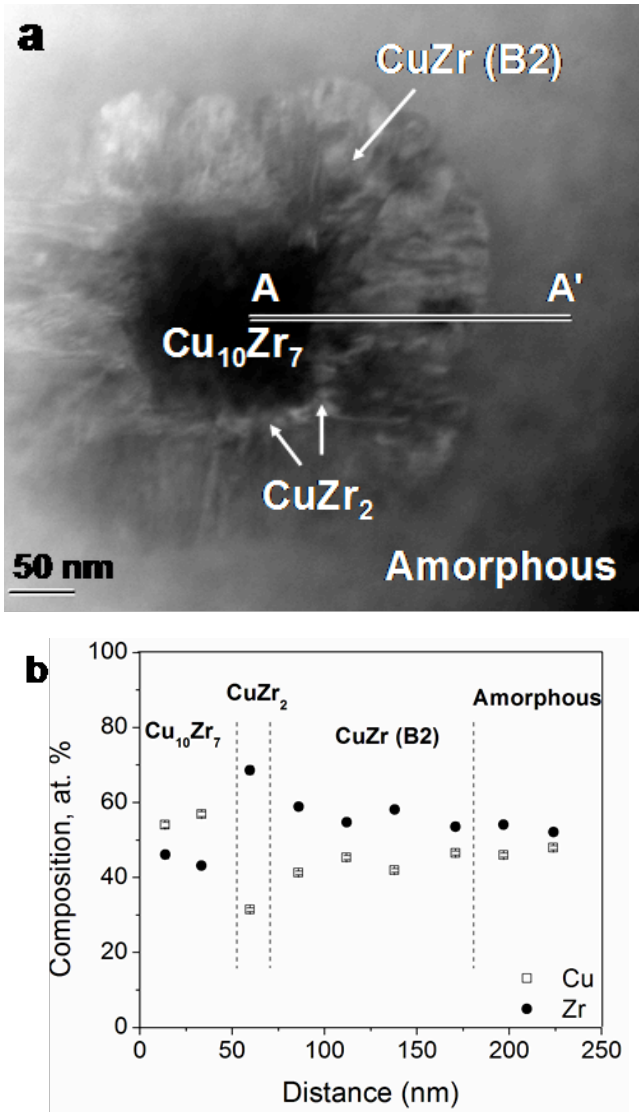

Figure A.8 (a) A STEM image of melt-spun $Cu_{50}Zr_{50}$ isothermally annealed at 671 K for 44 min. The data from the EDS line scan (A to A') is presented in (b). These data were collected along a 250 nm line, approximately, with 1-nm beam size.

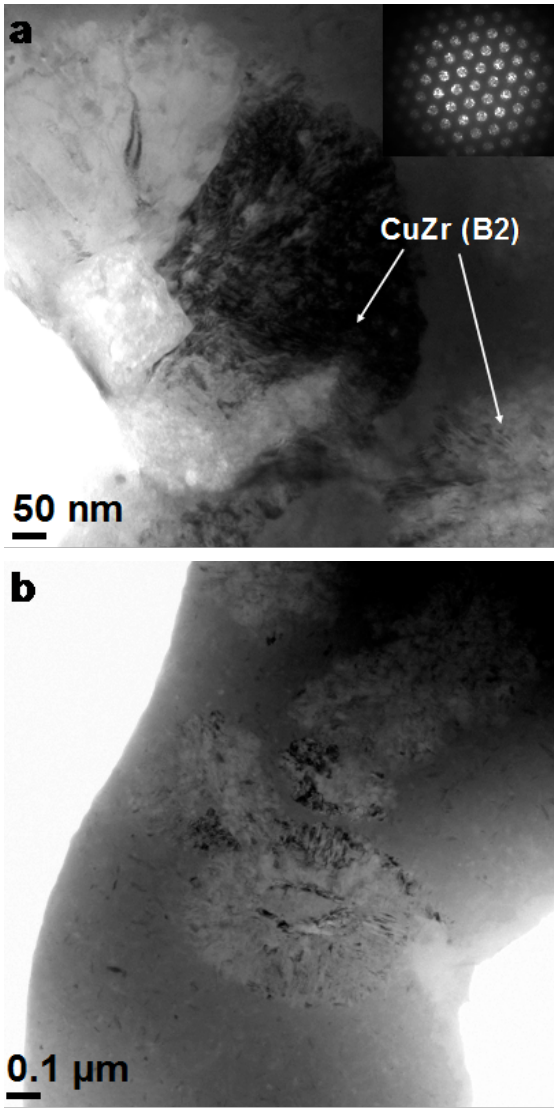

Figure A.9 BF images of melt-spun $Cu_{50}Zr_{50}$ isothermally annealed at 671 K for 49 min. (a) shows the the nucleation of CuZr (B2) on $CuZr_2$ crystals. The inset is a convergent beam electron diffraction (CBED) pattern from CuZr (B2) at a [111] zone axis. (b) shows the distribution of these crystals in the amorphous matrix.

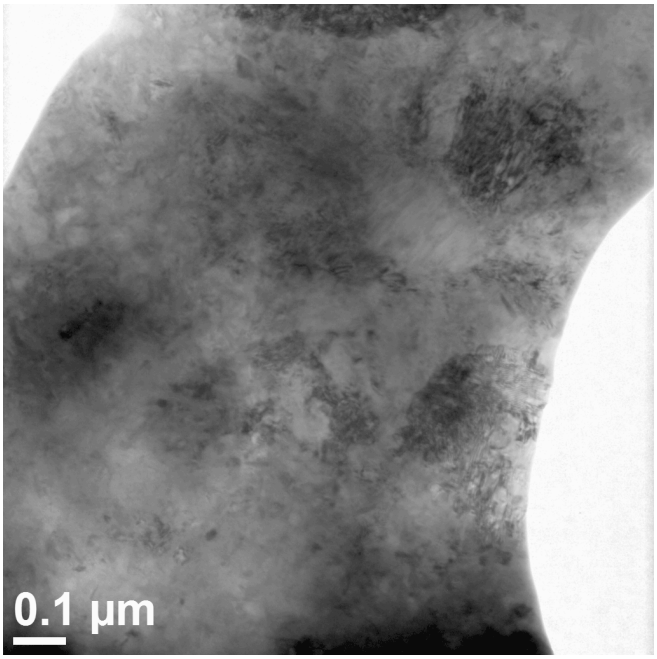

Figure A.10 A BF image of melt-spun $Cu_{50}Zr_{50}$ isothermally annealed at 671 K for 75 min.

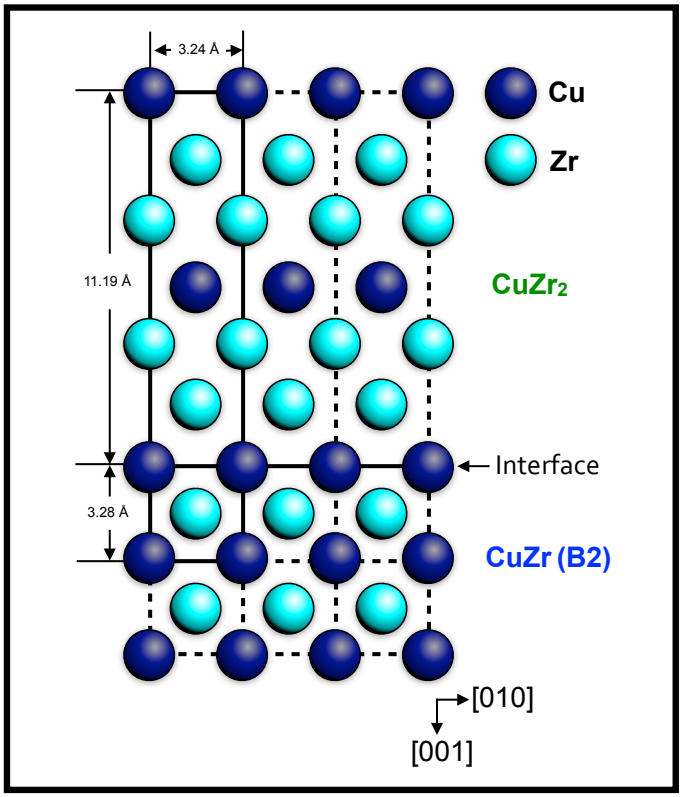

Figure A.11 A schematic showing the coherent interface between the $CuZr_2$ ($C11_b$) and CuZr (B2) phases. Through slight atomic rearrangements, the lattice parameter of $CuZr_2$ (3.24 $\mathring{A}$) enlarges to that of CuZr (3.28 $\mathring{A}$).

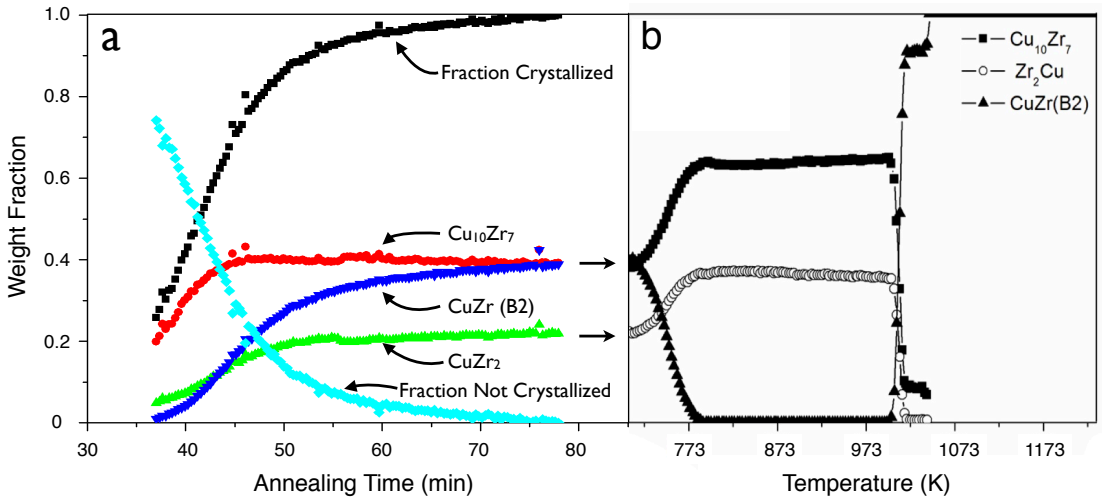

Figure A.12 (a) Time-resolved phase fractions computed from *in-situ* HEXRD patterns of isothermally annealed (673 K) melt-spun $Cu_{50}Zr_{50}$. (b) Temperature-resolved phase fractions computed from *in-situ* HEXRD patterns collected during 10 K/min heating of melt-spun $Cu_{50}Zr_{50}$ [6].

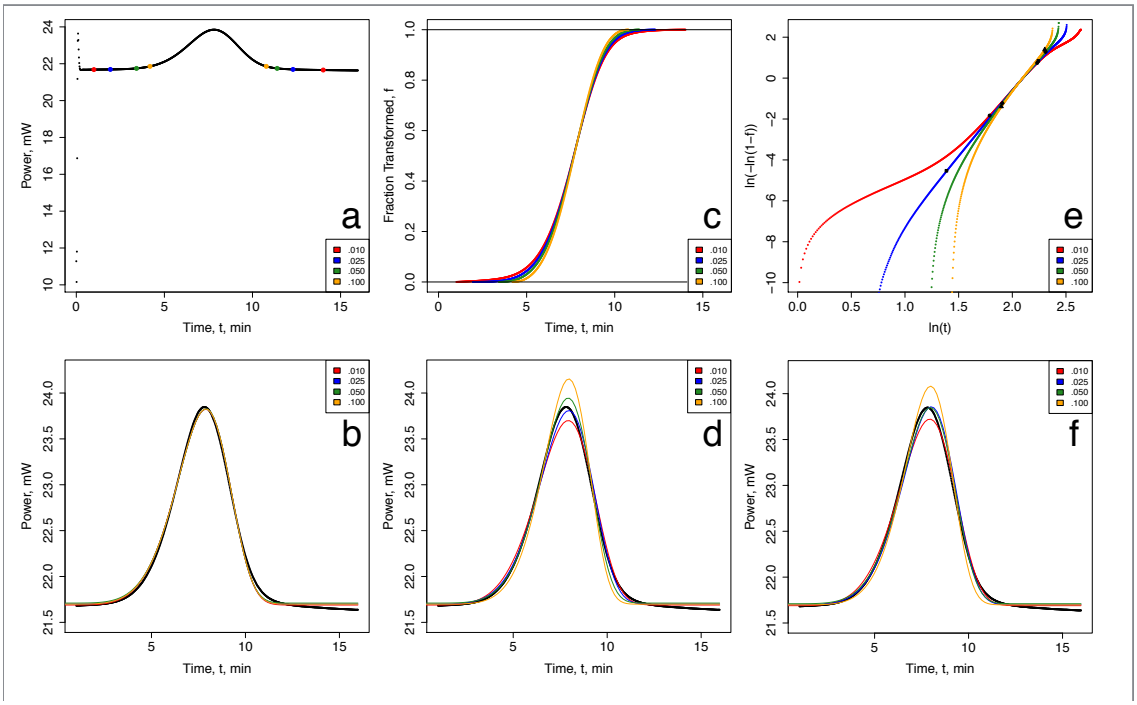

Figure A.13 (a) Raw isothermal (688.1 K) devitrification data measured by DSC. Note the initial transient signal that persists after the program changes from a ramping (100 K/min) to isothermal mode. For mathematical convenience, we present the data here such that exothermic events result in positive deflections from the baseline signal. The indicated points denote the lower and upper bounds for the data truncation scenarios we consider for this demonstration. The fitted values that we report in Table A.1 are based on truncating the raw data to include only the points greater than one percent of the peak height on both sides of the peak (listed as .010 in this figure). (b) Approximated DSC traces constructed from the expression for $\dot{Q}$ using the JMAK parameters obtained by fitting portions of the raw DSC data directly. This was carried out for the various truncation scenarios and superimposed on the raw data (solid black curve). The plot has been rescaled to omit the data corresponding to the initial transient. Note that fits obtained in this manner are relatively insensitive to the range of truncation conditions investigated here. (c) The normalized cumulative integrals calculated from the raw data in (a) for the various truncation scenarios. Note that the plot and ultimately the fitted parameters, k and n, are sensitive to the values selected for upper and lower integration bounds. (d) Approximated DSC traces based on the k and n values obtained from fitting the curves in (c) to the expression for $f(t)$. They are plotted here using the same S and C values obtained for the direct fitting results of (a), since S and C values are not computed when fitting the fraction curves to $f(t)$. (e) Logarithm plot of the curves presented in (c). Note the increased nonlinearity as the extent of data truncation increases. (f) Approximated DSC traces based on the n and k values computed from the slope and intercept of the lines corresponding with the points indicated in (e). These points were arbitrarily selected such that they visually represented the largest linear portion of each plot. Again, S and C values for (f) were the same as those from the direct fitting procedure.

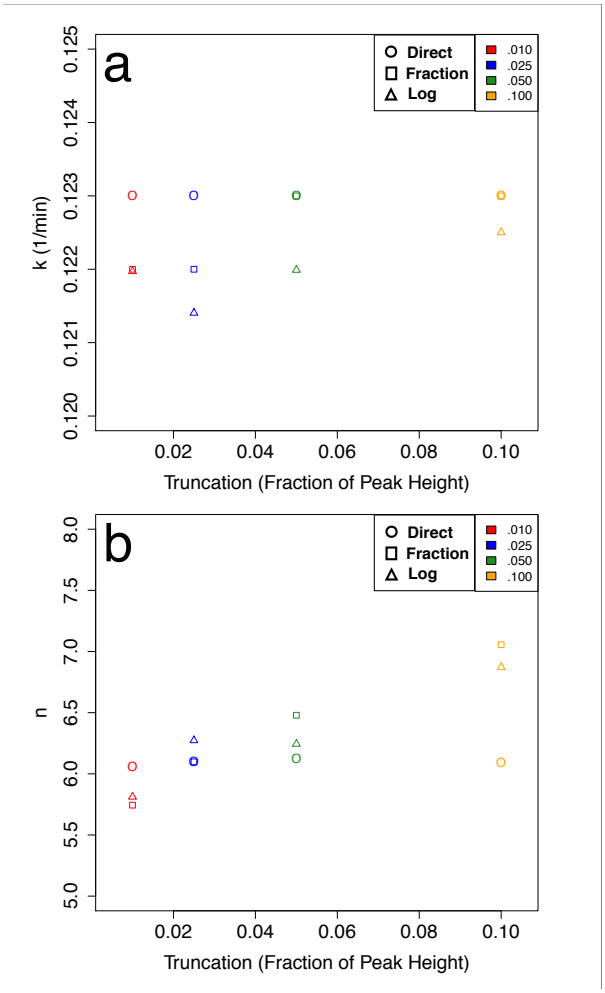

Figure A.14 k (a) and n (b) values plotted versus the truncation value (fraction of peak height) for the various fitting types demonstrated in Fig. A.13. Direct (□) refers to fitting the raw, but truncated, DSC data to the expression for $\dot{Q}$ (see Fig. A.13a-b). Fraction (◯) refers to fitting the normalized cumulative integral (fraction curve) to the expression for $f(t)$ (see Fig. A.13c-d). Log (△) refers to computing n and k from the slope and intercept of normalized cumulative integral values presented on log scales (see Fig. A.13e-f).

Bibliography

[1] Lian Yu. Polymorphism in molecular solids: An extraordinary system of red, orange, and yellow crystals. Accounts of Chemical Research, 43(9):1257–1266, 2010. doi: 10.1021/ar100040r. URL http://dx.doi.org/10.1021/ar100040r. PMID: 20560545.

[2] Hitachi Metals Ltd. Nanocrystalline soft magnetic material finemet. (Brochure No. HL-FM10-C), April 2005.

[3] A Inoue and W Zhang. Formation, thermal stability and mechanical properties of Cu-Zr and Cu-Hf binary glassy alloy rods. Mater. Trans., 45(2):584–587, FEB 2004. ISSN 1345-9678. doi: {10.2320/matertrans.45.584}.

[4] R. Ray, B. C. Giessen, and N. J. Grant. New non-crystalline phases in splat cooled transition metal alloys. Scr. Metall., 2(6):357–359, 6 1968. URL http://www.sciencedirect.com/science/article/pii/0036974868901385.

[5] Donghua Xu, Boonrat Lohwongwatana, Gang Duan, William L. Johnson, and Carol Garland. Bulk metallic glass formation in binary cu-rich alloy series – cu100xzrx (x=34, 36, 38.2, 40 at.cu64zr36 glass. Acta Mater., 52(9):2621 – 2624, 2004. ISSN 1359-6454. doi: http://dx.doi.org/10.1016/j.actamat.2004.02.009. URL http://www.sciencedirect.com/science/article/pii/S1359645404000862.

[6] I. Kalay, M.J. Kramer, and R.E. Napolitano. High-accuracy x-ray diffraction analysis of phase evolution sequence during devitrification of cu50zr50 metallic glass. Metall. Mater. Trans. A, 42(5):1144–1153, 2011. ISSN 1073-5623. doi: 10.1007/s11661-010-0531-9. URL http://dx.doi.org/10.1007/s11661-010-0531-9.

[7] R. J. Greet and D. Turnbull. Glass transition in o-terphenyl. The Journal of Chemical Physics, 46(4):1243–1251, 02 1967. URL http://dx.doi.org/10.1063/1.1840842.

[8] R. J. Greet. Solidification kinetics of 1,2-diphenylbenzene. Journal of Crystal Growth, 1 (4):195–203, 10 1967. doi: http://dx.doi.org/10.1016/0022-0248(67)90053-X. URL http://www.sciencedirect.com/science/article/pii/002202486790053X.

[9] J. H. Magill and Hin-Mo Li. Physical properties of aromatic hydrocarbons: V. the solidification behavior of 1:2 diphenylbenzene. Journal of Crystal Growth, 20(2):135–144, 9 1973. doi: http://dx.doi.org/10.1016/0022-0248(73)90127-9. URL http://www.sciencedirect.com/science/article/pii/0022024873901279.

[10] G. Scherer, D. R. Uhlmann, C. E. Miller, and K. A. Jackson. Crystallization behavior of high purity o-terphenyl. Journal of Crystal Growth, 23(4):323–330, 10 1974. doi: http://dx.doi.org/10.1016/0022-0248(74)90078-5. URL http://www.sciencedirect.com/science/article/pii/0022024874900785.

[11] Takaaki Hikima, Yôko Adachi, Minoru Hanaya, and Masaharu Oguni. Determination of potentially homogeneous-nucleation-based crystallization in o-terphenyl and an interpretation of the nucleation-enhancement mechanism. Physical Review B, 52(6):3900–3908, 08 1995. URL http://link.aps.org/doi/10.1103/PhysRevB.52.3900.

[12] Takashi Konishi and Hajime Tanaka. Possible origin of enhanced crystal growth in a glass. Phys. Rev. B, 76:220201, Dec 2007. doi: 10.1103/PhysRevB.76.220201. URL http://link.aps.org/doi/10.1103/PhysRevB.76.220201.

[13] Hanmi Xi, Ye Sun, and Lian Yu. Diffusion-controlled and diffusionless crystal growth in liquid o-terphenyl near its glass transition temperature. The Journal of Chemical Physics, 130(9):094508, 2009. doi: http://dx.doi.org/10.1063/1.3081047. URL http://scitation.aip.org/content/aip/journal/jcp/130/9/10.1063/1.3081047.

[14] C. Travis Powell, Keewook Paeng, Zhen Chen, Ranko Richert, Lian Yu, and M. D. Ediger. Fast crystal growth from organic glasses: Comparison of o-terphenyl with its

structural analogs. The Journal of Physical Chemistry B, 118(28):8203–8209, 2014. doi: 10.1021/jp501301y. URL http://dx.doi.org/10.1021/jp501301y. PMID: 24654628.

[15] D. W. McCall, D. C. Douglass, and D. R. Falcone. Molecular motion in ortho-terphenyl. The Journal of Chemical Physics, 50(9):3839–3843, 05 1969. URL http://dx.doi.org/10.1063/1.1671636.

[16] S. S. Chang and A. B. Bestul. Heat capacity and thermodynamic properties of o-terphenyl crystal, glass, and liquid. The Journal of Chemical Physics, 56(1):503–516, 01 1972. URL http://dx.doi.org/10.1063/1.1676895.

[17] S. Aikawa, Y. Maruyama, Y. Ohashi, and Y. Sasada. 1,2-diphenylbenzene (o-terphenyl). 34(9):2901–2904, 1978. URL http://dx.doi.org/10.1107/S0567740878009577.

[18] G. M. Brown and H. A. Levy. o-terphenyl by neutron diffraction. 35(3):785–788, 1979. URL http://dx.doi.org/10.1107/S0567740879004805.

[19] E. Bartsch, H. Bertagnolli, P. Chieuxp, A. David, and H. Sillescu. Temperature dependence of the static structure factor of ortho-terphenyl in the supercooled liquid regime close to the glass transition. Chemical Physics, 169(3):373–378, 2 1993. doi: http://dx.doi.org/10.1016/0301-0104(93)85108-K. URL http://www.sciencedirect.com/science/article/pii/030101049385108K.

[20] Ye Sun, Hanmi Xi, Shuang Chen, M. D. Ediger, and Lian Yu. Crystallization near glass transition: Transition from diffusion-controlled to diffusionless crystal growth studied with seven polymorphs. The Journal of Physical Chemistry B, 112(18):5594–5601, 2013/06/28 2008. doi: 10.1021/jp7120577. URL http://dx.doi.org/10.1021/jp7120577.

[21] M. D. Ediger, Peter Harrowell, and Lian Yu. Crystal growth kinetics exhibit a fragility-dependent decoupling from viscosity. The Journal of Chemical Physics, 128(3):034709, 2008. doi: http://dx.doi.org/10.1063/1.2815325. URL http://scitation.aip.org/content/aip/journal/jcp/128/3/10.1063/1.2815325.

[22] Carl Yaws. Yaws' Handbook of Antoine coefficients for vapor pressure. Knovel, Norwich, N.Y, 2005. ISBN 978-1-59124-879-8.

[23] S.H. Zhou and R.E. Napolitano. Phase stability for the cu–zr system: First-principles, experiments and solution-based modeling. Acta Mater., 58(6):2186 – 2196, 2010. ISSN 1359-6454. doi: http://dx.doi.org/10.1016/j.actamat.2009.12.004. URL http://www.sciencedirect.com/science/article/pii/S1359645409008386.

[24] T Ohkubo, H Kai, DH Ping, K Hono, and Y Hirotsu. Mechanism of heterogeneous nucleation of alpha-Fe nanocrystals from Fe89Zr7B3Cu1 amorphous alloy. SCRIPTA MATERIALIA, 44(6):971–976, APR 1 2001. ISSN 1359-6462. doi: {10.1016/S1359-6462(00)00689-8}.

[25] ME McHenry, F Johnson, H Okumura, T Ohkubo, VRV Ramanan, and DE Laughlin. The kinetics of nanocrystallization and microstructural observations in FINEMET, NANOPERM and HITPERM nanocomposite magnetic materials. SCRIPTA MATERIALIA, 48(7):881–887, APR 1 2003. ISSN 1359-6462. doi: {10.1016/S1359-6462(02)00597-3}. Workshop on Nanostructured Advanced Magenetic Materials, ISREE, GERMANY, JUN 06-13, 2002.

[26] YN KOVAL, GS FIRSTOV, and AV KOTKO. MARTENSITIC-TRANSFORMATION AND SHAPE MEMORY EFFECT IN ZRCU INTERMETALLIC COMPOUND. SCRIPTA METALLURGICA ET MATERIALIA, 27(11):1611–1616, DEC 1 1992. ISSN 0956-716X. doi: {10.1016/0956-716X(92)90153-6}.

[27] A. V. Zhalko-Titarenko, M. L. Yevlashina, V. N. Antonov, B. Yu. Yavorskii, Yu. N. Koval, and G. S. Firstov. Electronic and crystal structure of the zrcu intermetallic compound close to the point of structural transformation. physica status solidi (b), 184(1):121–127, 1994. ISSN 1521-3951. doi: 10.1002/pssb.2221840108. URL http://dx.doi.org/10.1002/pssb.2221840108.

[28] YN Koval, GS Firstov, JV Humbeeck, L Delaey, and WY Jang. B2 intermetallic compounds of Zr. New class of the shape memory alloys. JOURNAL DE PHYSIQUE IV, 5

(C8, 2):1103–1108, DEC 1995. ISSN 1155-4339. International Conference on Martensitic Transformation (ICOMAT 95), LAUSANNE, SWITZERLAND, AUG 20-25, 1995.

[29] S. H. Zhou and R. E. Napolitano. Identification of the B33 martensite phase in Cu-Zr using first-principles and X-ray diffraction. SCRIPTA MATERIALIA, 59(10):1143–1146, NOV 2008. ISSN 1359-6462. doi: {10.1016/j.scriptamat.2008.07.040}.

[30] Susan Aldridge. The shape shifters. Chemistry World, pages 64–70, 2007.

[WHO] http://www.who.int/mediacentre/factsheets/fs360/en/. URL http://www.who.int/mediacentre/factsheets/fs360/en/.

[inj] URL http://www.unicef.org/immunization/23245_safety.html.

[31] Neelam Dhingra. Making safe blood available in africa. Statement, World Health Organization, June 2006.

[32] Shuang Chen, Hanmi Xi, and Lian Yu. Cross-nucleation between roy polymorphs. Journal of the American Chemical Society, 127(49):17439–17444, 2005. doi: 10.1021/ja056072d. URL http://dx.doi.org/10.1021/ja056072d. PMID: 16332095.

[33] J. Eckert, J. Das, S. Pauly, and C. Duhamel. Mechanical properties of bulk metallic glasses and composites. J. Mater. Res., 22:285–301, 2 2007. ISSN 2044-5326. doi: 10.1557/jmr.2007.0050. URL http://journals.cambridge.org/article_S0884291400092554.

[34] Ryusuke Hasegawa. Advances in amorphous and nanocrystalline materials. J. Magn. Magn. Mater., 324(21):3555 – 3557, 2012. ISSN 0304-8853. doi: http://dx.doi.org/10.1016/j.jmmm.2012.02.088. URL http://www.sciencedirect.com/science/article/pii/S0304885312001850. Fifth Moscow international symposium on magnetism.

[35] R. L. Freed and J. B. Vander Sande. A study of the crystallization of two non-crystalline cu-zr alloys. J. Non-Cryst. Solids, 27(1):9–28, 1 1978. URL http://www.sciencedirect.com/science/article/pii/0022309378900327.

[36] D.E. Polk, C.E. Dube, and B.C. Giessen. The Effect of Oxygen Additions on the Properties of Amorphous Transition Metal Alloys. Defense Technical Information Center, 1978. URL http://books.google.com/books?id=L_rZNwAACAAJ.

[37] A.J. Kerns, D.E. Polk, R. Ray, and B.C. Giessen. Thermal behavior of zr-cu metallic glasses. Mater. Sci. Eng., 38(1):49 – 53, 1979. ISSN 0025-5416. doi: http://dx.doi.org/10.1016/0025-5416(79)90031-4. URL http://www.sciencedirect.com/science/article/pii/0025541679900314.

[38] K. H. J. Buschow. Thermal stability of amorphous zrcu alloys. J. Appl. Phys., 52(5): 3319–3323, 1981. doi: http://dx.doi.org/10.1063/1.329152. URL http://scitation.aip.org/content/aip/journal/jap/52/5/10.1063/1.329152.

[39] Z. Altounian, Tu Guo-hua, and J. O. Strom-Olsen. Crystallization characteristics of cu-zr metallic glasses from cu[sub 70]zr[sub 30] to cu[sub 25]zr[sub 75]. J. Appl. Phys., 53(7): 4755–4760, 07 1982. URL http://dx.doi.org/10.1063/1.331304.

[40] K H J Buschow. Short-range order and thermal stability in amorphous alloys. J. Phys. F: Met. Phys., 14(3):593, 1984. URL http://stacks.iop.org/0305-4608/14/i=3/a=005.

[41] K Dini and R A Dunlap. Crystallisation and hydrogen absorption in amorphous cu 60 zr 40 and cu 50 zr 50. J. Phys. F: Met. Phys., 15(2):273, 1985. URL http://stacks.iop.org/0305-4608/15/i=2/a=005.

[42] Mireille Harmelin, André Naudon, Jean-Marc Frigerio, and Josette Rivory. Comparison of the structural relaxation and glass transition in both liquid-quenched and sputtered copper-zirconium amorphous alloys. a study by dsc and x-ray scattering. In S. STEEB and H. WARLIMONT, editors, Rapidly Quenched Metals, pages 659 – 662. Elsevier, 1985. ISBN 978-0-444-86939-5. doi: http://dx.doi.org/10.1016/B978-0-444-86939-5.50158-5. URL http://www.sciencedirect.com/science/article/pii/B9780444869395501585.

[43] E. Kneller, Y. Khan, and U. Gorres. The alloy system copper-zirconium .2. crystallization of the glasses from cu70zr30 to cu26zr74. Z. Metallkd, 77(3):152–163, Mar 1986. ISSN 0044-3093.

[44] Eric C. Stelter and David Lazarus. Diffusion and thermal stability of amorphous copper zirconium. Phys. Rev. B, 36:9545–9558, Dec 1987. doi: 10.1103/PhysRevB.36.9545. URL http://link.aps.org/doi/10.1103/PhysRevB.36.9545.

[45] JSC JANG and CC KOCH. The glass-transition temperature in amorphous cu1-xzrx alloys synthesized by mechanical alloying milling. Scr. Metall., 23(10):1805–1810, OCT 1989. ISSN 0036-9748. doi: 10.1016/0036-9748(89)90365-7.

[46] H. Lu, C.L. Bao, Q.K. Xue, and D.S. Tang. Clustering effect in the crystallization process of a cuzr amorphous alloy. Appl. Phys. A., 52(5):302–306, 1991. ISSN 0947-8396. doi: 10.1007/BF00324769. URL http://dx.doi.org/10.1007/BF00324769.

[47] H. Ohshiro and T. Arakawa. Thermal behaviour of amorphous cu(x)zr(1 - x) powders synthesized by mechanical alloying. J. Alloys Compd., 215:251–255, November 1994.

[48] Wha-Nam Myung, Hyun-Goo Kim, and T Masumoto. Glass transition behaviour of zr- and ti-based binary amorphous alloys. Mater. Sci. Eng. A., 179–180, Part 1(0):252 – 255, 1994. ISSN 0921-5093. doi: http://dx.doi.org/10.1016/0921-5093(94)90204-6. URL http://www.sciencedirect.com/science/article/pii/0921509394902046.

[49] A PRATAP, A PRASAD, SR JOSHI, NS SAXENA, MP SAKSENA, and K AMIYA. Crystallization kinetics of cu50zr50 glass. In AR Yavari, editor, MECHANICALLY ALLOYED AND NANOCRYSTALLINE MATERIALS: ISMANAM-94, volume 179- of MATERIALS SCIENCE FORUM, pages 851–854, BRANDRAIN 6, CH-8707 ZURICH-UETIKON, SWITZERLAND, 1995. European Union; Japan Soc Powder & Powder Met; Ecole Electrochim & Electromet Grenoble; Zoz Gmbh; Kurimoto Ltd; Int Sci Fdn, ISF; City Grenoble, TRANSTEC PUBLICATIONS LTD. ISBN 0-87849-688-2. International Symposium on Metastable, Mechanically Alloyed and Nanocrystalline Materials

(ISMANAM-94)/European Meeting on Disordering and Amorphization, GRENOBLE, FRANCE, JUN 27-JUL 01, 1994.

[50] E.A Leonova, S.D Kaloshkin., and I.A. Tomilin. Thermal stability and phase transformations during crystallization of amorphous zirconium-based alloys. 1. cu-zr system. Izv. Ross. Akad. Nauk, Ser. Fiz., 65(10):1420–1423, 2001.

[51] Kirit Lad, Mohammed Maaroof, K.G. Raval, Arun Pratap, and K.G. Raval. Fractal growth kinetics during crystallization of amorphous cu50zr50. Prog. Cryst. Growth Charact. Mater., 45(1–2):15 – 19, 2002. ISSN 0960-8974. doi: http://dx.doi.org/10.1016/S0960-8974(02)00022-0. URL http://www.sciencedirect.com/science/article/pii/S0960897402000220.

[52] O.J. Kwon, Y.C. Kim, K.B. Kim, Y.K. Lee, and E. Fleury. Formation of amorphous phase in the binary cuzr alloy system. Metals and Materials International, 12(3):207–212, 2006. ISSN 1598-9623. doi: 10.1007/BF03027532. URL http://dx.doi.org/10.1007/BF03027532.

[53] Oh-Jib Kwon, Young-Kook Lee, Sang-Ok Park, Jae-Chul Lee, Yu-Chan Kim, and Eric Fleury. Thermal and mechanical behaviors of cu-zr amorphous alloys. Mater. Sci. Eng. A., 449–451(0):169 – 171, 2007. ISSN 0921-5093. doi: http://dx.doi.org/10.1016/j.msea.2006.02.298. URL http://www.sciencedirect.com/science/article/pii/S0921509306013712.

[54] Dmitri V. Louzguine-Luzgin, Guoqiang Xie, Wei Zhang, and Akihisa Inoue. Influence of al and ag on the devitrification behavior of a cu-zr glassy alloy. Mater. Trans., 48(8):2128–2132, AUG 2007. ISSN 1345-9678. doi: 10.2320/matertrans.MF200633.

[55] N. Mattern, A. Schöps, U. Kühn, J. Acker, O. Khvostikova, and J. Eckert. Structural behavior of cuxzr100x metallic glass (x=3570). J. Non-Cryst. Solids, 354(10–11):1054 – 1060, 2008. ISSN 0022-3093. doi: http://dx.doi.org/10.1016/j.jnoncrysol.2007.08.035. URL http://www.sciencedirect.com/science/article/pii/S002230930700837X.

[56] N. Mehta, K. Singh, and N.S. Saxena. Comparative analysis of thermal crystallization in cu50ti50 and cu50zr50 metallic glasses. Phys. B, 403(21–22):3928 – 3931, 2008. ISSN 0921-4526. doi: http://dx.doi.org/10.1016/j.physb.2008.07.016. URL http://www.sciencedirect.com/science/article/pii/S0921452608003232.

[57] X. D. Wang, Q. K. Jiang, Q. P. Cao, J. Bednarcik, H. Franz, and J. Z. Jiang. Atomic structure and glass forming ability of cu46zr46al8 bulk metallic glass. J. Appl. Phys., 104 (9):1–5, 2008.

[58] S. Pauly, J. Das, N. Mattern, D. H. Kim, and J. Eckert. Phase formation and thermal stability in cu–zr–ti(al) metallic glasses. Intermetallics, 17(6):453–462, 6 2009. URL http://www.sciencedirect.com/science/article/pii/S0966979508002872.

[59] Rubén Fernández, Wilson Carrasco, and Alejandro Zúñiga. Structure and crystallization of amorphous cu–zr–al powders. J. Non-Cryst. Solids, 356(33–34):1665 – 1669, 2010. ISSN 0022-3093. doi: http://dx.doi.org/10.1016/j.jnoncrysol.2010.06.016. URL http://www.sciencedirect.com/science/article/pii/S0022309310003480.

[60] D. V. Louzguine-Luzgin, G. Xie, Q. Zhang, and A. Inoue. Devitrification behavior and crystal-glassy mixed-phase structures observed in partially crystallized cu-based glassy alloys. In K Ewsuk, M Naito, T Kakeshita, S Kirihara, K Uematsu, and H Abe, editors, CHARACTERIZATION AND CONTROL OF INTERFACES FOR HIGH QUALITY ADVANCED MATERIALS III, volume 219 of Ceramic Transactions, pages 3–8, 735 CERAMIC PLACE, WESTERVILLE, OH 43081-8720 USA, 2010. Amer Ceram Soc, AMER CERAMIC SOC. ISBN 978-0-470-90917-1. 3rd International Conference on Characterization and Control of Interfaces for High Quality Advanced Materials, Kurashiki, JAPAN, 2009.

[61] D.V. Louzguine-Luzgin, G. Xie, Q. Zhang, C. Suryanarayana, and A. Inoue. Formation, structure, and crystallization behavior of cu-based bulk glass-forming alloys. Metall. Mater. Trans. A, 41(7):1664–1669, 2010. ISSN 1073-5623. doi: 10.1007/s11661-009-0087-8. URL http://dx.doi.org/10.1007/s11661-009-0087-8.

[62] N. Mattern, A. Shariq, B. Schwarz, U. Vainio, and J. Eckert. Structural and magnetic nanoclusters in cu50zr50xgdx (x=5 at.metallic glasses. Acta Mater., 60(5):1946 – 1956, 2012. ISSN 1359-6454. doi: http://dx.doi.org/10.1016/j.actamat.2012.01.019. URL http://www.sciencedirect.com/science/article/pii/S1359645412000572.

[63] X. Cui, F.Q. Zu, Z.Z. Wang, Z.Y. Huang, X.Y. Li, and L.F. Wang. Study of the reversible intermetallic phase: B2-type cuzr. Intermetallics, 36(0):21 – 24, 2013. ISSN 0966-9795. doi: http://dx.doi.org/10.1016/j.intermet.2012.12.008. URL http://www.sciencedirect.com/science/article/pii/S0966979512004542.

[64] Tim E Cullinan, Ilkay Kalay, Eren Kalay, Matt J Kramer, and Ralph E Napolitano. Kinetics and mechansims of isothermal devitrification in amorphous cu50zr50. 2015.

[65] E.M. Carvalho and I.R. Harris. Constitutional and structural studies of the intermetallic phase, zrcu. J. Mater. Sci., 15(5):1224–1230, 1980. ISSN 0022-2461. doi: 10.1007/BF00551811. URL http://dx.doi.org/10.1007/BF00551811.

[66] Weiler. Ber., 29:115, 1896.

[67] W. E. Bachmann and H. T. Clarke. The mechanism of the wurtz-fittig reaction. JOURNAL OF THE AMERICAN CHEMICAL SOCIETY, 49:2089–2098, 1927. ISSN 0002-7863. doi: 10.1021/ja01407a038.

[68] C. J. Birkett Clews and Kathleen Lonsdale. Structure of 1.2-diphenylbenzene ($c_{18}h_{14}$). Proceedings of the Royal Society of London. Series A - Mathematical and Physical Sciences, 161(907):493–504, 1937. URL http://rspa.royalsocietypublishing.org/content/161/907/493.short.

[69] C. F. H. Allen and F. P. Pingert. The chemistry of o-terphenyl (o-diphenylbenzene). i. the general reactivity, basal structure and rearrangements of the hydrocarbon. Journal of the American Chemical Society, 64(6):1365–1371, 2013/05/13 1942. doi: 10.1021/ja01258a038. URL http://dx.doi.org/10.1021/ja01258a038.

[70] Isabella Lugoski Karle and L. O. Brockway. The structures of biphenyl, o-terphenyl and tetraphenylene1. Journal of the American Chemical Society, 66(11):1974–1979, 2013/04/09 1944. doi: 10.1021/ja01239a057. URL http://dx.doi.org/10.1021/ja01239a057.

[71] R. J. Good, E. E. Hardy, A. M. Ellenburg, and H. B. Richards. The solubility of p-terphenyl in o- and m-terphenyls and in biphenyl1. Journal of the American Chemical Society, 75(2):436–442, 2013/06/25 1953. doi: 10.1021/ja01098a053. URL http://dx.doi.org/10.1021/ja01098a053.

[72] J. N. Andrews and A. R. Ubbelohde. Melting and crystal structure: The melting parameters of some polyphenyls. Proceedings of the Royal Society of London. Series A, Mathematical and Physical Sciences, 228(1175):435–447, 03 1955. doi: 10.2307/99635. URL http://www.jstor.org/stable/99635.

[73] Ye Sun, Hanmi Xi, M. D. Ediger, and Lian Yu. Diffusionless crystal growth from glass has precursor in equilibrium liquid. The Journal of Physical Chemistry B, 112(3):661–664, 2008. doi: 10.1021/jp709616c. URL http://dx.doi.org/10.1021/jp709616c. PMID: 18095668.

[74] D. Turnbull. Solid State Phys., 3(225), 1956.

[75] M. Volmer. Crystal growth. Z. Physik, 9:193, 1922.

[76] J.D. Hoffman. Soc. Plastics Engrs. Trans., page 315, 1964.

[77] J.W. Cahn. Acta Met., 8:554, 1960.

[78] J.W. Cahn, W.B. Hillig, and Sears G.W. Acta Met., page 1421, 1964.

[79] M.I. Volmer and M. Marder. Z. Physik. Chem. A, page 97, 1931.

[80] W.B. Hillig and D. Turnbull. J. Chem. Phys., 24:914, 1956.

[81] R. J. Greet and D. Turnbull. Test of adam–gibbs liquid viscosity model with o-terphenyl specific-heat data. The Journal of Chemical Physics, 47(6):2185–2190, 09 1967. URL http://dx.doi.org/10.1063/1.1712251.

[82] A. Biswas. Solidification of acoustically levitated o-terphenyl crystals: a raman study. Journal of Crystal Growth, 147(1–2):155–164, 1 1995. doi: http://dx.doi.org/10.1016/0022-0248(94)00670-9. URL http://www.sciencedirect.com/science/article/pii/0022024894006709.

[83] Norimaru Okamoto and Masaharu Oguni. Discovery of crystal nucleation proceeding much below the glass transition temperature in a supercooled liquid. Solid State Communications, 99(1):53 – 56, 1996. ISSN 0038-1098. doi: http://dx.doi.org/10.1016/0038-1098(96)00139-1. URL http://www.sciencedirect.com/science/article/pii/0038109896001391.

[84] Masaharu Oguni. 'intra-cluster rearrangement' model for the -process in supercooled liquids, as opposed to 'cooperative rearrangement of whole molecules within a cluster'. Journal of Non-Crystalline Solids, 210(2–3):171 – 177, 1997. ISSN 0022-3093. doi: http://dx.doi.org/10.1016/S0022-3093(96)00607-2. URL http://www.sciencedirect.com/science/article/pii/S0022309396006072.

[85] Takaaki Hikima, Minoru Hanaya, and Masaharu Oguni. Numerical and morphological approach to the mechanism of homogeneous-nucleation-based crystallization in o-terphenyl. Journal of Non-Crystalline Solids, 235–237(0):539 – 547, 1998. ISSN 0022-3093. doi: http://dx.doi.org/10.1016/S0022-3093(98)00610-3. URL http://www.sciencedirect.com/science/article/pii/S0022309398006103.

[86] Takaaki Hikima, Minoru Hanaya, and Masaharu Oguni. Microscopic observation of a peculiar crystallization in the glass transition region and -process as potentially controlling the growth rate in triphenylethylene. Journal of Molecular Structure, 479(2–3):245 – 250, 1999. ISSN 0022-2860. doi: http://dx.doi.org/10.1016/S0022-2860(98)00875-8. URL http://www.sciencedirect.com/science/article/pii/S0022286098008758.

[87] Dwight D. Back, Lawrence R. Grzyll, and Mary Corrigan. Dsc enthalpy of vaporization measurements of high temperature two-phase working fluids. Thermochimica Acta, 272 (0):53–63, 1 1996. doi: http://dx.doi.org/10.1016/0040-6031(95)02615-0. URL http://www.sciencedirect.com/science/article/pii/0040603195026150.

[88] K. L. Ngai, J. H. Magill, and D. J. Plazek. Flow, diffusion and crystallization of supercooled liquids: Revisited. The Journal of Chemical Physics, 112(4):1887–1892, 01 2000. URL http://dx.doi.org/10.1063/1.480752.

[89] Tian Wu and Lian Yu. Origin of enhanced crystal growth kinetics near tg probed with indomethacin polymorphs. The Journal of Physical Chemistry B, 110(32):15694–15699, 2006. doi: 10.1021/jp062771g. URL http://dx.doi.org/10.1021/jp062771g. PMID: 16898713.

[90] H. Tanaka. Phys. Rev. E, 011505, 2003.

[91] J. Frenkel. Phys. Z. Sowietunion, 1:498–500, 1932.

[92] D. Turnbull and J. C. Fisher. Rate of nucleation in condensed systems. The Journal of Chemical Physics, 17(1):71–73, 01 1949. URL http://dx.doi.org/10.1063/1.1747055.

[93] L. Klein and D.R. Uhlmann. J. Geophys. Res., 79:4869, 1974.

[94] J.H. Magill and D.J. Plazek. Nature (London), 209:70, 1966.

[95] W Kurz and D.J. Fisher. Fundamentals of Solidification. CRC Press, 1998.

[96] JD HUNT, KA JACKSON, and H BROWN. TEMPERATURE GRADIENT MICROSCOPE STAGE SUITABLE FOR FREEZING MATERIALS WITH MELTING POINTS BETWEEN -100 AND +200 DEGREES C. REVIEW OF SCIENTIFIC INSTRUMENTS, 37(6):805–&, 1966. ISSN 0034-6748. doi: {10.1063/1.1720336}.

[97] N. Dey and J.A. Sekhar. Interface configurations during the directional growth of salol—ii. thermal stress cracking. Acta Metallurgica et Materialia, 41(2):425 – 439, 1993. ISSN

0956-7151. doi: http://dx.doi.org/10.1016/0956-7151(93)90072-Z. URL http://www.sciencedirect.com/science/article/pii/095671519390072Z.

[98] N. Dey and J.A. Sekhar. Interface configurations during the directional growth of salol—i. morphology. Acta Metallurgica et Materialia, 41(2):409 – 424, 1993. ISSN 0956-7151. doi: http://dx.doi.org/10.1016/0956-7151(93)90071-Y. URL http://www.sciencedirect.com/science/article/pii/095671519390071Y.

[99] Dongkai Shangguan and JohnD. Hunt. In situ observation of faceted cellular array growth. Metallurgical Transactions A, 22(4):941–945, 1991. ISSN 0360-2133. doi: 10.1007/BF02659005. URL http://dx.doi.org/10.1007/BF02659005.

[100] Chunguang Tang and Peter Harrowell. Anomalously slow crystal growth of the glass-forming alloy cuzr. Nat. Mater., 12(6):507–511, 06 2013. URL http://dx.doi.org/10.1038/nmat3631.